RUN WITH THE HUNTED:
SEARCHING FOR SURVIVING SN IA COMPANIONS AND CONSTRAINING THE SN IA
PROGENITOR SYSTEM THROUGH STELLAR MODELING

By

Joshua V. Shields

A DISSERTATION

Submitted to
Michigan State University
in partial fulfillment of the requirements
for the degree of

Astrophysics—Doctor of Philosophy

2024

ABSTRACT

Type Ia Supernovae (SNe Ia) mark the explosive terminations of the otherwise quiet, dead cores of low mass stars known as White Dwarfs (WDs). The largest outstanding question in the SN Ia field is: What is the full progenitor system of these events, or more specifically what type of binary interaction prompts thermonuclear runaway inside a WD to produce a SN Ia in the Universe? Theorists have proposed a large number of seemingly viable progenitor systems for these energetic transients. To move forward and solidify our understanding of SNe Ia, the field requires a way to test the proposed theoretical progenitor scenarios and discriminate between them. One particularly promising method of discrimination is to examine stars within Supernova Remnants (SNRs) to identify or rule out the existence of surviving companions to exploded WDs. This can be accomplished by backwards modeling each potential surviving companion star to understand the star's properties, and then comparing the constrained properties of the star to the predicted properties of surviving companions. *This thesis adds to the growing body of evidence that will disambiguate the progenitor system of SNe Ia by systematically studying stars within SNRs Ia, and makes similar future stellar studies more accurate and approachable by releasing a new stellar spectral synthesis.*

In the first surviving companion investigation presented in this thesis, I examine the interior stellar population of the SN 1006 remnant. The goal of this investigation is to test the Dynamically Driven Double-Degenerate Double-Detonation (D6) scenario, a recently popular and promising SN Ia progenitor theory. This theory predicts the existence of a hypervelocity WD within the remnant, an anomalously bright WD moving at greater than $1000 \, \mathrm{km \, s^{-1}}$. I perform high-precision astrometry to extract the proper motion of each star within the remnant and compare them to the predicted properties of a theoretical hypervelocity WD. I do not detect any star within the remnant matching the description of a hypervelocity WD predicted by the D6 scenario.

In the second surviving companion investigation presented in this thesis, I analyze SNR 0509−67.5, a SN Ia remnant in the Large Magellanic Cloud (LMC). In this investigation, I utilize the constraints of the LMC (i.e., known distances and foreground extinctions to the enclosed stars)

to model the stellar population interior to the remnant and extract astrophysical properties of each star inside the remnant. I review the literature to gather a list of predicted properties of the surviving companion on timescales similar to the age of the remnant (e.g., the star will be inflated or heated due to interaction with SN ejecta), and then compare those properties to the properties of the modeled stars. All progenitor scenarios I consider predict that a surviving companion would be clearly identifiable against the unrelated stellar population. I do not detect a star within the remnant matching any of the peculiar properties predicted by the individual progenitor scenarios, and rule out the existence of a surviving companion within the remnant in accordance with those progenitor scenarios.

The stellar modeling of the surviving companion searches presented here makes use of pre-existing stellar spectral synthesis codes. While those codes were adequate to model ordinary stars and discriminate them against potential surviving companions, those codes are generally inadequate to model the surviving companions themselves. In addition, the codes are written in older programming languages that are no longer widely used in astrophysics which creates a considerable barrier to extending them to accurately model new systems. To enable the modeling of peculiar systems that require different physical treatments and approximations to normal stellar atmospheres, I present a new stellar spectral synthesis code called STARDIS. Stardis is open-source, written in Python, and is intended to be both modular and easily modifiable. I include a review of the currently included physics, describe the state of the code, and validate its output against existing codes. The work in this dissertation to develop a modern, approachable, and extensible stellar spectral synthesis code will enable the next generation of stellar investigations across astronomy.

This thesis is dedicated.

ACKNOWLEDGEMENTS

Your acknowledgements here.

TABLE OF CONTENTS

LIST OF TABLES

LIST OF FIGURES

LIST OF ABBREVIATIONS

SN(e) Ia   Type Ia Supernova(e)

WD   White Dwarf

MS   Main Sequence

C/O   Carbon/Oxygen

DDet   Double Detonation

SD   Single Degenerate

SNR   Supernova Remnant

ESA   European Space Agency

HST   Hubble Space Telescope

D6   Dynamically Driven Double-Degenerate Double-Detonation

DECam   Dark Energy Camera

CTIO   Cerro Tololo Inter-American Observatory

WCS   World Coordinate System

PSF   Point Spread Function

CCD   Charge-coupled Device

ICRS   International Celestial Reference System

DR   Data Release

RMS   Root Mean Square

MC   Monte Carlo

LMC   Large Magellanic Cloud

HSC   Hubble Source Catalog

A22   Arunachalem et al. 2022

SED   Spectral Energy Distribution

MJD   Modified Julian Date

PI   Principal Investigator

NSF   National Science Foundation

CMD   Color Magnitude Diagram

IR   Infrared

UV   Ultraviolet

MSU   Michigan State University

CHAPTER 1

INTRODUCTION

1.1   Stellar Evolution, White Dwarfs and Type Ia Supernovae

Type Ia Supernovae (SNe Ia) are the violent explosions of White Dwarfs (WDs), the dead cores of stars less massive than about 8 $M_\odot$ that have exhausted all of their hydrogen, having burned it into heavier elements through nuclear fusion. The vast majority of the energy a star produces during its lifetime comes from this H burning, and this energy supports the star against gravitational collapse and turns into electromagnetic radiation that makes the star shine. Consequently, when nuclear fusion halts the star collapses inwards and sheds its outer layers until it becomes roughly the size of the earth. At this point, the collapse halts once again as electron degeneracy pressure becomes important. Due to the Pauli exclusion principle, even zero temperature electrons at high densities continue to supply pressure which is strong enough to counteract gravitational contraction.

For most WDs, that is where the story ends. The stars contain some residual heat so they glow white, but as photons and neutrinos carry energy away from the star and no further energy is produced, WDs are largely destined to fade and cool for the rest of cosmic time. However, for a small number of these objects, the story has a different final chapter. Instead of a quiet, and uneventful rest, some WDs containing mostly Carbon and Oxygen (C/O) perform one ultimate awe-inspiring and violent act. Nuclear fusion reignites and heavier elements start being produced. This nuclear burning is a highly temperature dependent process, and the energy produced is quickly converted into heat that raises the temperature of the system. In normal circumstances, raising the temperature of a gas would cause the system to expand and find a new equilibrium. However, because the WD is supported by electron degeneracy pressure, energy must be used to lift electron degeneracy before expansion can occur. This process is too slow to keep up with the nuclear fusion, and instead of stable burning akin to what occurs in the center of normal stars, the system undergoes a process called thermonuclear runaway. Fusion increases the temperature of the system, which increases the reaction rate of the nuclear burning, which increases the temperature of the system further. In summation, a single spark in the WD culminates with the star obliterating itself

completely, briefly producing enough energy to out shine an entire galaxy comprising billions of stars (see e.g. Figure 1.1). For a short period of time the system produces of order 10^{43}erg s^{-1} in photons, shining roughly 10 orders of magnitude brighter than a star like our Sun. This is what we call a SN Ia. These events are critically important to the sustained life cycle of galaxies, and they provide a fundamental cornerstone of our astrophysical understanding of the Universe.

1.1.1 The Role of SNe Ia in Shaping the Universe

SNe Ia shape the Universe as we know it in a number of important ways. SNe Ia create a significant fraction of the iron group elements in the Universe (Timmes et al., 1995; Kobayashi et al., 2020) (and see Figure 1.1.1. The heavy elements produced in the event are recycled into the interstellar medium, the gas that will go on to form future stars and planets. Many fundamental building blocks of life as we know it (e.g., Iron, one of the major components of both rocky planets earth and a human's red blood cells), are primarily produced by SNe Ia.

Furthermore, SN Ia explosions inject energy into the interstellar medium, perturbing stable gas clouds, prompting gravitational collapse and promoting new generations of star formation (Mitra et al., 2015). The explosions can conversely suppress star formation by heating and driving out that same gas (White & Rees, 1978; Dekel & Silk, 1986; White & Frenk, 1991). The exact coupling between SNe Ia both chemical evolution and energetic feedback remains uncertain, but it is largely agreed upon that the events are crucial to galactic evolution, and a deeper understanding of SNe Ia would propagate directly to these questions.

1.1.2 SNe Ia as Cosmic Probes

But importance of SNe Ia goes further still beyond the physical role that they play in shaping the structure and appearance of the Universe and the galaxies that inhabit it. The observations of SNe Ia contribute fundamentally to our understanding of the large-scale structure of the Universe as well. Specifically, SNe Ia are referred to as standardizable candles because they are remarkably uniformly bright after calibrating for how quickly their light decays (Phillips, 1993, see figure 1.1.2). Additionally, because they are so intrinsically bright, we can observe SNe Ia out to large cosmic-scale distances, in far away galaxies. Plainly, if we observe an SN Ia in a galaxy, we can

Figure 1.1 A Hubble Space Telescope image of SN 1994D in galaxy NGC 4526. The image emphasizes the dramatic energy produced by a single SN Ia event because the SN is directly identifiable on the same scale as the entire NGC 4526 galaxy. This picture is also widely used in popular astronomy (such as in my PhD advisor's thesis). Credit: NASA/ESA, The Hubble Key Project Team and The High-Z Supernova Search Team.

measure precisely how far away from us that galaxy resides. This distance measuring practice has allowed us to map out the Universe and understand its large scale structure. Furthermore, this practice directly led to the discovery of the accelerating expansion of the universe and well as the
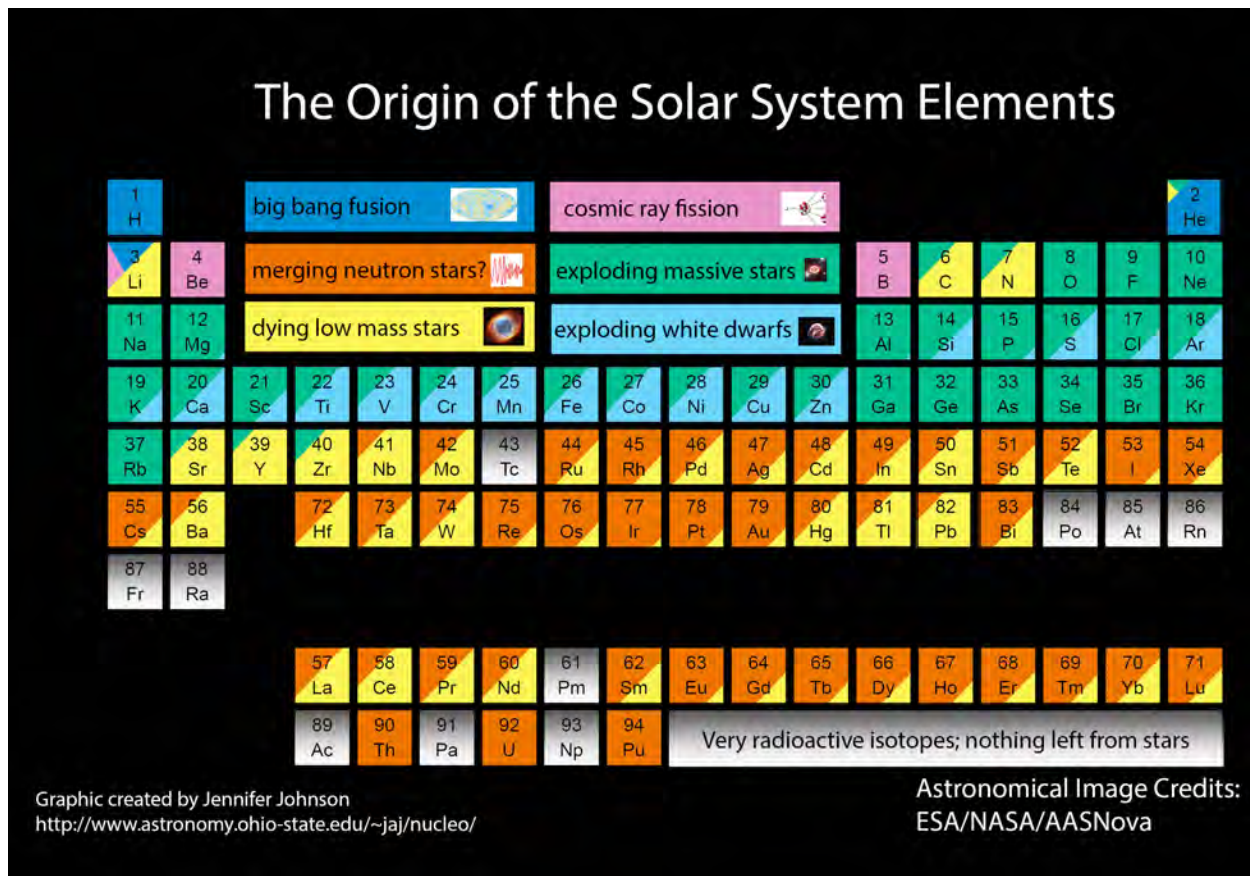
Figure 1.2 The general origin of elements in the Universe. Specific fractions are not completely certain, but this graphic generally illustrates what physical process astrophysicists believe is responsible for each element.

existence of dark energy (Riess et al., 1998; Perlmutter et al., 1999). To this day, SNe Ia provide one of the strongest constraints on two of the biggest open questions in cosmology, namely the nature of dark energy and the value of the Hubble Constant.

1.2 The SN Ia Progenitor Problem

Despite the critical role SNe Ia play both in our understanding of astrophysics and physically in the great cosmic scheme, one crucial aspect of the the events remains defiantly unconstrained. While SNe Ia are securely understood to come from thermonuclear runaway inside C/O WDs (Hoyle & Fowler, 1960; Hoeflich & Khokhlov, 1996, and see section 1.2.1), we lack a detailed description of why nuclear fusion reignites. As mentioned, WDs are very generally inert objects, and we lack a concrete physical justification for why this would suddenly change in an isolated WD
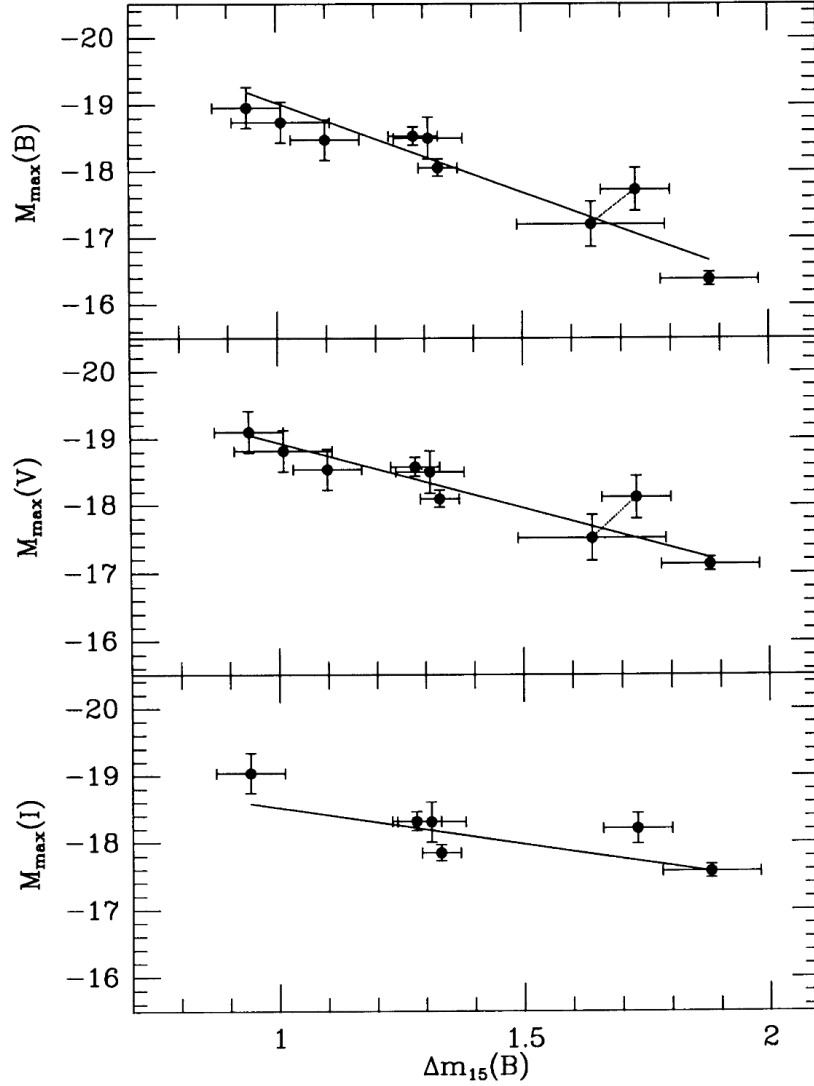
Figure 1.3 The original Phillips relation from Phillips, 1993, showing the correlation between the peak brightness and luminosity decline rate of a SN Ia. The y-axis shows the peak absolute magnitude of a specific SNe Ia in different wavelength regimes, and the x-axis shows how quickly a SN Ia fades in the B-band over 15 days.

(although see Iben & Renzini, 1983; Chiosi et al., 2015, for alternatives). It logically follows that these objects are reignited as a result of interaction with a secondary perturber[1]. Currently, in spite of decades of targeted research, that is the end of what can be securely stated (see e.g., Hoeflich et al., 1996; Maoz et al., 2014; Hoeflich et al., 2017; Blondin et al., 2017).

---

[1]Note: throughout this thesis, I will often refer to to primary and secondary objects. The primary will always be the C/O WD that explodes as an SN Ia, and the secondary will always be its companion, usually a less massive object that either donates material to the primary or is disrupted in a merger.

There are many suggested, physically motivated, and conceptually valid scenarios in which a secondary object prompts a WD to explode as an SN Ia, but which of these scenarios contribute to the SN Ia rate in nature, and in what fraction, has yet to be confirmed. To make matters worse, different conceptualizations of the SN Ia progenitor system predict dramatically different nucleosynthetic yields, which might lead to systematic biases in our predictions of galactic chemical evolution. Perhaps an even larger problem comes from the cosmological applications of SNe Ia side. The Phillips relation that underpins so much of our understanding of the Universe is empirically calibrated on our observations of nearby SNe Ia in the local Universe, because they must be verified against other methods of distance measurement. In extrapolating out to great distances, we rely on the assumption that SNe Ia behave similarly in the local and distant Universe. However, if the dominant progenitor system of SNe Ia changes between the early and present Universe, then the Phillips relation might no longer apply. Indeed, despite our best efforts, the current constraint on the Hubble Constant from SNe Ia distance measurements remains in 5-σ tension with independent measurements deriving from power spectrum fluctuations of the cosmic microwave background (Riess et al., 2022), and this could be due in part to an incomplete understanding of SNe Ia. To solidify our understanding of the Universe we must begin by unraveling the SN Ia progenitor system. Providing additional evidence towards this goal is the primary aim of this thesis.

1.2.1   The Confirmed Half of the SN Ia System

To understand how to confirm any given progenitor system of SNe Ia, we must first discuss what the viable physical progenitor systems are. As mentioned previously in this chapter, the most well understood component of the progenitor system is that a C/O WD explodes to create the SN Ia (see e.g., Hoyle & Fowler, 1960; Whelan & Iben, 1973; Livne, 1990). This is because the thermonuclear runaway of a C/O WD uniquely satisfies multiple observable signatures of SNe Ia events including the following:

1. The light curve, or luminosity over time, of an SN Ia can be reproduced almost exactly by the decay of radioactive ^{56}Ni into ^{56}Co and then to ^{56}Fe after taking into account the delay of light propagating through expanding SN ejecta (Meyerott, 1978, 1980; Axelrod,

1980). Furthermore, this physical explanation conveniently explains the Phillips relation, as more massive progenitor systems could produce more ^{56}Ni, and also synthesize more iron group elements which increases opacity of the ejecta and a resulting delay of light curve development (Arnett, 1982; Mazzali et al., 2001). The thermonuclear runaway of a C/O WD has been shown by simulations to readily produce this feature.

2. Spectra of SNe Ia are remarkably absent of Hydrogen features. While not directly indicative of a progenitor, because Hydrogen is the most abundant element in the Universe, very few astrophysical environments are depleted of Hydrogen. The Hydrogen deficient nature of C/O WDs conveniently explains this absence.

3. Observations of at least one specific SN Ia have ruled out non-degenerate stellar progenitors (Bloom et al., 2012).

4. SNe Ia are observed to occur regardless of whether the host stellar population is young or old, with no strong preference with respect to active star formation Mannucci et al. (2006). This property suggests that SNe Ia are able to occur in hosts long after star formation has ceased.

5. When considering WDs, simulations have shown that the explosions of less massive He WDs do not produce chemical compositions that can match SNe Ia nucleosynthetic yields (Nomoto & Sugimoto, 1977). In the other direction, more massive O-Ne-Mg WDs are difficult to make explode, and instead favor direct collapse into neutron stars (Nomoto & Kondo, 1991).

This combination of properties overwhelmingly suggests that SNe Ia arise from the thermonuclear runaway of C/O WDs. The uncertainty in the progenitor system instead lies in the identity of the WD's companion (Maoz et al., 2014; Maeda & Terada, 2016; Liu et al., 2023).

1.2.2 Theoretical Progenitor Systems of SNe Ia, or the Other Half

As the literature has securely established the identity of the exploded star itself, we must return to the reason that nuclear fusion reignites, or what specific process causes a C/O WD to explode as an SN Ia. Currently, there are three popularly supported scenarios that could lead to the re-

ignition of the WD which differ primarily in two ways: The identity of the companion, and how the companion interacts with the primary WD. The scenarios are each known by multiple names, but in this thesis they will be referred to as the Single Degenerate Scenario, the Double Degenerate Scenario, and the particularly noteworthy subclass of the double degenerate scenario known as the Dynamically-Driven Double-Degenerate Double-Detonation (D6) scenario. I will describe each of them in turn.

1.2.2.1   The Single Degenerate (SD) Scenario

As the name implies, in the SD scenario the degenerate WD interacts with a non-degenerate companion which could be any of a main sequence, sub giant, red giant, asymptotic giant branch, or helium (He) star (see e.g., Whelan & Iben, 1973; Nomoto, 1982a; Nomoto et al., 1984; Iben et al., 1987; Hachisu et al., 1999; Livio, 2000; Han & Podsiadlowski, 2004). This scenario can broadly be described by stable mass accretion onto the primary C/O WD through a process called Roche-lobe overflow. As the WD siphons material from the secondary, it steadily grows in mass. Electron degeneracy supported stars have an unusual property in that the more massive the star becomes, the smaller it will shrink. This property continues up to a theoretical maximum mass known as the Chandrasekhar mass at which the star would theoretically become a point mass at about 1.4 $M_\odot$ (Chandrasekhar, 1931), and the steady accretion of the WD pushes it towards this limit. However, on the path towards Chandrasekhar mass around 1.38 $M_\odot$, the WD obtains a central density high enough to restart nuclear fusion. Once burning begins, thermonuclear runaway follows and the WD explodes as an SN Ia. This scenario was widely regarded as the most likely SN Ia progenitor scenario for between two to three decades, and as a result it has been the most well studied and scrutinized of the three I will highlight (see e.g., Livio & Mazzali, 2018, for review).

1.2.2.2   The Double Degenerate (DD) Scenario

The double degenerate (DD) scenario broadly encompasses all scenarios in which the secondary, like the primary, is a degenerate object (i.e., a WD). A double WD system can lead to a SN Ia explosion in one of three ways. Classically, this scenario details the tidal disruption of a secondary WD as it is brought close to the primary WD through gravitational wave emission (Iben & Tutukov,

1984; Webbink, 1984). Here, the secondary may be accreted onto the primary, raising the central density of the primary enough to reignite nuclear fusion, similar to in the SD accretion scenario. It is unclear if this remains a viable SN Ia progenitor scenario, however, because simulations have suggested that this scenario leads to the accretion induced collapse of the WD into a neutron star instead (Saio & Nomoto, 1985; Nomoto & Iben, 1985; Schwab et al., 2016; Schwab, 2021).

Departing from the classic DD scenario, more recent conceptualizations have emerged that are able to produce SNe Ia. Rather than relying on accretion that raises the central density of the primary WD, some simulations have suggested that the primary will explode in the process of merging with secondary, known as the "violent merger scenario" (Pakmor et al., 2010, 2012; Sato et al., 2015). Another similar scenario has been proposed in which the primary and secondary collide head-on as a result of interactions with a third body that lead to highly eccentric orbits (Rosswog et al., 2009; Raskin et al., 2010). While possible, this variation is complicated by the necessity of the third object and would likely only frequent in dense stellar environments, which don't appear favored by general SNe Ia.

1.2.2.3 The Dynamically Driven Double-Degenerate Double-Detonation (D6) Scenario

Finally, I would like to highlight a specific conceptualization of the DD scenario that has received significant attention in recent times. In this scenario, known as the Dynamically Driven Double-Degenerate Double-Detonation (D6) Scenario, the secondary must be He rich in its outer layers, either a He WD or a hybrid HeCO WD. In this scenario, on the path to merger, the primary accretes a thin He shell which detonates and compresses the object. This squeezes the center, momentarily raising the central density enough to prompt a second detonation and produce an SN Ia (Bildsten et al., 2007; Guillochon et al., 2010; Dan et al., 2011; Pakmor et al., 2013, 2021, 2022; Roy et al., 2022). This scenario has risen to the forefront of the SN Ia progenitor debate and Chapter 2 is dedicated to investigating this scenario.

1.2.3 The State of the Field

Observations of normal SNe Ia appear remarkably uniform, and it would be a startling coincidence if multiple physically distinct channels were able to reproduce this uniformity[2] (however, see Wojtak et al., 2023, for discussion that SNe Ia may be better explained by a combination of two distinct populations). In light of the wide variety of physical systems that have been suggested to give rise to SNe Ia, one thing is clear. Observations must be compared to the distinct theoretical predictions of the various potential SNe Ia progenitor scenarios in order to discriminate between them and unravel the mystery of the SN Ia progenitor problem. This goal has been the goal of decades of research in the SN Ia field and is also a primary focus of this thesis. Despite extensive effort, it has proven difficult to confirm or comprehensively falsify even one individual progenitor channel (see e.g. Maoz et al., 2014; Maeda & Terada, 2016; Livio & Mazzali, 2018, for review).

I will now highlight a few attempts at distinguishing between progenitor scenarios to get a high level sense of where the field currently stands. The following were tests of the single degenerate scenario, and largely point towards the non-existence of such an object:

- Olling et al. 2015 examined three early time SNe Ia light curves for evidence of interaction between the ejecta and a companion and did not find evidence of a such a star.

- Tucker et al. 2020 looked for stripped companion emission in late-phase spectra of SNe Ias and did not find any.

- Tucker & Shappee 2024 did not see emission near the center of the nearby SN Ia 2011fe out to 11.5 yrs post explosion, where a non-degenerate companion should be clearly visible.

- Gilfanov & Bogdán 2010 examined nearby elliptical galaxies for X-ray radiation that should come from the single degenerate system for 100 yrs before the WD explodes as a SN Ia, and did not detect a large enough flux to explain the SN Ia rate.

---

[2]I would be remiss to omit the fact that there exist many distinct subclasses of SNe Ia not considered in this work. While variations of these scenarios almost certainly cannot all explain normal SNe Ia, some scenarios may and likely do map onto specific SN Ia subclasses.

- Woods et al. 2017 looked for evidence of the same X-rays as the previous study, instead by looking for traces of H recombination around Tycho's SNR (SN 1572). The X-rays emitted would have ionized the surrounding gas, which would recombine on timescales similar to SNR lifetimes and be visible around the Tycho remnant.

While the previous studies point away from the single degenerate scenario, attempts to confirm a double degenerate scenario have not proved significantly more fruitful. It is worth stating that, while the single degenerate scenario possesses a plethora of directly testable observational signatures, the double degenerate scenario is much more difficult to observationally confirm. A WD-WD merger is an interaction between two compact, faint objects which makes direct observations challenging (Rebassa-Mansergas et al., 2019). Perhaps one of the most promising testable predictions of the double degenerate scenario is instead in the expected asymmetry of the explosion ejecta. However, observations of SN ejecta have been shown to be significantly less asymmetric than simulations would predict (Bulla et al., 2016b,a).

There have also been significant attempts recently to distinguish between progenitor systems by mapping progenitor models onto chemical abundance profiles of the ejecta, and comparing those profiles to the abundances measured in SN Ia ejecta (O'Brien et al., 2021, 2024). These approaches appear promising, but are confined by the exact details of the progenitor system to abundance mapping which is a challenging problem on its own.

1.3 Surviving Companions as Probes of the Progenitor System

One of the single most powerful discriminants between progenitor scenarios is the detection of a surviving companion to the exploded star. While the exact identity of the companion is uncertain, virtually all suggested surviving companions are expected to be perturbed for up to hundreds of kiloyears, which should make those companions disguinshable against the general stellar population. For instance, during mass accretion, the secondary may experience tidal forces that heat the star (Shen & Schwab, 2017). During the explosion, the secondary will be impacted by ejecta which may strip the star's outer layers (Marietta et al., 2000) or deposit energy in to its envelope which will cause it to inflate (Liu et al., 2021). Ejecta that settles on the star will

contain radioactive elements which continue to inject energy in to the envelope (Shen & Schwab, 2017), and the high metal content of that ejecta will contaminate the photosphere which should be directly measurable (Ozaki & Shigeyama, 2006). In the event of a detection of an unambiguous companion due to one of these properties, the identity of the companion would directly confirm a specific progenitor channel (e.g., a main-sequence companion would confirm the SD scenario). More accurately (and conveniently), the surviving companion should be identified in a location where it can be unambiguously linked to SN Ia event.

Most SNe Ia that we observe occur in galaxies too far away to allow for the study of individual stars. Furthermore, SN Ia rates predict that an SN Ia should occur in our Galaxy roughly once every hundred years, so the prospects of observing a new SN Ia and identifying its companion are relatively low, though non-zero, within our lifetimes. Fortunately, SN Ia leave behind clear identifiable evidence of where they occurred in the form of remnants which persist for around 10^6 years. These remnants alone are of considerable scientific interest, and they can be studied kinematically to tell us precisely how old the remnants are (see e.g., Arunachalam et al., 2022; Guest et al., 2023). Furthermore, Supernova remnants (SNRs) can be traced back to specific types of SNe through signatures like their chemical compositions (Martínez-Rodríguez et al., 2020) or spectroscopic identification of the historical SNe that created the remnants, made possible by observing light reflecting off particles surrounding the remnant(Rest et al., 2005a, 2008a, 2012). Armed with secure type classifications, astrophysicists can search SNRs Ia for surviving companions.

An SNR surviving companion search can have two obvious outcomes. First, and most tantalizingly, a surviving companion could be detected. Such an identification would immediately revolutionize the SN Ia field and make significant headway into unraveling the SN Ia progenitor problem. Second, a surviving companion could not be detected. In this case, the constraining power of the surviving companion search comes from the limits placed on the existence, or more specifically the non-existence, of certain types of stars within the remnant. In astronomy virtually all observations are limited by the depth of those observations. That is, there may always be a fainter

object just beyond detection limits, that may have been discovered with a more powerful telescope or a longer observation. By understanding exactly those limits, we can turn this around to make concrete statements on the non-existence of objects. If we would have observed any object brighter than some limiting magnitude, then we can rule out the existence of those objects in the portion of the sky that we observed. Specific to our case here, if an SN Ia progenitor scenario predicts the existence of a specific type of surviving companion, then if that star would have been conclusively seen and identified in our observations but was not, we can state that that progenitor scenario is not responsible for the SN that created that remnant. Further still, with systematic investigations of large numbers of remnants, we can make powerful statistical arguments that certain progenitor scenarios are not responsible for the majority of, or possibly any SNe Ia. But all of that relies upon our ability to conclusively rule out the existence of a specific type of surviving companion. This can only be done with the careful treatment of detection limits as well as the study of each and every star potentially affiliated with the SN Ia event. In other words, if every star in a given remnant cannot be ruled out as a surviving companion, then we cannot make conclusive statements about SNe Ia progenitor scenarios.

1.3.1 Galactic SNRs and Surviving Companion Searches

There are, in total, about 300 known SN remnants in our galaxy (Green, 2019), and a significant fraction of these should be the remnants of SNe Ia. Unfortunately for our purposes, SNRs generally trace stellar populations, which means that the vast majority of SNRs are scattered throughout the Galactic disk. This property leads to two major problems.

First, both remnants and stars residing within the plane of the galaxy have, until recently, been prohibitively difficult to systematically estimate distances to. This leads to intractable numbers of foreground and background interlopers that may appear to reside visually within a remnant, but are truly unrelated. The recent Gaia mission (Collaboration et al., 2016, 2018; Gaia Collaboration et al., 2021) has measured distances to billions of stars within our Galaxy, but distances to remnants themselves are still largely unconstrained.

Second, but perhaps more importantly, the largest obstacle to investigating most Galactic SNRs

is the presence of otherwise mundane dust particles. The dense parts of galaxies like our Milky Way are filled with dust, which obscures starlight through a process called extinction (see Figure 1.3.1). In optical wavelength regimes, foreground dust between us and remnants reduces the intensity of stars that we observe by a factor of tens in the best cases and by hundreds to over tens of thousands in typical cases. In such cases where foreground dust is not prohibitive, detailed dust modeling must be taken into account in order to understand stars that inhabit remnants. But the problem escalates when foreground dust and uncertain distances are combined. Uncertain distances to stars and remnants makes it prohibitively difficult to estimate foreground dust even if the foreground dust is otherwise constrained. Without both concrete foreground dust estimates and concrete distance estimates, comprehensive investigation of more than tens to hundreds of stars becomes impossible with current limitations.
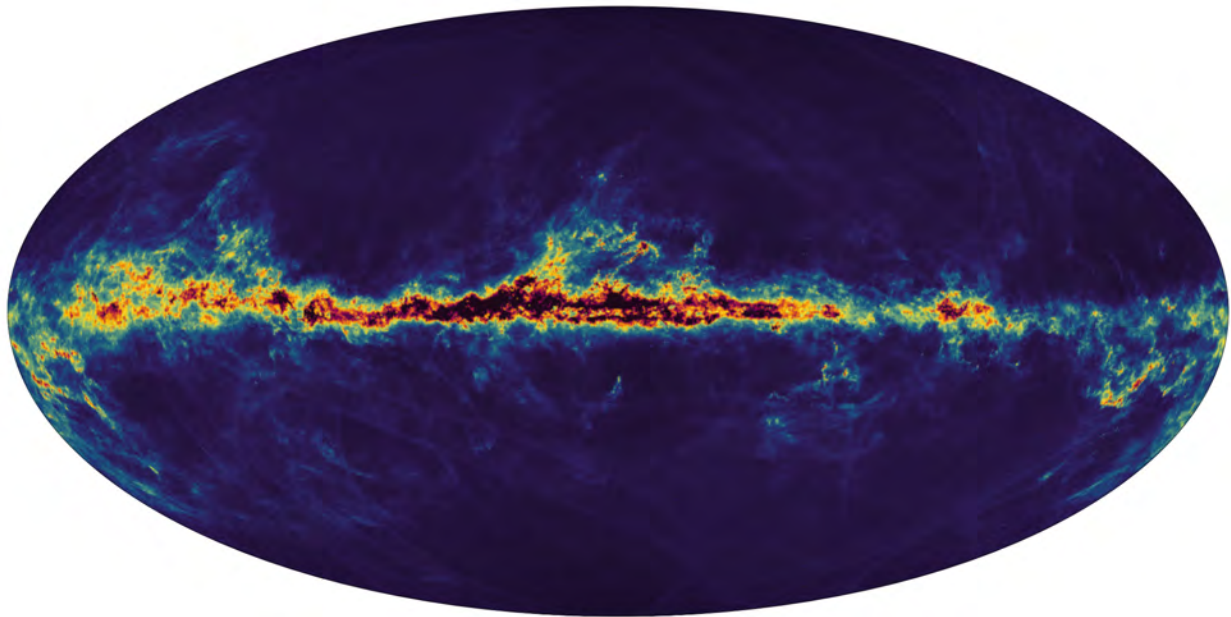
Figure 1.4 A milky way dust map created with Gaia. Dust can be seen to trace the shape of the Galaxy, and most stars in the Galactic bulge is impossible to see through in most wavelengths. ESA/Gaia/DPAC; CC BY-SA 3.0 IGO

All said, a small handful of Galactic SNRs have been comprehensively examined and searched for surviving companions (see e.g., Ruiz-Lapuente, 2019, for review). This work adds one more Galactic surviving companion search to the sample in Chapter 2, as well as one extragalactic

surviving companion search in Chapter 3 in the Large Magellanic Cloud (LMC).

1.4 Stars as Physical Probes and the Importance of Stellar Modelling

The primary focus of this thesis is unraveling the SN Ia progenitor problem. However, the astute reader may have already noticed that the primary concern of this thesis includes virtually no observations of SNe themselves. Instead, my work has focused on learning about SNe through observations of individual stars and their subsequent characterizations. All the inferences drawn throughout this thesis (and indeed throughout most branches of astrophysics) rely on our understanding of stellar observations. This understanding is built upon physical models of stars beginning with their physical structure (i.e., the temperature and density profile of the steady state gravitationally bound ball of plasma) and ending with the photons that escape that structure and travel to our telescopes. Solving a model of the former entails solving hydrodynamic equations to satisfy the conditions of hydrostatic equilibrium and is an important undertaking that is outside the scope of this work. The latter is the classic problem of radiative transfer applied to the plasma of stellar atmospheres and is a major component of this thesis.

Stellar radiative transfer codes have existed and enabled a large body of research in the astronomical community, but they by and large are either difficult to interact with, impossible to find, or difficult to evolve to the changing needs of the modern astrophysicist. Often they are carefully and reasonably calibrated to reproduce the spectra of ordinary stars, but the assumptions incorporated into them may not extend to non-standard use-cases. For instance, in Chapter 3 I use photometry to broadly characterize the effective temperature and radii of stars. The coarse measurements therein allowed me to neglect a careful treatment of the physics necessary to correctly model the highly non-standard atmospheres of surviving companions. But in order to do full spectral synthesis capable of accurately predicting surviving companion spectral observations, a new stellar spectral synthesis code is needed. While my use case highlighted here is a single example, it illustrates the larger need of the astrophysics community for a modern offering to the ever present problem of stellar radiative transfer. To enable the next generation of stellar research and bring stellar radiative transfer into the current 21st century, I began working on this problem.
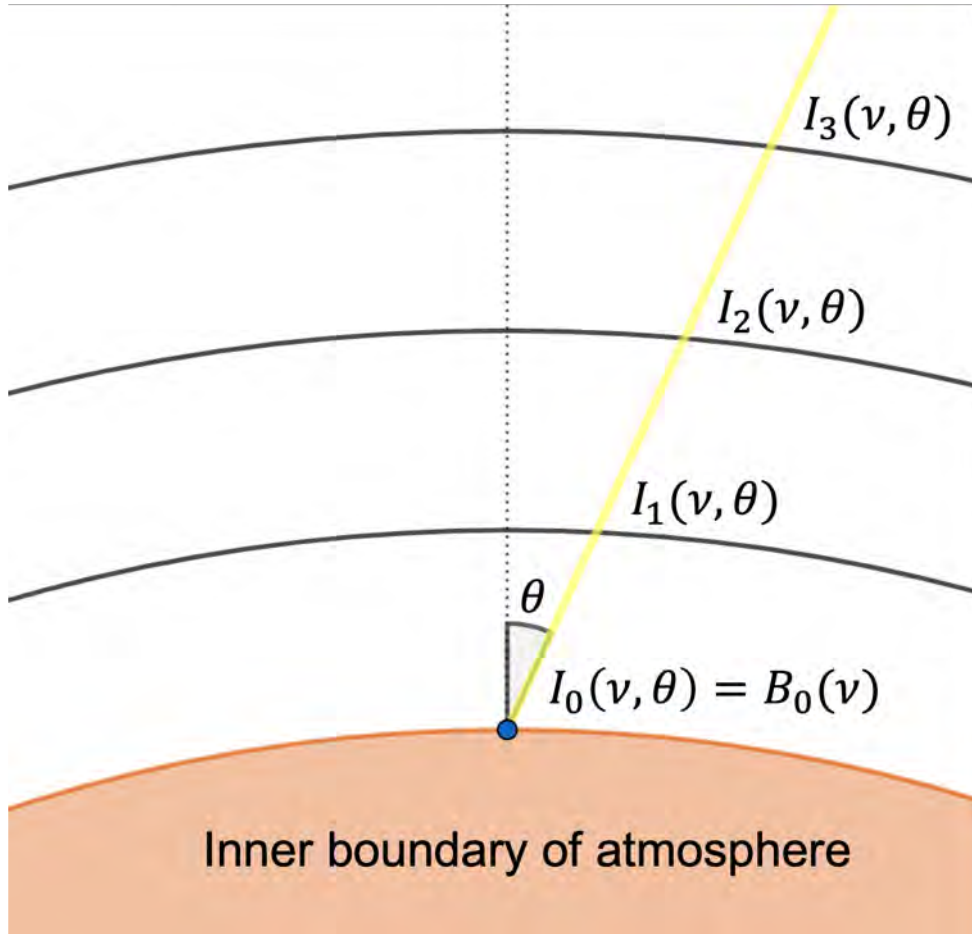
Figure 1.5 A cartoon diagram depicting ray tracing at an angle through the stellar atmosphere. Source: STARDIS Documentation

The last major work of this thesis, presented in Chapter 4, details the release of a new 1D open-source finite-difference stellar atmospheric spectral synthesis python code called STARDIS. The code solves the state of plasma, taking the temperature, density, and chemical composition of the atmosphere as inputs. Then, the code solves for the attenuation of beams of light at each step through the atmosphere to obtain a detailed spectrum produced by a star (see Figure 1.4 for a cartoon illustrating the ray tracing process). The code is designed to be modular, allowing for the input of additional physics as needed by the user.

1.5   Outline

The following chapters contain works for which I am the primary intellectual contributor. Chapter 2 details the surviving SN Ia companion investigation of the Galactic SNR Ia called SN

1006. That work specifically seeks to test the D6 scenario by searching for a hypervelocity white dwarf predicted by that scenario. That work rules out the existence of such a star, supporting the conclusion that the SN 1006 remnant was not created by the conceptualization of the D6 scenario tested. Chapter 3 details another surviving companion investigation, this time in the LMC remnant SNR0509-67.5. That investigation more broadly seeks to identify any type of surviving companion broadly above the detection limits of for the archival HST observations examined. While this study also did not detect a surviving companion, the non-detection points to the strong conclusion that the SN Ia progenitor scenario that created the SNR0509-67.5 remnant does not produce a surviving companion altogether. Chapter 4 details a new stellar radiative transfer code intended to be able to accurately model, among other things, the starlight produced by surviving companions. More generally, the code aims to provide astrophysicists with a new tool suitable for modern stellar modeling, and increase scientific productivity for those whose work requires synthetic stellar spectra in the coming years. Finally, In Chapter 5 I begin by summarizing this dissertation and the content of each chapter, and then describe the future directions of both the surviving companion work and the planned extensions of the STARDIS code, as well as the upcoming research that it will enable.

CHAPTER 2

SEARCHING FOR A HYPERVELOCITY WHITE DWARF SN IA COMPANION: A PROPER MOTION SURVEY OF SN 1006

This section reviews the published work of Shields et al. (2022)
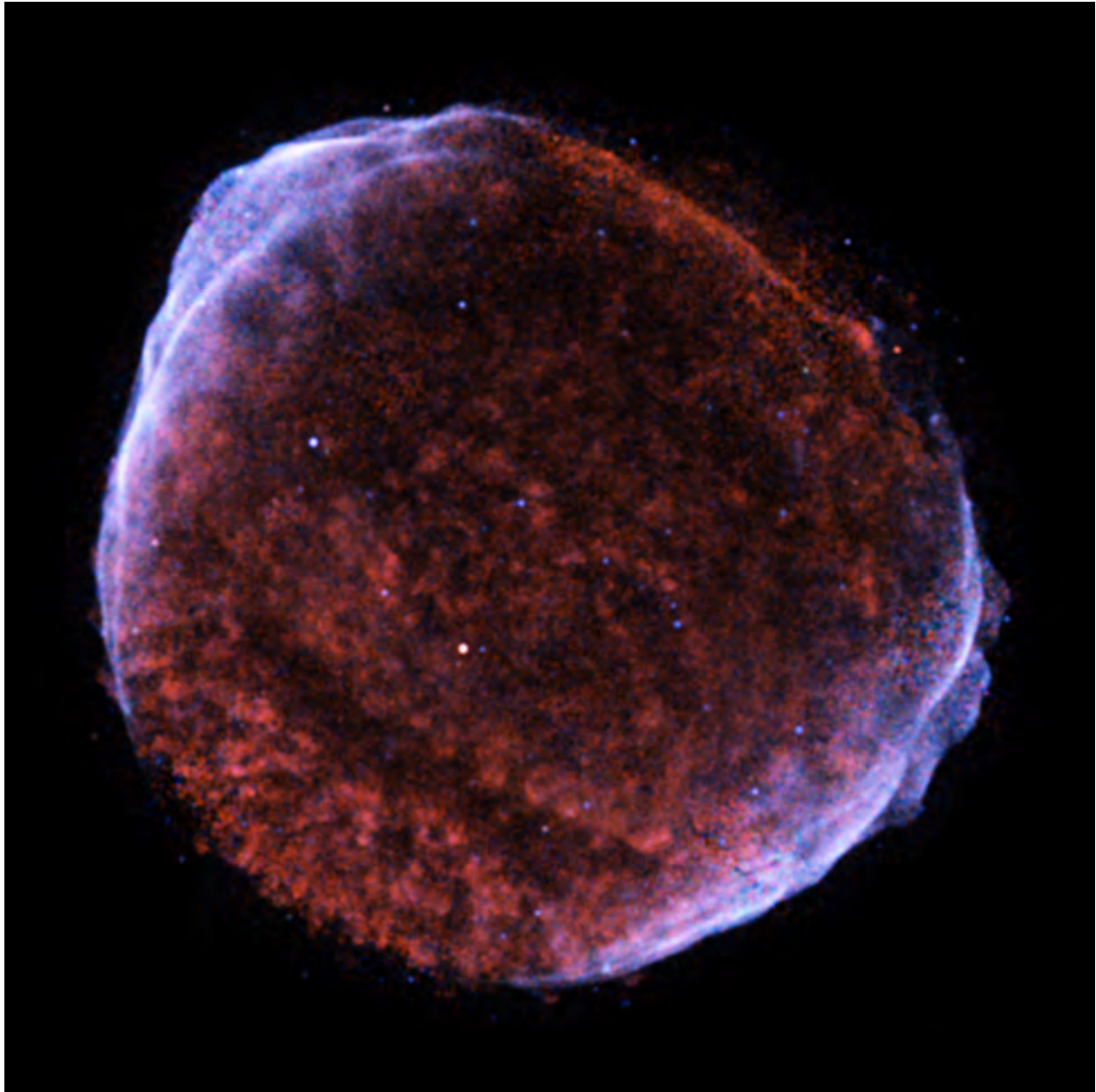
Figure 2.1 The SN 1006 remnant. Credit: NASA/CXC/Rutgers/J.Hughes et al.

2.1 Abstract

Type Ia Supernovae (SNe Ia) are securely understood to come from the thermonuclear explosion of a white dwarf as a result of binary interaction, but the nature of that binary interaction and the secondary object is uncertain. Recently, a double white dwarf model known as the dynamically driven double-degenerate double-detonation (D6) model has become a promising explanation for these events. One realization of this scenario predicts that the companion may survive the explosion and reside within the remnant as a fast moving ($V_{peculiar} > 1000$ km s^{-1}), overluminous ($L > 0.1L_\odot$) white dwarf. Recently, three objects which appear to have these unusual properties have been discovered in the Gaia survey. We obtained photometric observations of the SN Ia remnant SN 1006 with the Dark Energy Camera over four years to attempt to discover a similar star. We present a deep, high precision astrometric proper motion survey of the interior stellar population of the remnant. We rule out the existence of a high proper motion object consistent with our tested realization of the D6 scenario ($V_{transverse} > 600$ km s^{-1} with $m_r < 21$ corresponding to an intrinsic luminosity of $L > 0.0176L_\odot$). We conclude that such a star does not exist within the remnant, or is hidden from detection by either strong localized dust or the unlikely possibility of ejection from the binary system near parallel to the line of sight.

2.2 Introduction

Type Ia supernovae (SNe Ia) are well-studied, highly energetic events that are fundamental drivers of galactic chemical enrichment (Timmes et al., 1995; Nomoto et al., 2013; Kobayashi et al., 2020) and that led to the discovery of the accelerating expansion of the Universe by allowing for secure measurements to distant galaxies (Riess et al., 1998; Perlmutter et al., 1999). Despite the central role that these energetic events play in our understanding of the Universe and decades of focused research (e.g. see Maoz et al. 2014; Ruiz-Lapuente 2019), we still do not know the progenitor system and explosion scenario that creates these events. SNe Ia arise from a carbon/oxygen white dwarf undergoing thermonuclear runaway (Pankey, 1962; Colgate & McKee, 1969), but the circumstances that lead to this condition are uncertain. A misunderstanding of the underlying physics will result in uncertainties in our understanding of the Universe that is built

19

upon these events.

SNe Ia progenitor scenarios are divided into two broad classes. In one major scenario, a white dwarf violently merges with a secondary white dwarf which leads to explosion (Iben & Tutukov, 1984; Webbink, 1984). In the other, the primary white dwarf accretes material from a nearby secondary which also prompts thermonuclear runaway. This accretion scenario has many variations, with the secondary being either degenerate (Dan et al., 2011) or non-degenerate (Whelan & Iben, 1973; Nomoto, 1982b; Iben et al., 1987; Livio, 2000). Significant work has been done attempting to disentangle progenitor scenarios and discover which, if any, of these processes are progenitors of SNe Ia, but finding strong support for any specific scenario has proven difficult (see Ruiz-Lapuente 2019 for detailed discussion). One crucial, directly testable prediction comes from the secondary star in the binary system. In the violent merger scenario, the secondary is expected to be completely disrupted, while many accretion scenarios make the strong prediction that the secondary survives the explosion and exists within the resulting SN Ia remnant.

Identification of a surviving companion would lend powerful support to a corresponding accretion scenario based on the properties of the companion star (Marietta et al., 2000; Pakmor et al., 2008; Shappee et al., 2013a; Pan et al., 2012, 2013). Galactic SN Ia remnants have been the subject of much scrutiny to discover a surviving companion, but no such companion has been unambiguously identified (e.g. see Ruiz-Lapuente et al. 2004, 2018, 2019; Ihara et al. 2007; Hernández et al. 2009; Kerzendorf et al. 2009, 2014, 2018a; Schaefer & Pagnotta 2012). These works focused on identifying bright, non-degenerate companions tying back to the non-degenerate accretion scenario. However, mounting evidence including, but not limited to, non-detection of signatures of a non-degenerate companion in early (Hayden et al., 2010; Bianco et al., 2011; Bloom et al., 2012; Zheng et al., 2013; Olling et al., 2015; Marion et al., 2016; Shappee et al., 2016, 2018; Cartier et al., 2017; Miller et al., 2018; Holmbo et al., 2019; Fausnaugh et al., 2021) as well as late times (Mattila et al., 2005; Leonard, 2007; Shappee et al., 2013b; Lundqvist et al., 2013, 2015; Sand et al., 2016, 2018; Graham et al., 2017; Maguire et al., 2016; Woods et al., 2017; Vallely et al., 2019; Tucker et al., 2020), disfavor the non-degenerate accretion scenario as an explanation for the bulk of SNe

Ia, aligning with the non-detection of a non-degenerate surviving companion. Coincidentally, most surviving companion searches did not go deep enough to discover faint degenerate companions (e.g. white dwarfs) which have recently come to the forefront of the SNe Ia progenitor debate.

In this work, we test a specific realization of the Dynamically Driven Double-Degenerate Double-Detonation (D6) scenario (Guillochon et al., 2010; Pakmor et al., 2010, 2013; Shen & Bildsten, 2014). In this scenario, the primary CO white dwarf undergoes unstable He accretion from a secondary degenerate He or CO white dwarf companion. The primary forms a thin He shell that detonates, which compresses the star and triggers thermonuclear runaway. If the He shell detonates early on in the accretion process, the secondary will survive the explosion and be flung out of the system with a minimum velocity of 1000 km s^{-1} (Shen et al., 2018), significantly above that inherited by normal processes of stellar evolution barring specific dynamic interactions in the galactic center which are exceedingly rare (Hills, 1988; Brown, 2015; Generozov & Perets, 2022). Shen et al. 2018 discovered three hypervelocity white dwarfs in the field in the Gaia mission (Collaboration et al., 2016, 2018) that lie in a peculiar region of the color luminosity diagram, aligning with this realization and providing the most powerful observational support that any progenitor scenario has seen. Combined with the mounting evidence against other established SNe Ia progenitor scenarios, this discovery suggests the possibility that most if not all normal SNe Ia arise from the D6 scenario.

This scenario provides a testable hypothesis. If this realization of the D6 scenario is the generic explanation for SNe Ia, each SN Ia remnant must contain such a surviving companion. The SN ejecta that forms the remnant is ejected with a mean velocity $V_{ejecta,mean} \simeq 5000$ km s^{-1}, and a maximum velocity $V_{ejecta,max} \geq 20\,000$ km s^{-1} (see e.g. Hillebrandt & Niemeyer 2000), far above the surviving companion's velocity. The ejecta slows upon colliding with the surrounding interstellar medium, but still leaves the companion contained by the SN remnant. We intended to test this realization of the D6 scenario by searching for a surviving D6 companion inside the SN 1006 remnant, which is uniquely suited for such a search. Galactic SN remnants generally trace the stellar population and therefore reside primarily within the Galactic plane (mean and standard

deviation of Galactic remnant latitudes b = 0.117 ± 2.787 deg, Green 2019), which creates two significant problems: First, the Galactic plane is heavily obscured by dust and is prohibitively difficult to search for faint, blue objects (e.g. white dwarfs, see Ruiz-Lapuente et al. 2018) with current observational constraints. Second, there is a high density of contaminating foreground and background interlopers which has two effects. The high density can contribute to source confusion and force the search to include sources which cannot be placed in front of or behind the remnant, obfuscating the search to the point of unfeasibility. SN 1006 uniquely resides nearby and high above the galactic plane with a galactic latitude b = 14.6 deg and a distance d = 2.17 ± 0.08 kpc (Winkler et al., 2002)[1], leading to shallow foreground extinction (A_v = 0.2154 ± 0.0564) and relatively little source confusion. Furthermore, a star moving 1000 km s^{-1} in a transverse direction at such a close distance would show a very strong proper motion signal of 97.2 mas yr^{-1}, far above normal positional uncertainties of high precision astrometric measurements. These properties indicate that a high velocity D6 companion will be observable within the remnant if one exists.

There have been multiple previous searches in SN 1006 for surviving companions, but they largely focused on discovering bright, non-degenerate donors and did not go deep or wide enough to discover a compact high velocity object in line with the predictions of the D6 scenario (e.g. Hernandez et al. 2012 down to m_r = 15, Kerzendorf et al. 2012 down to m_v = 19 but a search radius r = 2 arcmin). Furthermore a D6 star in SN 1006 would have only had about 10^3 years to evolve, orders of magnitude less time than the three candidates discovered in the field in Shen et al. 2018 which are thought to be at least 10^5 yr post explosion. Liu et al. 2021 showed that a D6 star will be significantly overluminous within 10^4 years, but the appearance of a D6 star as young as in SN 1006 has not yet been observed, and an unusually high velocity remains the strongest signature of such an object. While Kerzendorf et al. 2018b went down to m_r = 21 and directly sought to investigate the possibility of a white dwarf companion, a young D6 star's heavily uncertain appearance in color and luminosity could mean that it resides far off the standard white dwarf cooling track, which might have caused the star to elude this analysis as well.

---

[1]We note that there is some ambiguity on the distance to the remnant. Kerzendorf et al. 2018b report the distance as 2.07 kpc ±0.18, but Winkler et al. 2002 report 2.17 ±0.08. We adopt this distance for the remainder of this work.

In this work, we present a deep four year baseline astrometric proper motion survey of the stars inside SN 1006 using the Dark Energy Camera (Diehl, 2012; Flaugher et al., 2015) to find the surviving companion predicted by the Shen et al. 2018 realization of the D6 hypothesis. We measured and report the proper motions of over 2000 objects beyond the detection limit of Gaia.

In Section 2.3, we present our observations and initial data reduction. In Section 2.4, we detail our astrometry and proper motion extraction. In Section 2.5, we present the results of our survey and the constraints on a surviving companion in SN 1006 that follow. In Section 2.6 we consider confounding possibilities of non-detection and discuss high proper motion objects identified in our search. We conclude by summarizing our findings and discussing future work in Section 2.7.

2.3 Observations & Data Reduction

For our work, we acquired pre-existing photometry of the SN 1006 remnant from the nights of Jan 30 2017 and May 22 2018, and obtained new observations of the remnant on the night of Jan 22 2021. All data was captured using the Dark Energy Camera (Diehl 2012, Flaugher et al. 2015) instrument mounted on the 4-m Blanco telescope located at the Cerro Tololo Inter-American Observatory (CTIO). Exposures were taken in 5 bands, but all data processing and analysis was performed on r-band observations to minimize atmospheric scattering as well as foreground dust extinction, allowing for higher astrometric accuracy and better measurements of faint, reddened sources. All r-band exposures were 50 seconds, stacked to create combined exposure times of 250 or 300 seconds depending on epoch.

After standard calibration (bias correction, flat-fielding, and WCS) was done by the NSF NOIRLab DECam Community Pipeline (Valdes et al., 2014), we reduced the data using the `Photpipe` pipeline as described in Rest et al. (2005b, 2013): Images were warped into a tangent plane of the sky using the "SWarp" routine (Bertin et al., 2002), before photometry of the stellar sources is obtained using the standard point spread function (PSF) fitting software DoPHOT (Schechter et al., 1993). We obtained observations of standard stars on the same nights as the photometric catalogues, which we used for calibration to obtain our photometric zeropoints.

Each epoch was comprised of either 5 or 6 dithered observations which were combined for each

of the 62 individual CCDs. Multiple observations of the same star within one pixel coordinate (0.263 arcseconds) were matched and combined. Additional details about this initial matching are given in Appendix 2.8.2. Final stellar positions were then calculated using uncertainty weighted averages in both CCD pixel dimensions, and their uncertainties co-added using standard uncertainty propagation rules, decreasing uncertainties by a factor of $1/\sqrt{N}$. We note that, as dithering patterns did not observe all sources in each image, this factor was inconsistent depending on source position inside a CCD. With secure single epoch catalogue positions, we then needed to cross match sources across epochs to identify their movement and extract proper motions.

2.4 Methodology & Analysis

A source moving inside SN 1006 at 1000 km s^{-1}, the minimum velocity in line with the predictions of the D6 scenario (Shen et al., 2018), would have a proper motion of 97 mas yr^{-1} assuming our chosen distance to the remnant of 2.17 kpc. We initially set out to discover any star within SN 1006 with a proper motion higher than 80 mas yr^{-1} with no further restrictions other than being bright enough to be measurable in the DECam imagery. To recover proper motions with sufficient signal to noise to identify a surviving companion, we needed to discover a transformation from each individual instrumental CCD reference frame into one common reference frame. We chose to use the Gaia EDR3 catalogue (Gaia Collaboration et al., 2021) to establish this common astrometric reference frame because it is currently the publicly available catalogue with the most precisely measured positions of the stars inside the remnant.

2.4.1 Building Our Proper Motion Catalogue

We began by identifying a grid of 16 bright stars on each CCD with relatively small astrometric position uncertainties (see Equation 2.1 in Appendix 2.8.1) that could be matched between our DE-Cam and Gaia source catalogues. We used these as an initial guess for a second-degree polynomial (12 free parameters) that transforms from our DECam pixel coordinates to Gaia ICRS coordinates. Using this initial guess, we matched additional sources within one arcsecond (3.8 pixels) and one magnitude in the DECam and Gaia catalogues and refit the polynomial transformation. We note that Gaia G-band and DECam r-band are different filters, but we found that empirically the two

bands are similar (r-band magnitude and G-band magnitude have a mean difference of 0.02 mag in our sample). The filters are also centered on similar wavelengths. Additionally, the magnitude matching was only used as a conservative safeguard against spurious matches. We finally performed a second iteration of this fitting process, matching the DECam catalogue to the Gaia catalogue with a polynomial up to fourth degree (30 free parameters) beginning with the previously matched stars as our initial guess to capture minor instrumental distortions. Between 4000 and 9000 stars were identified and matched between the Gaia and DECam catalogues in each CCD for this polynomial fitting step. Both iterations of the polynomial transformation were tested over a small range of polynomial orders to arrive at a transformation that produced strong agreement between Gaia and DECam positions.

With this final polynomial transformation from the DECam instrumental reference frame to the Gaia ICRS defined reference frame, we matched DECam objects across all three epochs within one arcsecond and fit their motions independently in RA and Dec using χ^2 minimization. Only stars detected in all three epochs were fit for proper motion. Final proper motion uncertainties are shown in Figure 2.3. Uncertainties here are calculated using standard uncertainty propagation rules from χ^2 minimization. The structure in the multiple systematic uncertainty floors seen in the figure traces back to stars at the edges of fields being observed in incomplete fractions of the imaging dithering patterns. For all but the faintest objects, our proper motions have uncertainties at least three times smaller than our desired signal of 80 mas yr^{-1}. We show additional independent verification of our proper motion measurements and comparisons to Gaia in Appendix 2.8.3. Relative to Gaia, we find that over our whole sample, our proper motion measurements have a root mean square (RMS) difference average of 5.61 mas yr^{-1} and RMS standard deviation of 5.14 mas yr^{-1}. This observed scatter is also much smaller than our desired signal of 80 mas yr^{-1}, allowing for proper motion measurements of sufficient quality to detect a surviving D6 companion within the remnant.

2.4.2 Search Region and Parameter Restrictions

The site of the SN Ia event that created SN 1006 is uncertain because density variations in the interstellar medium might have lead to a significant offset between the geometric center of the
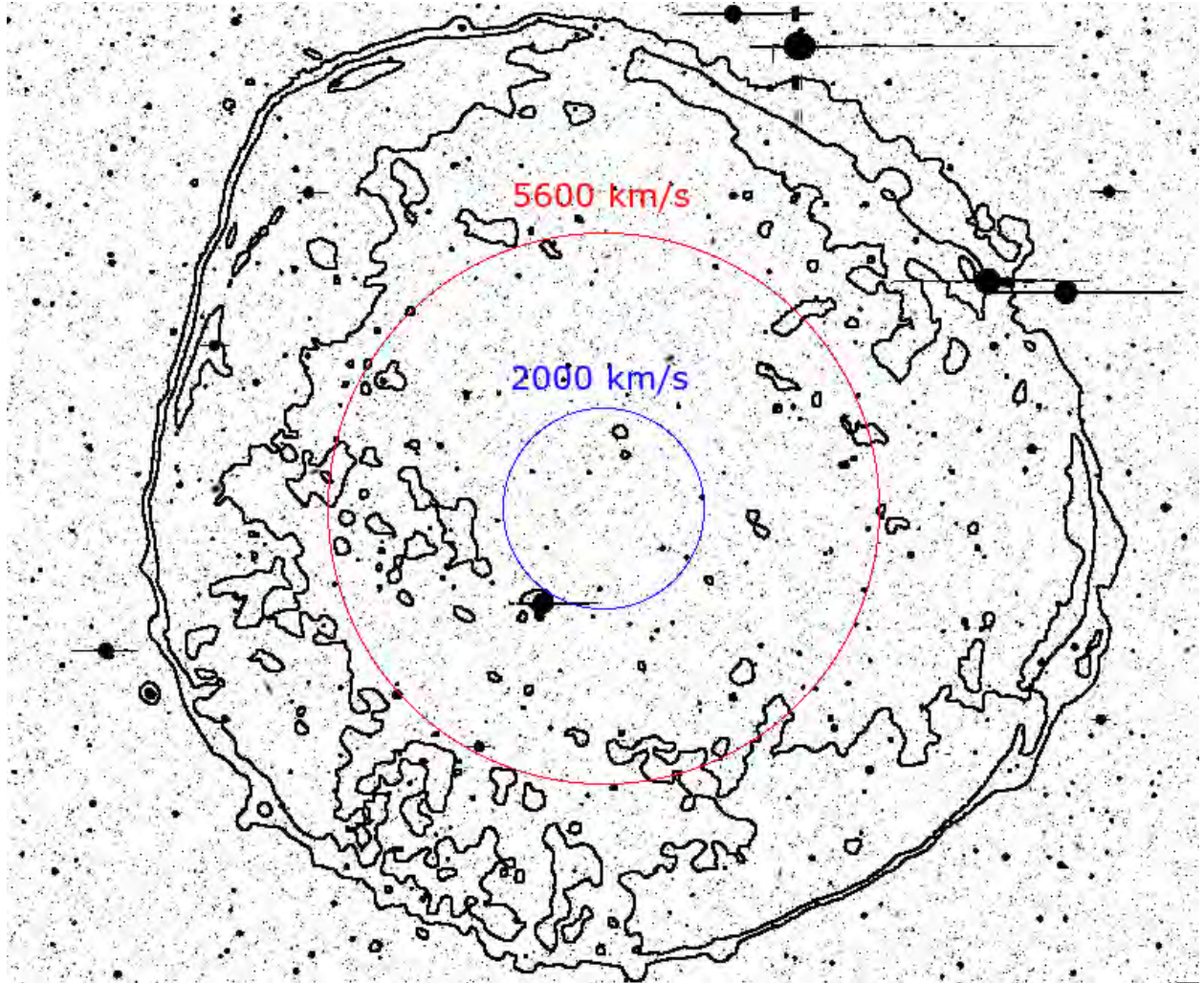
Figure 2.2 2017 DECam imagery of the SN 1006 remnant. The contours are Chandra X-ray data (0.5-0.9 keV) showing the position of the remnant. The circles indicate the search region (red) and the the likely maximum displacement of a D6 star (blue), as well as the physical transverse velocity of a star corresponding to the angular distance assuming a distance of the remnant. The larger search region allows for ambiguity on the center of the remnant.

remnant and the site of explosion (Winkler et al., 2005; Williams et al., 2013). We restricted our search to a 9 arcmin cone corresponding to a transverse velocity of $\sim$ 5600 km s^{-1} at a distance of 2.17 kpc, centered on the geometric center of SN 1006 reported as $15^h 02^m 55.4^s - 41°56'33''$ by Winkler et al. 2002. This transverse velocity is far higher than the upper limit on the velocity expected for a surviving companion (Shen & Schwab, 2017), but the cone radius was chosen to allow for strong ambiguity on the site of the explosion. Furthermore, because of this ambiguity, we made no directional proper motion cuts. This left us with 8123 stars for analysis. Our final

catalogue can be found at https://doi.org/10.5281/zenodo.6506198 which includes 125 116 sources both in and around the remnant, with sources delineated as either inside or outside the search region.
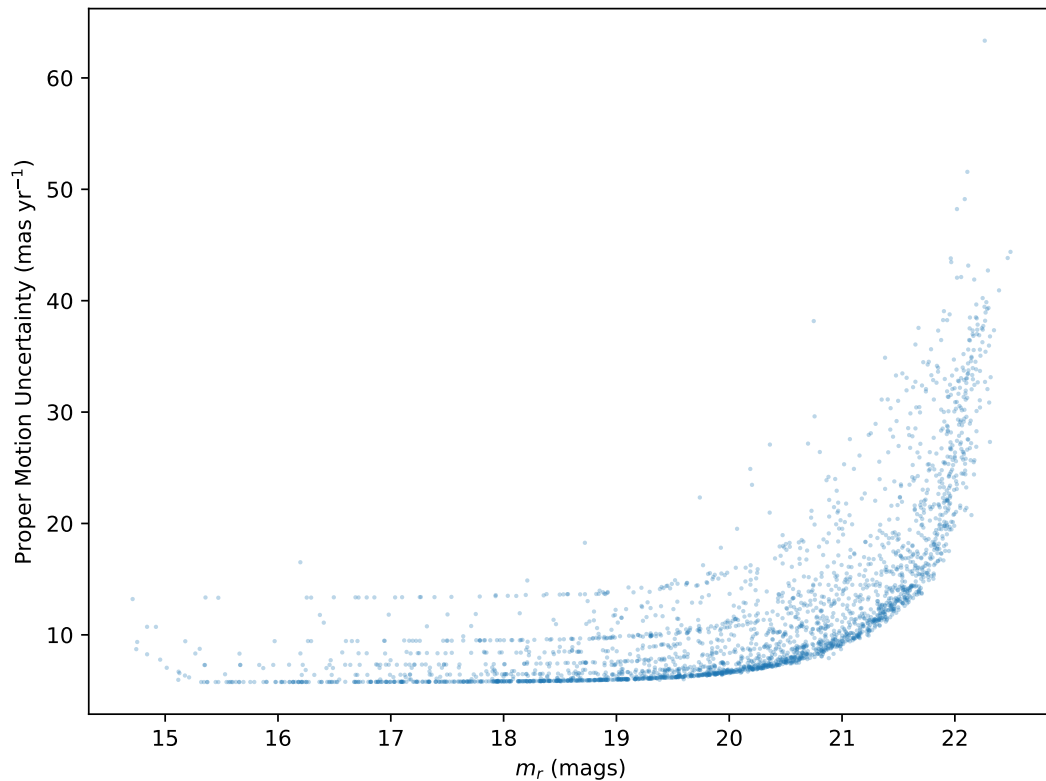
Figure 2.3 Proper motion uncertainty vs r-band magntitude. There are different systematic uncertainty floors depending on CCD dithering and number of observations for a source. The desired signal measurement was 80 mas yr^{-1}.

2.5 Results

We conducted a high-precision proper motion astrometric survey of the stars within SN 1006 to search for a surviving companion predicted by the D6 scenario. In our sample, Gaia completeness appears to drop rapidly at $m_r = 21$ (see Figure 2.4). Inside the remnant Gaia contains 5341 stars. We augmented the survey by measuring the proper motions of 2782 stars up to three magnitudes fainter than Gaia was able to detect. We comment on the high proper motion objects discovered

at these faint magnitudes in Section 2.6, but we chose $m_r = 21$ as the limiting magnitude for this work for three reasons: First, beyond this magnitude limit there are no available color or parallax measurements for our objects which makes it difficult to verify an object's identity as a surviving D6 companion. Second, completeness begins dropping quickly, which can be seen by the large number of objects detected in an incomplete fraction of our observations in Figure 2.4. Third, proper motion uncertainties systematically grow beyond a third of our desired signal of 80 mas yr^{-1} (see 2.1 in Appendix 2.8.1 and Figure 2.5).
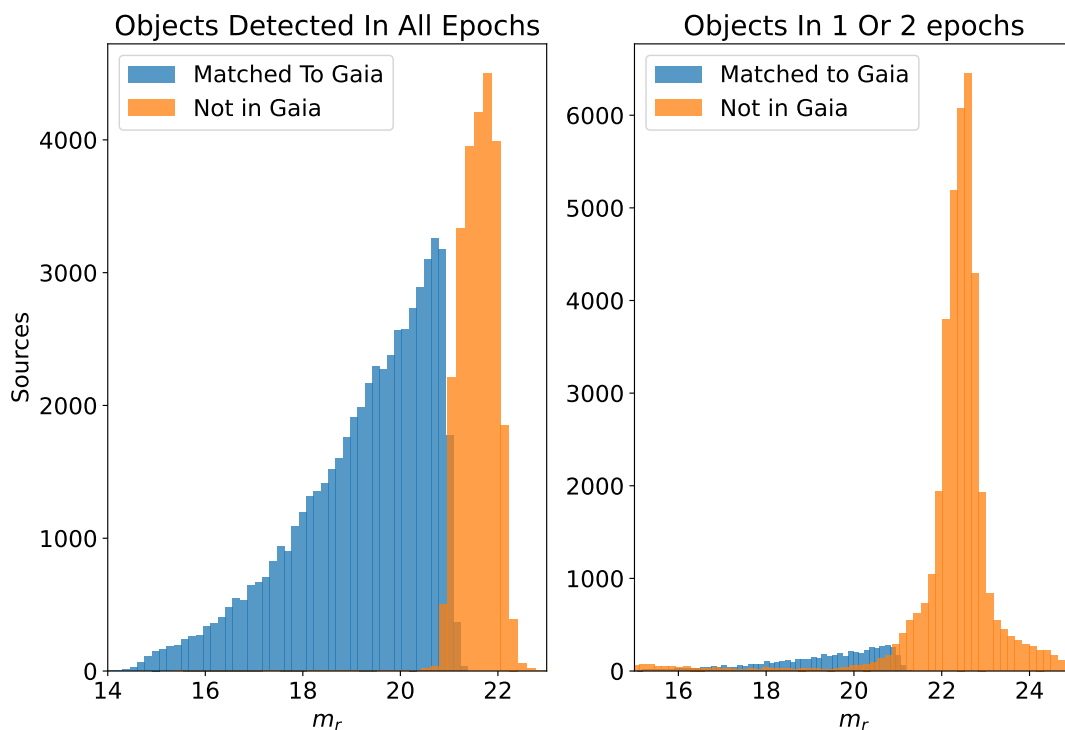
Figure 2.4 Histograms of all sources discovered in our search divided in to sources observed in all three epochs or in an incomplete fraction. We only extracted proper motions for objects discovered in all three epochs.

Our limiting magnitude is multiple magnitudes fainter than a D6 star is expected to appear within the SN 1006 remnant. A D6 star similar to those discovered by Shen et al. 2018 would appear between $17.5 < m_r < 19.2$. However, the three D6 candidates discovered in that work reside within the field, having likely had over 10^5 years to radiate away excess energy injected from

28

the explosion of the primary and reestablish equilibrium appearances. Liu et al. 2021 simulated the appearance of a D6 star shortly after explosion and found that the star would possess a luminosity of $10\ L_\odot$ ($m_r \approx 14.2$ in SN 1006) 10^3 years after the explosion, and remain above $1\ L_\odot$ ($m_r \approx 16.7$ in SN 1006) for 10^7 years. However, a D6 candidate as young as would appear in SN 1006 (10^3 years post SN) has not yet been observed. Thus, for our search, we conservatively considered all stars down to a magnitude of $m_r = 21$. Additionally, while a D6 star inside the remnant is expected to possess a velocity of $>1000\ km\ s^{-1}$, we initially considered down to a projected velocity equivalent of $800\ km\ s^{-1}$ to allow for a hidden radial velocity component and to compensate for measurement error. We then expanded our proper motion cut, detailed in the following paragraph.

The results of our Gaia-DECam survey are shown in Figure 2.5. We show the three previous D6 candidates from Shen et al. 2018, the expected parameter space of a similar star inside SN 1006, as well as our conservative limiting magnitude and proper motion cuts. We did not discover any high proper motion object in this space brighter than $m_r = 21$. To investigate the possibility of a high proper motion object slower than that expected *a priori*, we investigated the 22 fastest of the 8123 stars within the remnant (the percentile equivalent of the 3-sigma highest proper motion outliers). Of these, 18 are too faint to be supported as the surviving companion ($m_r > 21$) without additional followup needed to rule each out from being a contaminating foreground star, a contaminating halo star, or from having a nonphysical proper motion measurement due to an undersampled (PSF) which leads to poor localization. The remaining four candidates are reported in Table 2.1 under their Gaia identifiers and are marked in Figure 2.5, reaching down to a proper motion of $62.5\ mas\ yr^{-1}$ or a projected velocity of $616\ km\ s^{-1}$. We additionally show a color-magnitude diagram of these four stars, the three D6 candidates from Shen et al. (2018), as well as a sample of 150 000 Gaia stars with secure parallax measurements (parallax_over_error > 30) in and around the remnant in Figure 2.7. Unlike the three D6 candidates, the high proper motion Gaia stars in SN 1006 exist firmly on the main sequence and are each therefore unlikely to be the surviving companion. Additionally, Gaia EDR3 6004735811668137472 is the only object possessing a parallax that places it inside the remnant within uncertainties, while the other three have parallax measurements that point to

foreground star identifications.

GAIA Source ID	m_G	$G_{BP} - G_{RP}$	m_r	Parallax (mas)	Proper Motion (mas/yr)	Projected Velocity Inside Rem (km/s)
6004785431417429120	15.35	1.87	15.35	3.37 ± 0.04	67.4 ± 0.1	693.3 ± 1.0
6004784984740826752	20.20	2.60	20.20	2.16 ± 0.81	82.2 ± 1.4	845.6 ± 14.4
6004735811668137472	18.64	1.51	18.64	0.62 ± 0.27	44.2 ± 0.4	454.7 ± 4.1
6004735094407417344	15.26	1.81	15.26	3.48 ± 0.04	60.2 ± 0.1	619.3 ± 1.0

Table 2.1 High proper motion Gaia sources in SN 1006. Projected velocity assumes a distance of 2.17 kpc and not a distance implied by the parallax measurement in case of a spurious parallax measurement that would cause us to miss a surviving companion. Proper motions shown here Gaia reported measurements.

2.5.1 Constraints On Intrinsic Stellar Luminosity

We investigated the intrinsic luminosity constraints of our survey. To estimate the foreground extinction between us and the SN 1006 remnant, we used the Guo et al. (2021) southern sky three-dimensional dust maps, shown in Fig 2.6. The map queried at the distance of the remnant gives an extinction $E_{B-V} = 0.0673 \pm 0.0176$. Assuming an $R_V = 3.1$ F99 reddening law following Schlafly & Finkbeiner 2011, we calculate $A_V = 0.2154 \pm 0.0564$. Furthermore, using a resulting $A_r/A_V = 0.89$, we estimate $A_r = 0.192 \pm 0.050$. Adopting $A_r = 0.192$, a distance modulus of 11.68 corresponding to a distance of 2.17 kpc, and a bolometric magnitude equal to r-band, a $m_r = 21$ object posses an intrinsic luminosity of $L = 0.0176L_\odot$. We did not detect a high proper motion object with unusual colors brighter than this luminosity within SN 1006.

2.6 Discussion

We have investigated a prediction of one realization of the D6 scenario which might be a generic explanation for SNe Ia. We have no observationally motivated constraints for how a D6 star would appear shortly after the explosion of the primary. The three candidates presented in Shen et al. 2018 were discovered in the field of the galaxy, and are estimated to be older than $\sim 10^5$ years post explosion. Theory suggests that a young D6 star would be brighter than $m_r > 19$, but a significant inherited velocity remains the strongest observable property of such a star. We have investigated the stars in SN 1006 for this signature. Our survey places strict limits on the parameter space that a surviving D6 companion could exist inside SN 1006. Previous direct searches went down to $m_r = 15$ (Hernandez et al., 2012) and $m_V = 19$ (Kerzendorf et al., 2012). Kerzendorf et al. 2018b went down to $m_r = 21$ but only sought to investigate objects closely following the white dwarf cooling track. Here, we rule out the possibility of a high velocity surviving companion in the remnant down to $m_r = 21$.

2.6.1 Confounding Possibilities

We did not detect an overluminous surviving white dwarf companion with a high enough proper motion to be consistent with the D6 scenario inside SN 1006. We explored possibilities for a surviving D6 companion to have gone undetected in our analysis. Our search targeted stars
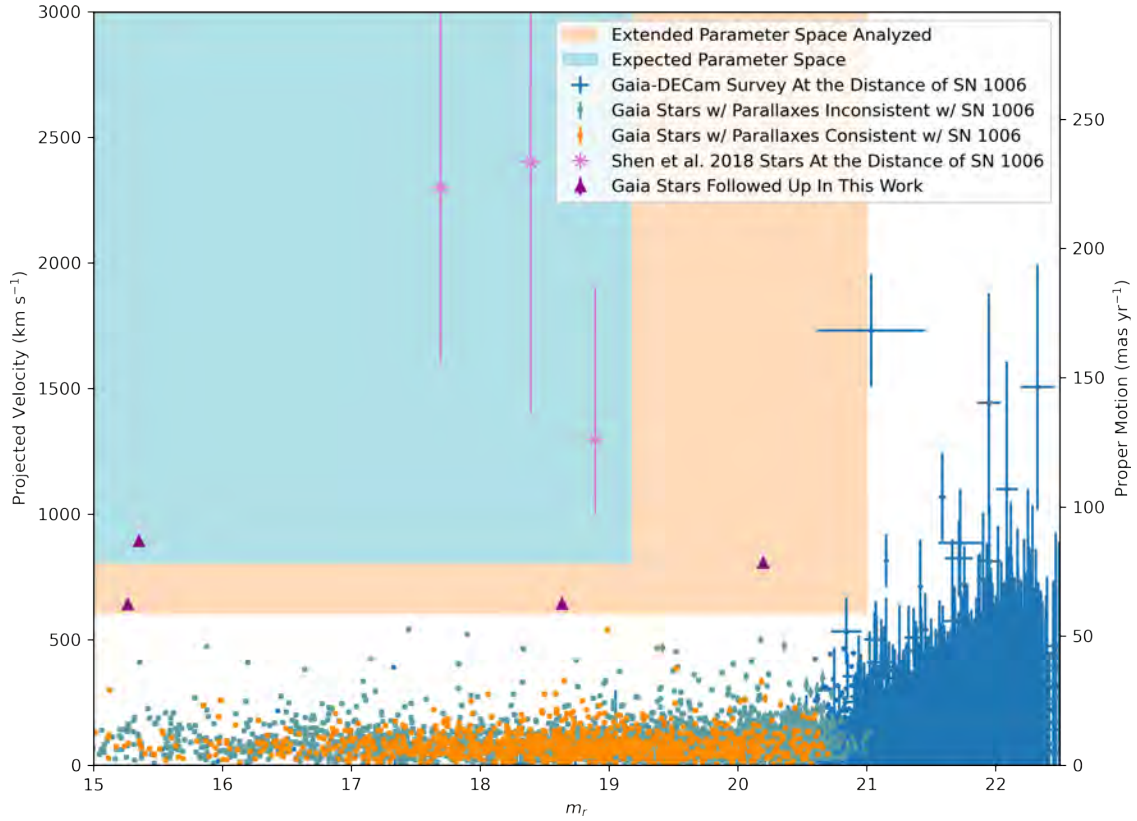
Figure 2.5 Results of proper motion survey showing apparent r-band magnitude against proper motion measurement and calculated transverse velocities assuming a distance of 2.17 kpc for DECam sources. The three Shen et al. 2018 stars have corrected apparent magnitudes as they would appear at the same distance with uncertainties and including foreground extinction. A surviving white dwarf companion in accordance with the predictions of the D6 scenario was expected to lie in the shaded region with the previously discovered D6 stars. The four Gaia stars in the analyzed region are shown in Table 2.1 and Figure 2.7, and are discussed in Section 2.5 along with the high proper motion objects fainter than 21.

with large transverse velocities detectable through proper motion measurements. As a result, we identified two following outstanding reasons that a D6 star in the remnant might have gone undetected in our study: First, the star may have inherited an exceedingly large radial velocity with a small transverse velocity by being ejected near parallel to our line of sight. Second, the star may be hidden by significant, unforeseen dust obscuration prompted by interaction with the SN.

33

We explore the possibility that a star launched with a significant velocity in a random direction did not inherit a large transverse velocity, with the majority of the velocity hidden in the radial direction. We performed a Monte Carlo simulation of a star launched in a random direction with a velocity of 1000 km s^{-1}, the lowest theoretically predicted velocity of a D6 star. The resulting probability distribution of the observed tangential velocity measured for such a star is presented in Figure 2.8. Our experiment and analysis would have detected the star above 94.3% of the time. However, a D6 star likely inherits a velocity far greater than 1000 km s^{-1}, quickly shrinking the unexamined portion of this distribution (e.g., a 1200 km s^{-1} star would have been discovered 97.3% of the time). This parameter space could be examined with detailed radial velocity measurements of the stars in SN 1006, but remains a small, outstanding possibility.

We also consider the possibility that a D6 star could have been heavily enshrouded by dust from the remnant and thus appeared fainter than 21st magnitude in r-band. In Figure 2.6, we show the V-band absorption enclosed by the remnant, approximated by sampling the Guo et al. (2021) dust maps in front of and behind three times the uncertainty on the distance to the remnant. We see no evidence of additional dust absorption in the remnant on large enough scales to be detectable by these dust maps, with an angular resolution of 13.7 arcmin. Any obscuring dust capable of hiding the surviving companion would need to be localized around the star itself, such as dust produced by a strong stellar wind prompted by interaction with the SN explosion.

2.6.2 Faint High Proper Motion Outliers

As a result of this survey, we discovered six faint, high proper motion objects between 21 and 22.5 mag listed in Table 2.2 and seen in the faint end of Figure 2.5. These objects are too faint to have color information, and we note that these objects have large proper motion uncertainties due to their poorly constrained initial positions tracing back to their faint appearances, and thus the objects are mostly less than one or two sigma above our velocity threshold. While one of these objects may be the surviving companion in line with the significant dust obscuration scenario detailed above, we note that each is also likely a result of statistical sampling uncertainties and the large number of sources examined. Furthermore, we examined the Spitzer Enhanced Imaging Products

(Capak; Peter, 2019; Fazio et al., 2004; Werner et al., 2004) combined 3.6, 4.5, 5.8, and 8.0 micron image catalogue for coincident infrared sources with our high proper motion objects and did not discover any aligned sources. This provides strong evidence against dust obscuration, as absorbed light should be re-radiated in the infrared and make the source easily detectable. We however note that spectral followup of these objects would concretely support or reject their respective statuses as the surviving companion by providing both color information that could place them on the main sequence or in an unusual portion of the color magnitude diagram, as well as radial velocity measurements that could support or oppose high intrinsic velocities as opposed to modest intrinsic velocities that appear large due to foreground nature.

Target	RA (deg)	Dec (deg)	m_r	Proper Motion (mas/yr)	Projected Velocity (km/s)
Candidate 1	225.618762	-41.856965	22.33	146.4 ± 47.3	1506.0 ± 486.6
Candidate 2	225.801826	-42.041687	22.09	107.0 ± 49.1	1100.7 ± 505.1
Candidate 3	225.823198	-42.064307	21.73	86.0 ± 21.0	884.7 ± 216.0
Candidate 4	225.697236	-41.985479	21.72	80.2 ± 14.6	825.0 ± 150.2
Candidate 5	225.916877	-41.995497	21.59	103.9 ± 17.1	1068.8 ± 175.9
Candidate 6	225.586830	-41.888318	21.04	168.3 ± 21.8	1731.0 ± 224.1

Table 2.2 Discovered faint high proper motion objects in SN 1006. Projected velocity assumes a distance of 2.17 kpc. These objects are too faint to be supported as D6 candidates in this work but remain interesting candidates. Additionally, we investigated candidate 6 and found it to have an unreliable measurement due to its psf overlapping with a nearby bright star.

2.7   Conclusions and Future Work

We present a deep four year baseline astrometric survey of the stars in the SN 1006 remnant. We do not detect an overluminous, high proper motion white dwarf similar to that predicted by a realization of the D6 scenario presented in Shen et al. 2018. This result suggests that this realization of the D6 scenario is not generically responsible for SNe Ia. Alternatively, this result might be in line with the recent result of Pakmor et al. 2022, which showed that a SN Ia like-event can be created through the detonation of both the primary and the secondary white dwarf in the D6 scenario.

We investigated possibilities that a surviving companion star similar to or brighter than those detected in the field could have gone undetected in our study. We find that:

- There is less than a 5.7% chance that a star with an intrinsic velocity of 1000 km s^{-1} could have been ejected from the system near parallel to our line of sight, and have inherited a small enough proper motion to have remained undetected. This possibility shrinks quickly as the velocity of the surviving companion increases.

- There is no significant additional large scale dust created by or coincident with the SN remnant. Dust capable of obscuring the surviving companion would need to be on angular scales significantly smaller than 13.7 arcmin or a physical scale of 8.6 pc at the distance of the remnant, localized around the surviving companion itself.

We briefly consider the possibility of detecting a surviving D6 companion with an assumed luminosity of about 0.1 $L_\odot$ in other Galactic SN Ia remnants. We did not detect an unambiguous, overluminous white dwarf companion inside SN 1006 as predicted by our tested realization of the D6 theory, however there exist tens of SN Ia remnants in the Galaxy where a similar study could potentially be performed to search for a similar star. Upon inspection, we find that only three unambiguously classified SN Ia remnants exist with comparable distances to SN 1006, where a D6 star is approaching detection limits. These three remnants are RCW 86, Tycho's SNR, and G272.2-3.2. These remnants all lie within or close to the Galactic plane behind 4.4, 3.5, and 2.6 magnitudes of V-band extinction respectively (Schlafly & Finkbeiner, 2011). This poses a challenging obstacle for repeating a high precision proper motion survey within these remnants, where a 0.1 $L_\odot$ star could be as faint as $m_r \sim 24$.

2.8 Appendix

2.8.1 Position Uncertainty Estimation

We estimated the uncertainty of a single observation from the Dark Energy Camera following Rest et al. (2013):

$$\sigma_{pix} = 0.1^2 + 1.5(\frac{FWHM}{SNR})^2 \tag{2.1}$$

2.8.2 Matching Algorithm Choices

To create our individual epoch catalogues we combined detections of sources with two or more observations using the SCIPY.SPATIAL.KDTREE package to subdivide the parameter space and reduce considered associations. We disregarded sources within three pixels from the edge of an observation, and only matched stars within one pixel or 0.263 arcec. We chose this search radius, taking in to consideration the stellar density of roughly one in eight pixels. Additionally, the nearest neighbor distribution function is shown in Fig 2.9, which shows that the nearest neighbor of a source is farther than 0.263 arcsec away in almost all cases. A source could be matched with an unrelated object if it is both within the search region of the unrelated source and it is not detected in a given epoch. This likely has the effect of artificially increasing proper motions, as the source would be reported having moved anomalously far between epochs, and is much more likely to be an issue for faint objects. This effect may explain some of the faint, high proper motion objects in our sample.

2.8.3 Proper Motion and Position Measurements Compared To Gaia

We compare the proper motions and positions of sources matched between the DECam and Gaia EDR3 catalogues. Our residual proper motion and position measurements are consistently smaller than our desired signal of 80 mas yr^{-1} (Figures 2.10 and 2.11), verifying the accuracy of the astrometric reference frame for our DECam measurements. We note that these matched stars were previously used to discover the polynomial transformation, so these do not provide a completely independent verification, but the fitting free parameters (30) are three orders of magnitude fewer than the sampled data-points (~ 8000 per CCD) so the correlations are not severe.
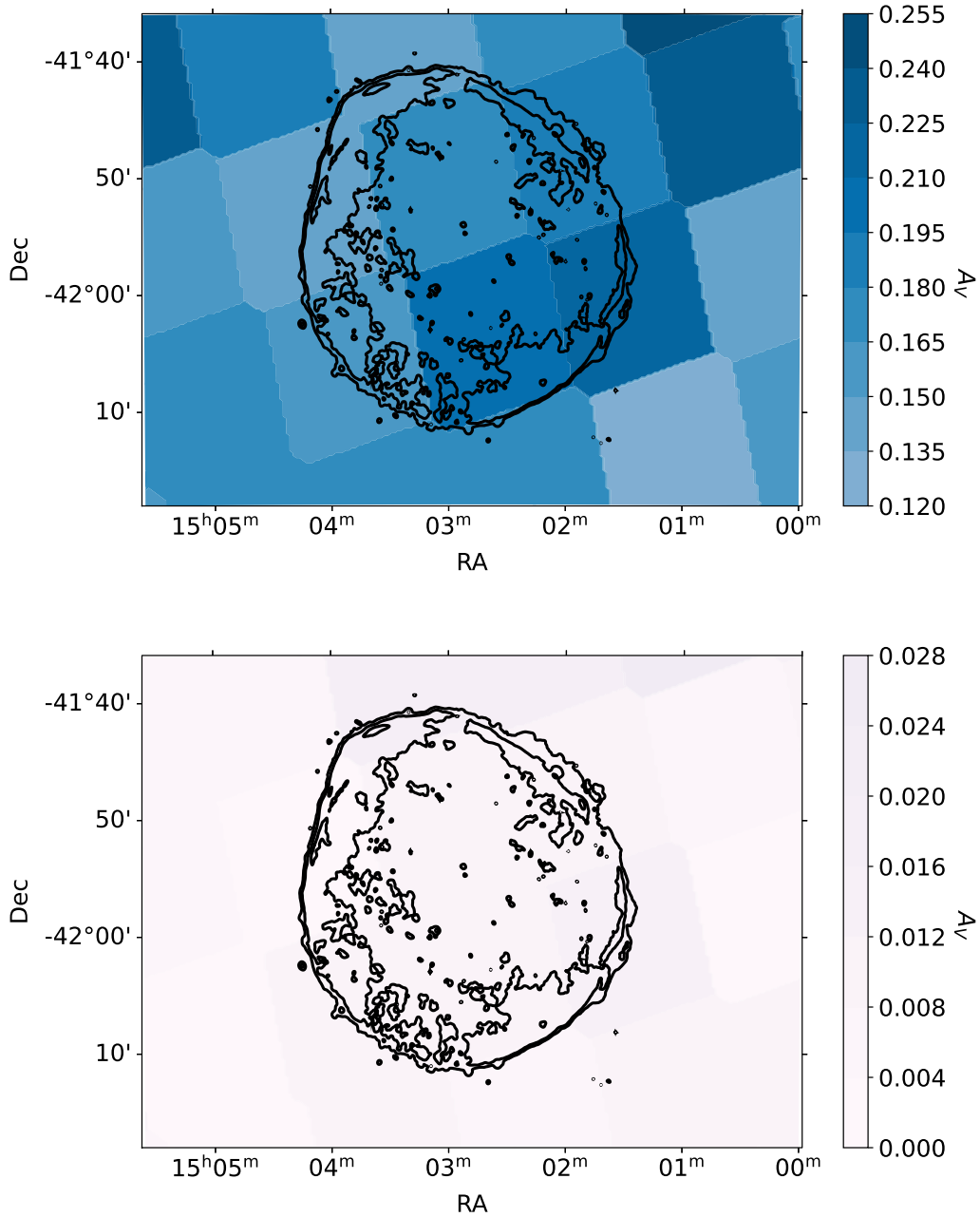
Figure 2.6 Guo et al. 2021 three-dimensional dustmaps sampled in the direction of the SN 1006 remnant with x-ray contours displayed to show the position of the remnant. The top shows the maps sampled at the distance of the remnant (2.17 kpc). The bottom shows the difference between the absorption sampled at 1.94 and 2.41 kpc (2.17 ± 0.24, 3 standard deviations of the uncertainty on the distance, 0.08, respectively). Both maps are placed on a consistent color-scale to emphasize the lack of additional dust extinction measured within the remnant. A_V is calculated assuming $E_{B-V} = 3.1 A_V$ following Schlafly & Finkbeiner 2011.
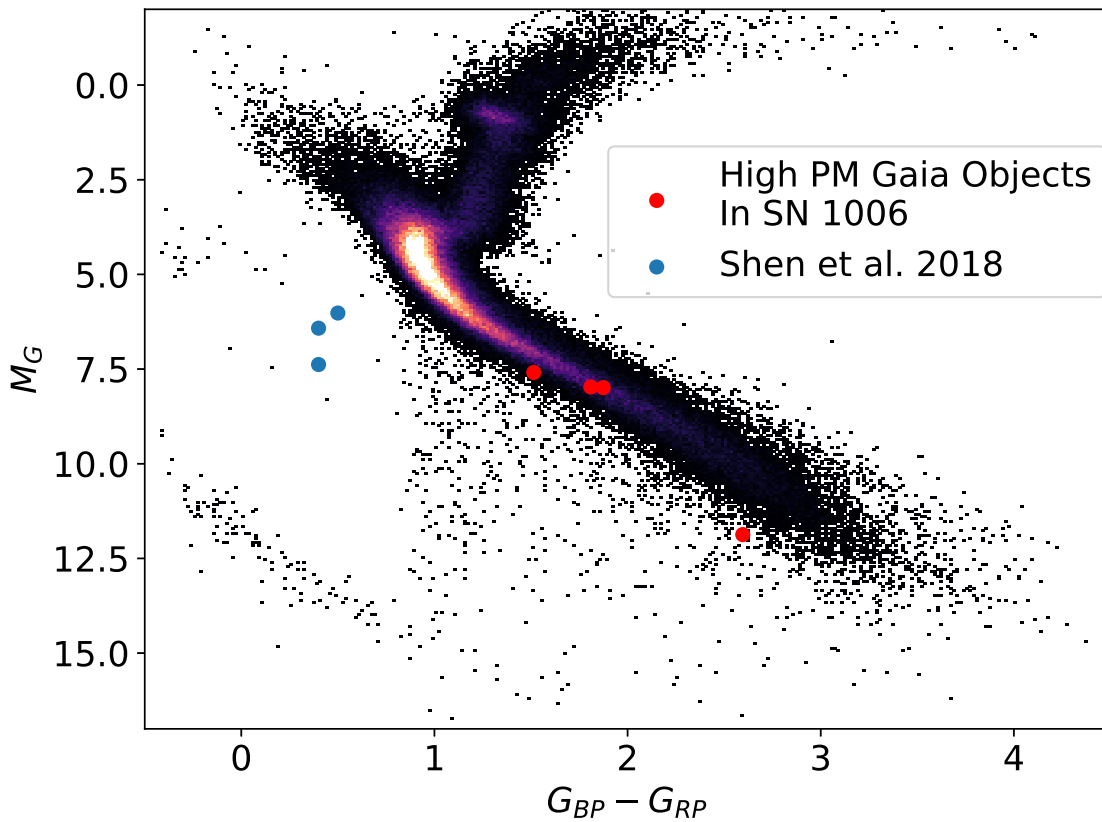
Figure 2.7 Color-Magnitude Diagram of 150 000 secure parallax (parallax over error > 30), Gaia stars around SN 1006. The blue dots show the three D6 candidates discovered in the field by (Shen et al., 2018) far off the main sequence. The red dots show the high proper motion (> 500 km s^{-1}) Gaia objects inside SN 1006 in our search. They lie on or close to the main sequence with ordinary colors.
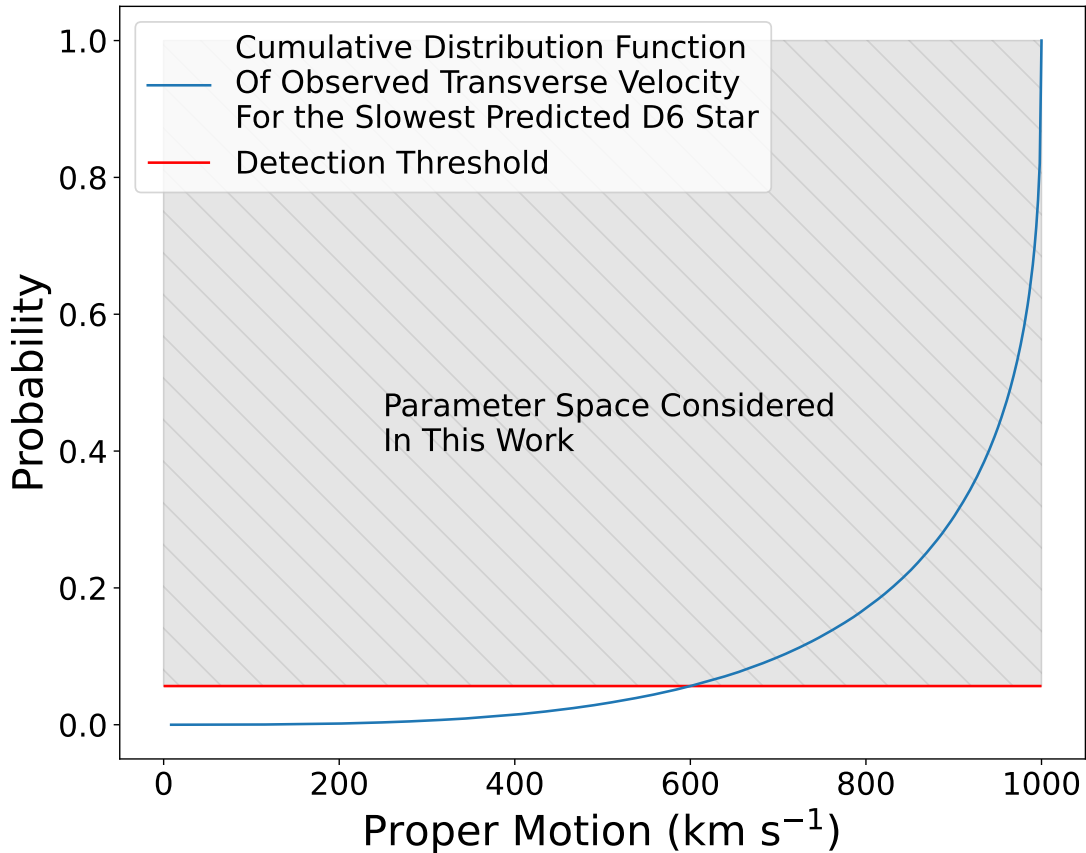
Figure 2.8 Results of our MC simulation showing the observed transverse velocity of a 1000 km s^{-1} star, the minimum expected velocity of a D6 star, traveling in a random direction. We examined all stars with proper motions corresponding to transverse velocities of above 600 km s^{-1} or proper motions of 58.3 mas yr^{-1} (the top 22 proper motion objects in our survey). As shown, this corresponds to examining 94.3% of this distribution. A faster velocity quickly shrinks the probability space, effectively moving further down the shallow tail of the distribution.
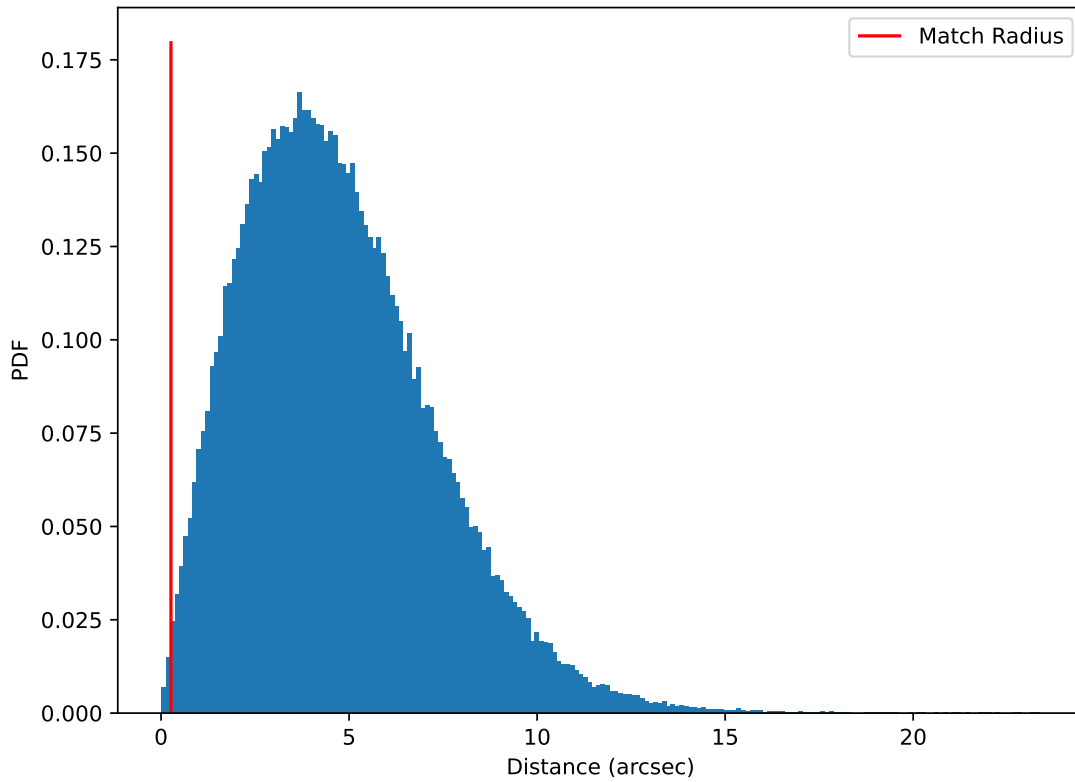
Figure 2.9 Nearest neighbor distribution function for a sample CCD after the initial stellar matching was completed. We adopted a search radius of 1 pixel or 0.263 arcsec for our initial matching algorithm, a small enough search radius to not allow for significant source confusion at the stellar density of the field.
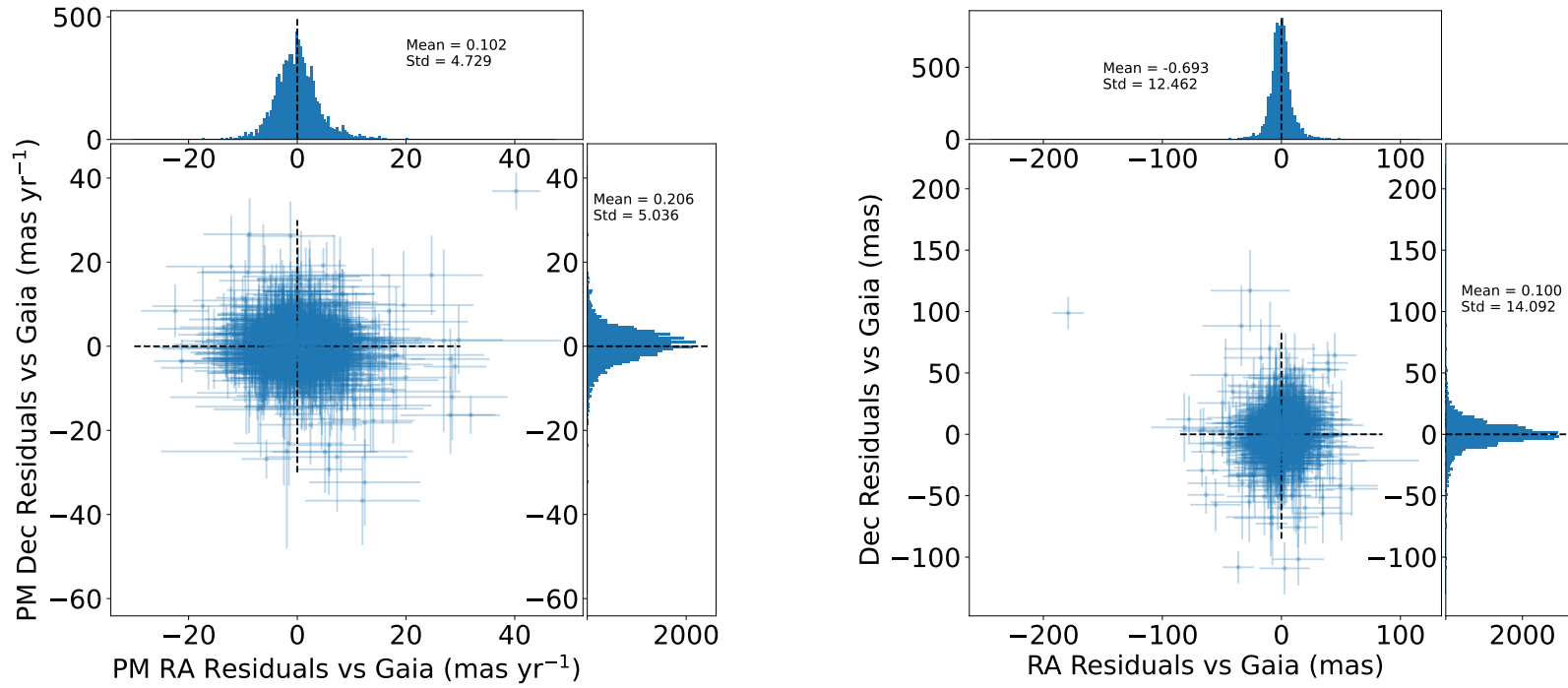
Figure 2.10 Residuals of DECam measurements vs. Gaia for cross-matched sources in RA and Dec in both proper motion (left) and position (right) space. Our desired precision was 80 mas yr^{-1}, many times higher than the scatter in our distributions which give an empirical estimate of our error.
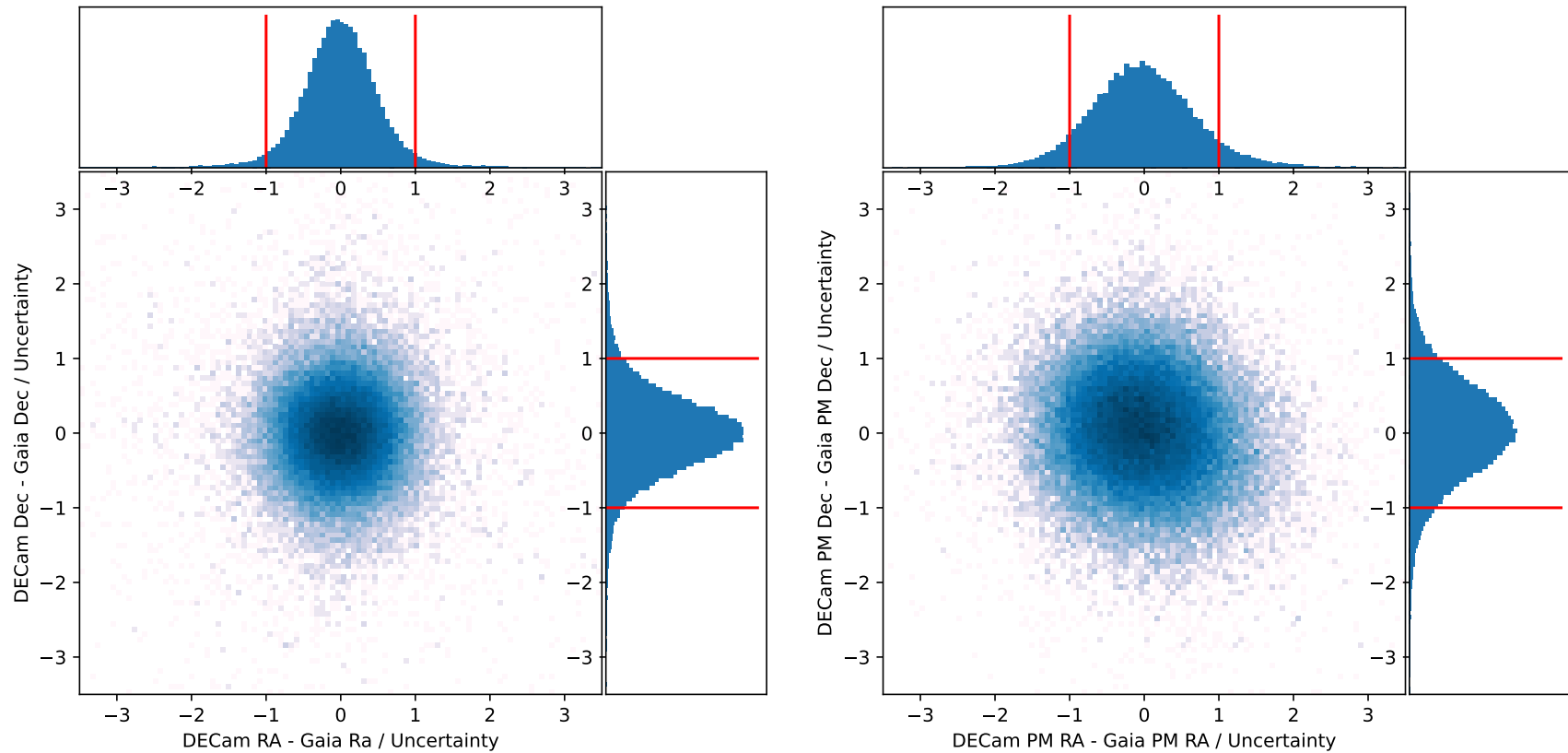
Figure 2.11 Position (left) and proper motion (right) residuals of DECam vs. Gaia measurements for cross-matched sources in RA and Dec over uncertainty in each dimension. We expect 68% of sources to be smaller than 1 sigma. We find ∼ 92% of sources in position space and ∼ 85% of sources in proper motion space lie within this region, suggesting that our errors may be overestimated.

CHAPTER 3

NO SURVIVING SN IA COMPANION IN SNR 0509-67.5: STELLAR POPULATION CHARACTERIZATION AND COMPARISON TO MODELS

This section reviews the published work Shields et al. (2023),

Figure 3.1 The SNR0509-67.5 Remnant. Credit: NASA, ESA, CXC, SAO, the Hubble Heritage Team (STScI/AURA), and J. Hughes (Rutgers University)

3.1 Abstract

The community agrees that Type Ia supernovae arise from Carbon/Oxygen white dwarfs undergoing thermonuclear runaway. However, the full progenitor system and the process that prompts the white dwarf to explode remain unknown. Most current models suggest that the white dwarf explodes because of interaction with a binary companion which may survive the process and remain within the resulting remnant of the exploded star. Furthermore, both the pre-supernova interaction process and the explosion of the primary are expected to imprint a significant departure from ordinary stellar radii and temperatures onto the secondary, making the star identifiable against the unrelated stellar population. Identification of a surviving companion inside an SN Ia remnant might confirm a specific corresponding SN Ia progenitor channel based on the identity of the companion. We conducted a surviving companion search of the Type Ia remnant SNR 0509−67.5 based in the Large Magellanic Cloud. The well-constrained distance to and foreground extinction of the Large Magellanic Cloud allow for Bayesian inference of stellar parameters with low correlation and uncertainties. We present a deep catalog of fully characterized stars interior to SNR 0509−67.5 with radii, effective temperatures, and metallicities inferred using combined Hubble Space Telescope photometric observations across multiple visits. We then compile a list of surviving companion models appropriate for the age of the remnant (roughly 400 years after the explosion). We compare these predictions with the inferred stellar parameters and conclude that none of the stars are consistent with the predicted signatures of a surviving companion.

3.2 Introduction

Type Ia supernovae (SNe Ia) play a critical role across astronomy. As standardizable candles, they serve as distance indicators (e.g. Phillips, 1993; Phillips et al., 1999) that led to the discovery of the accelerating expansion of the universe (Riess et al., 1998; Schmidt et al., 1998; Perlmutter et al., 1999). They are also known to provide a substantial fraction of the iron group elements in the Universe, driving galactic chemical enrichment over cosmic time (Timmes et al., 1995; Nomoto et al., 2013; Kobayashi et al., 2020). Despite the importance of these energetic events, we have still not confirmed their progenitor system and explosion mechanism (Livio, 2000; Wang & Han, 2012;

Ruiz-Lapuente, 2019). It is widely accepted that SNe Ia arises from the thermonuclear explosions of Carbon/Oxygen (C/O) white dwarfs (Pankey, 1962; Colgate & McKee, 1969), but the process that prompts the white dwarfs to explode is still uncertain. This major uncertainty on the origins of SNe Ia propagates directly to their empirically calibrated interpretations, introducing additional uncertainty or potential bias into our understandings of galactic chemical enrichment and universal expansion.

SN Ia progenitor models can be divided into two major channels distinguished by the survival or destruction of the secondary in the binary progenitor system that prompts the C/O white dwarf to explode. In the first channel, the primary white dwarf violently merges with a secondary white dwarf, prompting thermonuclear explosion (e.g. Webbink, 1984). In this scenario, the explosion may fully unbind both stars leaving no stellar remnant behind (Pakmor et al., 2012; Papish et al., 2015). In the second, the primary either stably or unstably accretes material from a secondary which prompts thermonuclear runaway in one of a variety of ways (Whelan & Iben, 1973; Iben & Tutukov, 1984). The companion in this broad progenitor channel has been proposed to be either a helium star (Iben & Tutukov, 1994; Wang et al., 2009), a helium-rich white dwarf (Bildsten et al., 2007), a post-main sequence giant star (Li & van den Heuvel, 1997), an evolved sub-dwarf (Meng & Li, 2019), or a main sequence star (Han, 2008; Meng et al., 2009). The majority of accretion scenarios predict that the secondary survives the SN explosion and will remain near the site of the explosion (Shappee et al., 2013a). Crucially, this means that the surviving companion to the exploded star will reside near the center of the supernova remnant (SNR) that is produced by the event.

In most accretion scenarios, the accretion and explosion processes are expected to impart identifiable signatures onto the companion that persist for at least thousands of years: During mass transfer, the secondary may experience tidal forces that may both heat the star (Shen & Schwab, 2017). This process may also cause the secondary to become tidally locked with the primary which will also cause the star to adopt an anomalously high rotation rate (Kerzendorf et al., 2009). When the primary explodes, the secondary will no longer be gravitationally bound and will be shot out of

the system at its pre-explosion orbital velocity (Shen et al., 2018), far above velocities obtainable through normal processes of stellar evolution. Shortly after the primary explodes, the companion will be impacted by the SN ejecta, which may strip a significant amount of material from the star (Marietta et al., 2000), or deposit energy into the stellar envelope, causing it to increase in temperature or inflate (Liu et al., 2021). Any ejecta that is captured by the companion will be rich in radioactive elements which can continue to inject energy into the star (Shen & Schwab, 2017). The ejecta will also contain a large fraction of iron group elements which can remain detectable in the stellar photosphere (Ozaki & Shigeyama, 2006).

If a surviving companion can be identified inside an SNR Ia by a combination of the signatures expected for such a star, that identification would directly confirm a specific corresponding accretion scenario as a viable SN Ia progenitor channel (Marietta et al., 2000; Pakmor et al., 2008). However, decades of intense, focused searches of Galactic SNRs have failed to securely identify even a single unambiguous SN Ia companion (see e.g. Ruiz-Lapuente et al., 2004, 2018; Ruiz-Lapuente, 2019; Kerzendorf et al., 2013, 2018b; Shields et al., 2022). Unfortunately, it is difficult to extrapolate from these results to make conclusive statements about the viability of SN Ia progenitor channels. Galactic remnants are plagued with highly uncertain distances (see e.g. Tycho's SNR, Ihara et al., 2007) and unconstrained column densities of foreground dust (see e.g. Kepler's SNR, Kerzendorf et al., 2014) which leads to generally narrow searches that are not sensitive to all viable progenitor channels and the surviving companions they are expected to produce.

In direct contrast, the Large Magellanic Cloud (LMC) resides at a well-constrained distance of 49.59 ± 0.63 kpc (Pietrzyński et al., 2019), with very little foreground extinction (Joshi & Panchal, 2019) due to its high Galactic latitude and face-on orientation (van der Marel et al., 2002). Additionally, the galaxy resides close enough for individual stars to be resolved by the Hubble Space Telescope (HST). These properties make SNRs Ia enclosed in the LMC uniquely well-suited for surviving companion searches that are free from the major problems of remnants in the Milky Way (Li et al., 2019).

SNR 0509−67.5 is a young LMC remnant confirmed to be of SN Ia origin by light echoes of

Prop. ID	MJD	Prop. PI	Filter	Exp. Time (s)	Limiting Mag (AB)
12326	55504	Noll	F475W	1010	26.08
12326	55504	Noll	F555W	696	26.05
12326	55504	Noll	F814W	800	25.17
13282	56559	Chu	F814W	1465	25.49
13282	56559	Chu	F110W	298	25.53
13282	56559	Chu	F160W	798	25.03

Table 3.1 The six observations combined to create our stellar catalogs. Limiting magnitudes were estimated based on the faintest star observed in the observation.

the original SN spectrum (Rest et al., 2005b, 2008b). Schaefer & Pagnotta (2012) conducted a tight search near the geometric center of the remnant, with a search region large enough to discover stars ejected from the progenitor system at speeds of up to $390\,\mathrm{km\,s^{-1}}$. That work found no objects in their search region other than a diffuse source that was later identified to be a background galaxy (Litke et al., 2017), suggesting that no surviving companion exists within the remnant. However, recent works allow for surviving companions traveling significantly faster (see e.g. Shen et al., 2018, up to $2500\,\mathrm{km\,s^{-1}}$), suggesting that a companion has not been conclusively ruled out. Recently, Arunachalam et al. (2022, hereafter A22) used accurate proper motion and location measurements of the remnant's forward shock to determine a precise dynamical explosion center. We decided to revisit this remnant with these new constraints to conduct a thorough surviving companion search.

In this work, we present a characterized catalog of the stellar population inside SNR 0509−67.5 to discover a surviving Ia companion. We synthesized six HST observations of the remnant in five broad filters to construct detailed spectral energy distributions (SEDs) of the enclosed stars. We fit the observations of each star with backward physical modeling using Bayesian Inference to move from SEDs to distributions of stellar astrophysical parameters that could produce each set of photometric observations.

In Section 3.3, we describe the data and synthesis methods we used to construct SEDs of the interior stellar population to SNR 0509−67.5. In Section 3.4, we describe our models and astrophysical parameter inference methods. In Section 3.5, we present the results of our inference and compare them to the expected parameters of surviving companions in the literature. In Section 3.6, we discuss the constraints our results place on allowed surviving companions in the SNR
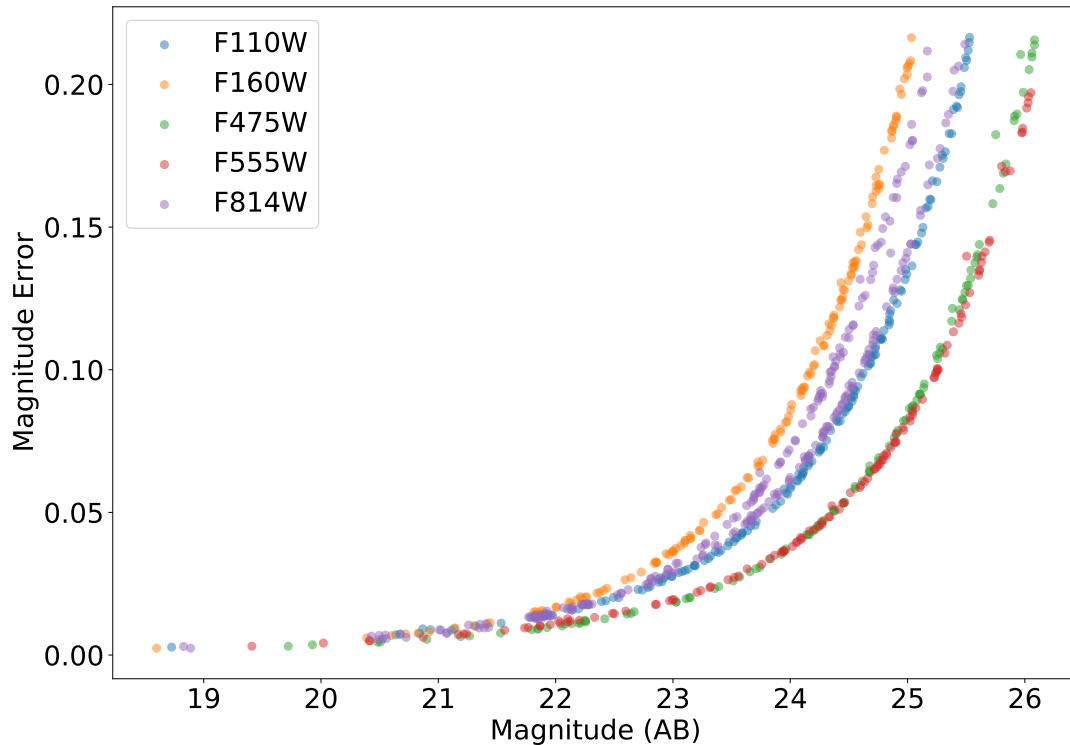
Figure 3.2 Error on magnitude as a function of magnitude for the full set of characterized stars in the larger sample, by filter. These data show the observational uncertainties used for our Bayesian inference fitting.

0509−67.5 remnant. We conclude in Section 3.7 by highlighting the parameter space ruled out for surviving companions as well as discussing further implementations of the techniques in this paper.

3.3 Observations

We needed to construct a well-sampled SED of each star inside SNR 0509−67.5 to characterize the interior stellar population and search for the existence of a surviving companion. To measure stellar radii and temperatures, we fundamentally needed to constrain the peak and shape of each stellar blackbody curve. SNR 0509−67.5 has been well observed by the HST in eight different filters. In this work, we chose to restrict ourselves to five wide-band HST filters (see Table 3.1) for ease of methodological development. A larger set of filters would more powerfully constrain

stellar astrophysical parameters but is beyond the scope of this work.

3.3.1 HST Catalogs

We set out to create a catalog of the interior stellar population to the SNR 0509−67.5 using a large enough sample of HST observations to construct well-sampled SEDs. However, individual archival HST observations have been shown to suffer from misaligned WCS with errors on the order of an arcsec, which has previously prohibited the creation of stellar catalogs with straightforward coordinate-based source matching. However, the recent HST Astrometry Project has re-derived WCS for archival observations by cross-identifying bright stars Gaia DR2 for alignment and reduced astrometric errors to approximately 10 mas (Hoffmann et al., 2021), published in the Hubble Source Catalog (HSC). We queried updated stellar sky positions and matched sources in the HSC available through the **CasJobs** database (Whitmore et al., 2016) for cross-visit matching to construct SEDs for stellar characterization. The resulting individual, unmatched observations are shown in Figure 3.2.

3.3.2 Search Region

We obtained observations of each star within a 4.2 arcsec (1.00 pc at 49.27 kpc) radius of the dynamical center of the SNR 0509−67.5 as determined by A22. This radius corresponds to the distance that a $2500 \, \mathrm{km \, s^{-1}}$ object (the fastest surviving companion velocity predicted in our considered models) could have traveled at the distance of the LMC, over a highly conservative age estimate for the remnant of 400 years (a strong upper limit from models of the remnant's expansion, see A22 for further discussion).

In addition, we obtained observations of the surrounding stellar population within 10 arcsec of the dynamical center of SNR 0509−67.5 in order to have a control sample of stars that could not be the surviving companion. We used this sample to better understand the sensitivity of our search and how the individual limiting magnitudes of the observations translate to limits on inferred astrophysical parameters.

In Figure 3.3, we show a composite image of SNR 0509−67.5 created with `APLPY` (Robitaille & Bressert, 2012) using two of the six observations analyzed in this work (F814W and F555W),
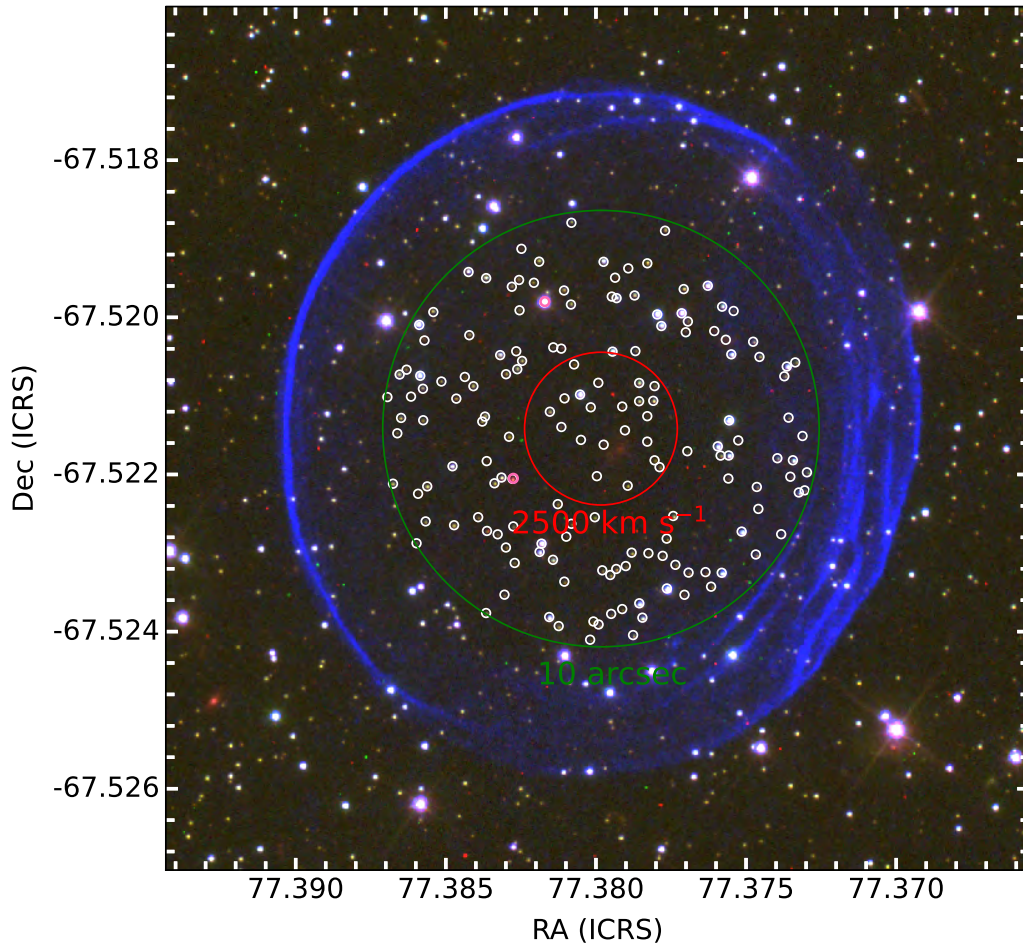
Figure 3.3 A composite image of SNR 0509−67.5 from archival photometry. The red channel is the F814W filter, green is F555W, and blue is F656N. The red circle shows our search region where stars are close enough to the center to be the surviving companion, and the green region shows the larger control sample of characterized stars we used to better understand the unrelated stellar population and the uncertainties of our technique. The white circles show the individual stars that were modeled and characterized. The two large stars we discuss in Subsection 3.5.2 are circled in pink.

as well as F656N to clearly show the remnant. We show the search region of potential surviving companions, the control sample, as well as each of the identified interior stars.

3.4   Methodology & Analysis

Our goal was to be sensitive to the entire range of predicted surviving companions which we gathered and show in Table 3.2. In designing this study, we chose to propagate the most conservative case for each parameter across all other parameters to be certain that we were sensitive to any potential type of surviving companion. As a result, certain portions of our combined parameter space are not realizable for a surviving companion (e.g. a non-degenerate companion cannot reside far away from the center of the remnant due to a lower maximum ejection speed). However, we decided that this approach was necessary to safeguard against potentially missing a surviving companion.

3.4.1   Stars Identified in A22

We note the presence of three stars identified in A22 as potential surviving companion candidates that reside very near the dynamical center of SNR 0509−67.5, within 1.4 arcsec, the angular distance that an object in the LMC moving at $1000\,\mathrm{km\,s^{-1}}$ could have traveled in 317 years. These three stars are too faint to be detected by the automated aperture photometry that created the HSC. For completeness, we decided to include these stars in our search using HST magnitudes from Hovey (2016), but we note that their photometry was obtained inconsistently with the rest of the stellar population. We discuss these stars further in Subsection 3.5.4.

3.4.2   Synthetic Spectra and Photometry

Source Work	Model	Surviving Companion Type	Temperature (10^4 K)	Radius ($R_\odot$)
Liu et al. 2021	DDet* Kepler Model	He Star	1	3
Liu et al. 2021	DDet* Mesa Model	He Star	1.1	0.5
Liu et al. 2022	SD Accretion‡	He Star	4.6	0.5
Shappee et al. 2013a	SD Accretion‡	MS Star	0.52	10
Pan et al. 2013	SD Accretion‡	He Star	4	0.6
Pan et al. 2014	SD Accretion‡	MS Star	0.75	3.42
Pan et al. 2014	DDet*	He WD	5.5	0.39
Rau & Pan 2022	SD Accretion‡	MS Star	0.4	2.5
Shen & Schwab 2017	DDet*	He WD	10	0.05[†]

Table 3.2 A summary of predicted temperatures and radii from different surviving companion models at the age of the remnant ≤ 1000 yrs. Many of these works tested a variety of models. In such cases, we show the resulting temperature and radius that is the most difficult to detect, i.e. the smallest, coolest model. We show two models from works where the smallest model is not also the coolest. All combinations of temperature and radius are clearly distinguishable from the surviving companion candidates inside SNR 0509−67.5with the exception of Shen & Schwab (2017) which is too faint to detect.

[*] DDet refers to the Double Detonation model, also known as the Dynamically Driven Double-Degenerate Double-Detonation (D6) model (Shen et al., 2018).

[‡] SD Accretion refers to the single degenerate accretion scenario, in which the companion has exhausted fusion energy.

[†]Shen & Schwab (2017) did not directly present an evolving radius of the surviving companion over time. We calculated a radius using the provided luminosity and effective temperature using the Stefan-Boltzmann law.

We generated synthetic spectra by interpolating a spectral grid generated with the `PHOENIX` stellar atmosphere code (Husser et al., 2013) using `StarKit`[1] (Kerzendorf & Do, 2015). The `PHOENIX` spectra to be interpolated were sampled over effective temperature T_{eff}, logarithmic surface gravity $\log(g)$, and metallicity relative to solar $[\frac{M}{H}]$. We then scaled the spectrum by stellar radius as a free parameter to obtain a model intrinsic stellar spectrum.

We attributed all extinction to Galactic foreground dust, which is the dominant source of extinction for objects contained in the LMC (Choi et al., 2018). We reddened our stellar spectrum with a standard Galactic extinction law of $R_V = 3.1$ following Fitzpatrick (1999) with the `dust_extinction`[2] package. We note that, because of the modest cumulative amount of foreground extinction ($A_V \approx 0.28$, Joshi & Panchal 2019), the exact choice of reddening model had little effect on synthetic magnitudes generated and resulting extracted stellar parameters (roughly a maximum difference of 0.01 mags in F475W and F814W, with smaller effects in other bands). Finally, we convolved the spectrum with each HST filter curve in which a given star was observed (shown in Figure 3.4) using `wsynphot`[3] (Kerzendorf & Singhal, 2022), and integrated the resulting flux to obtain a photometric magnitude that we compared directly to each observation.

3.4.3 Bayesian Parameter Inference

We derived a multidimensional posterior probability distribution for the set of astrophysical parameters for each star with the nested sampling Monte Carlo algorithm MLFriends (Buchner, 2016, 2019) implemented in the `UltraNest`[4] package (Buchner, 2021) by comparing the observations to synthetic magnitudes generated with a given set of parameters. Our priors are presented in Table 3.3. We fixed $\log(g)$ at 3.0 as our observations were generally insensitive to variation in this space. Additionally, we fixed each star to be at a distance of 49.27 kpc, the distance of the remnant following A22, noting that any variation in distance for a given star in the LMC is small compared to other sources of uncertainty, and any variation or uncertainty here translates directly to a corresponding variation or uncertainty in radius. An uncertainty on distance of 1 kpc (2%)

---

[1] `https://github.com/starkit/starkit`
[2] `https://github.com/karllark/dust_extinction`
[3] `https://github.com/starkit/wsynphot`
[4] `https://johannesbuchner.github.io/UltraNest/`

typical for the LMC, would translate directly to an uncertainty in radius of 2%.

We begin with a standard χ^2 likelihood assuming Gaussian distributed errors for our observations given by

$$\chi^2 = \sum_{i=1}^{n} \left(\frac{m_{i,obs} - m_{i,model}}{\sigma_{i,obs}} \right)^2$$

over the observations for a given star. We adopt the log-likelihood function $ln\mathcal{L} = \chi^2/2$ for fitting.

We show an example of a single set of observations and the resulting fit in Figure 3.4. The distribution of spectra in this figure is generated by randomly sampling the posterior parameter distribution and generating model spectra as examples to show the constraints of the input observations.

3.4.4 SED Requirements

Stars only detected in the infrared F110W and F160W bands did not have sufficient observational constraints to allow for strong astrophysical characterization. As a result, we only present characterizations of stars with observations in at least two non-infrared bands. This generally required that stars be brighter than 25th magnitude, seen in the limiting magnitude estimation reported in Table 3.1.

3.4.5 Validation, Sensitivity, and Precision of Parameter Extraction

We examine the constraining power of our parameter extraction and find robust validation of our ability to recover known temperatures and radii. In Appendix 3.8.1, we fit the sun as an example and show the posterior parameter distribution. We find that the precision of our metallicity constraint is highly dependent on the temperature of the star, and in some cases virtually no information is gained and the prior is recovered. In principle, a star enriched by over an order of magnitude in metallicity, a potential signature of a surviving SN Ia companion, could be constrained and detected with HST photometry. However, no star in our sample showed an obvious metallic enhancement signature (See appendix 3.8.2 for further discussion). For this reason, we show the maximum likelihood metallicities that result from our fitting process in Figures 3.5 and 3.6, but do not further probe this parameter space for the signature of a surviving companion. Similarly, while we fit for foreground extinction and thus allow the variation in the parameter to inform the posterior, in almost all cases

we recovered our extinction prior.

In this work, we did not attempt to characterize a systematic uncertainty floor for our parameter constraints. We note that the brightest stars in our sample show unrealistically small estimated temperature uncertainties, smaller than our models are truly able to constrain tracing back to uncertainty in our model PHOENIX spectra. We report these values as they were produced and note that they do not influence our search for a surviving companion, but suggest caution when interpreting these uncertainties for other purposes.

Our various limiting magnitudes in the original observations do not easily map onto uncorrelated temperature and radius sensitivities. We estimate the sensitivity of our HSC search in the dependent parameter space as the smallest, coolest stars in our sample. For a 5000 K star this results in a sensitivity to stars larger than half a solar radius, scaling with temperature. A 10000 K star in line with the predictions of Liu et al. (2022) would need to be smaller than $0.2\,R_\odot$ to remain undetected.

3.5 Results

3.5.1 Characterized Stellar Astrophysical Parameters

We modeled the interior stellar population of SNR 0509−67.5 to extract stellar parameters and search for a surviving companion in line with those predicted by the surviving companion models shown in Table 3.2. We extracted the parameters of each star within a 10 arcsec radius of the dynamical center, too far from the center of the remnant to be the surviving companion to the exploded star, to serve as a control sample of the local stellar population, shown in Figure 3.5. We then analyzed and extracted the parameters of each star within a conservative 4.2 arcsec search region, the maximum distance a surviving companion could have traveled from the center of the remnant. This is the sample of viable surviving companion candidates, shown in Figure 3.6. In this sample, we do not detect a star substantially different from the local temperature-radius main sequence or in line with any of the models shown in Table 3.2.

3.5.2 Large Radius Stars in the Control Sample

We note the presence of two anomalously large stars in our greater control sample of 10 arcsec around the dynamical center of SNR 0509−67.5 denoted separately in Figure 3.5. An inflated star

CasJobs Match ID: 24504632
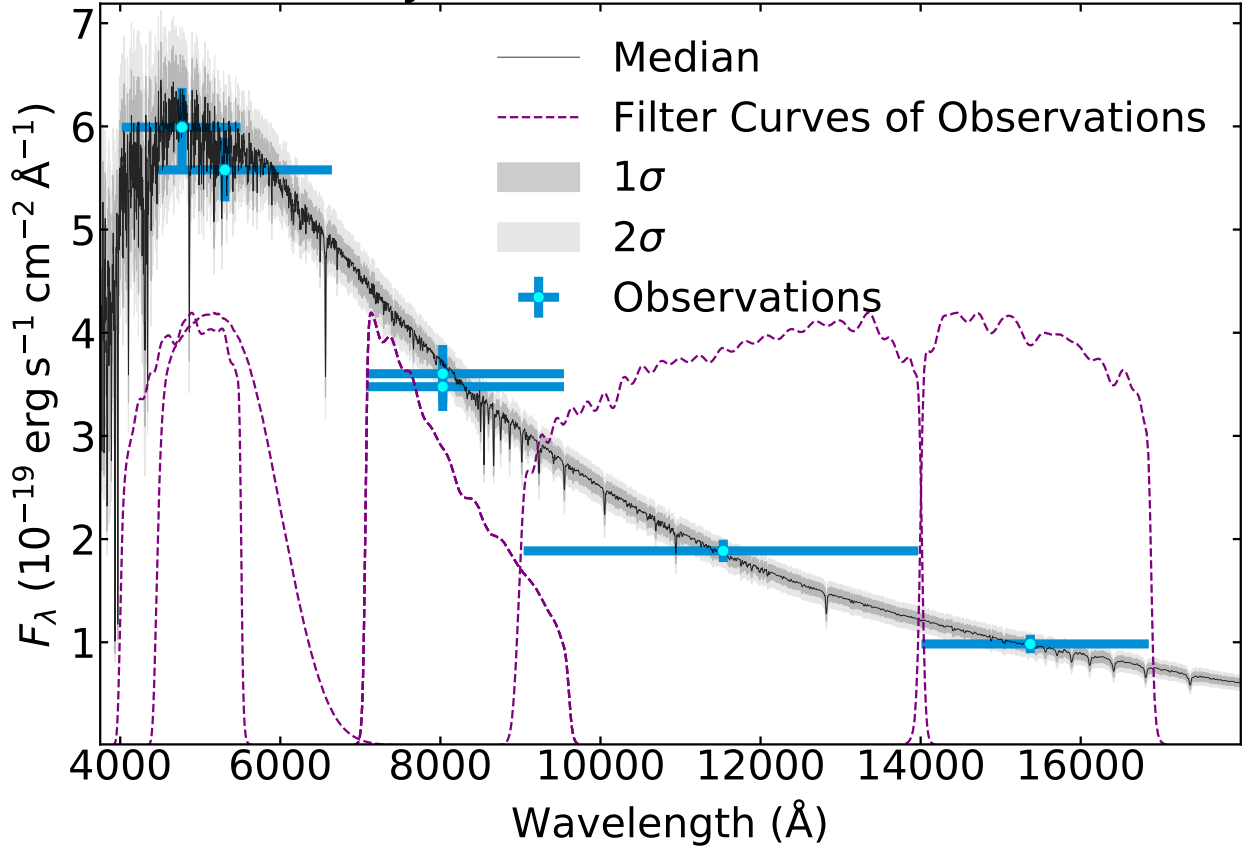
Figure 3.4 An example outcome of the fitting process for one of the stars in the search region. The blue crosses show the photometric observations with the vertical spread showing observational uncertainty, and the horizontal spread shows the width of the filter used for the observation, corresponding to the rough portion of the spectrum probed by the observation. The transmission curve of each filters is shown in dashed purple. The black and grey regions show a distribution of spectra created by sampling the posterior distribution of constrained stellar parameters.

Parameter	Prior Distribution	Source
Effective Temperature (K)	$\mathcal{U}(2300 - 12000)$	Phoenix Grid Boundaries
Radius ($R_\odot$)	$\mathcal{U}(0.05 - 10)$	Chosen Physical Boundaries
V band Absorption (mags)	$\mathcal{N}(0.28, 0.15)$ bounded at 0	Joshi & Panchal, 2019
Metallicity ($[\frac{M}{H}]$)	$\mathcal{N}(-0.34, 0.15)$	Luck et al., 1998
Distance (kpc)	49.27	Arunachalam et al., 2022

Table 3.3 A compilation of the priors used for stellar parameter inference, as well as sources where appropriate. $\mathcal{U}$ is Uniform (Lower boundary - Upper boundary), $\mathcal{N}$ is Normal(μ, σ), where μ is the mean and σ is the standard deviation. See subsection 3.4.3 for discussion of the choice of priors.
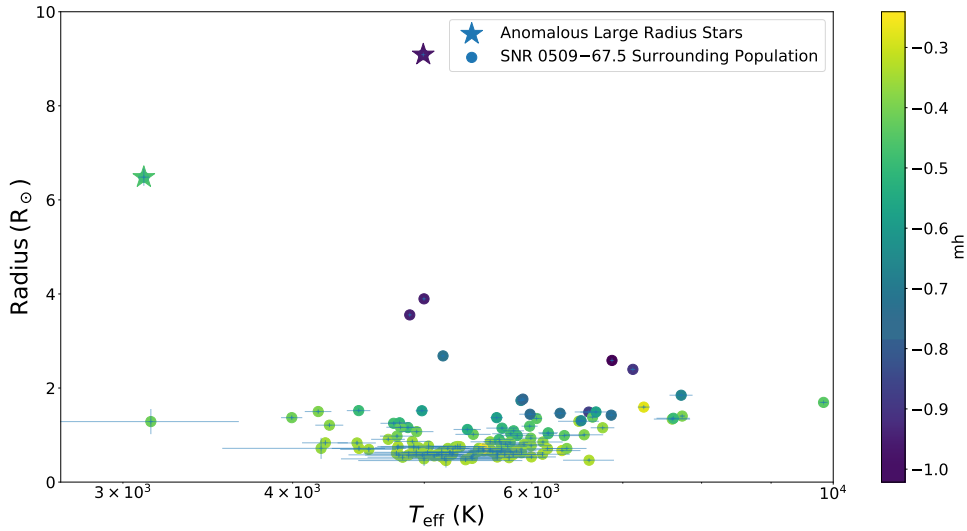
Figure 3.5 Radius vs. Effective Temperature and metallicity fits of stars in a 10 arcsec radius, excluding those close enough to the center of SNR 0509−67.5 to be the surviving companion. We used this sample to estimate the underlying main sequence distribution of stars in the local LMC. We note the presence of two anomalous large radius stars that we do not support belonging to the local main sequence population, and thus do not include in our distribution estimation in figure 3.6. We discuss these stars further in Subsection 3.5.2.

could be a tracer of a surviving companion, however neither of these stars lie close enough to the dynamical center of the remnant to be associated with the Type Ia event. We highlight that a large radius here is not necessarily physical because radius is degenerate with distance and all stars were assumed to be at the distance of the SNR 0509−67.5 for fitting. We favor the explanation that stars with anomalously large radii here are either foreground Galactic halo stars or red giants.

We examined the Besancon Galaxy model (Robin et al., 2012) to investigate the possibility of observing a foreground Galactic halo star in our sample. We sampled 10 arcsec cones oriented towards the LMC and found a stellar surface number density of 1.1×10^{-3} arcsec^{-2}, or 0.359 stars in a 10 arcsec radius circle on average. Assuming star counts are Poisson distributed, we calculate a 30.2% chance to observe one or more Galactic halo stars, and a 5.1% chance to observe 2 or more. Assuming the 3000 K star in Figure 3.5 is in the foreground, scaling its radius appropriately by roughly a factor of 10 for a halo star would place it firmly on the main sequence, making this a likely explanation. Additionally, A22 identified this star (also known as star M in Schaefer &
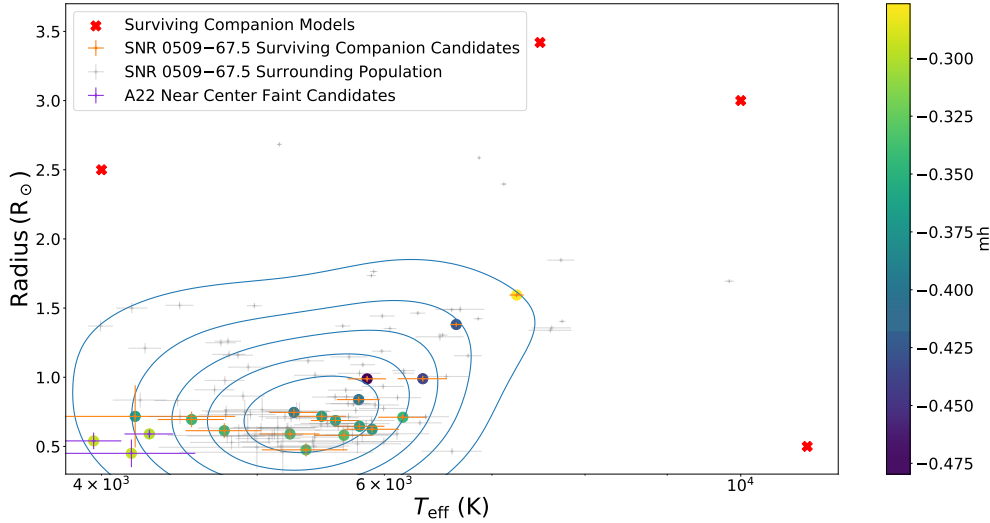
Figure 3.6 Radius vs. Effective Temperature and metallicity fits of stars within 4.2 arcsec of the hydrodynamic center of SNR 0509−67.5, the sample of potential surviving companion stars. The gray crosses show the surrounding control sample from Figure 3.5 which we used to estimate the underlying temperature-radius distribution of the local stellar population, shown by the contours. The purple crosses show the three stars identified in A22. The red X markers show surviving companion models from Table 3.2 close enough to be compared, with the other models too high in temperature or large in radius to be placed within the bounds of the figure.

Pagnotta 2012) as possessing the largest proper motion in and around the remnant, consistent with it residing in the foreground and further strengthening this identification.

The star that we measured to have a radius of $9.5\,R_\odot$ and a temperature of $5000\,K$ resides in a portion of temperature-radius space occupied by evolved red giants in the LMC, and we support this identification as well. We emphasize that neither of these two stars lie close enough to the center of the remnant to be a surviving companion to the exploded star, so we prefer these alternative explanations. We do not include either of the two stars discussed here in our Kernel Density Estimation that we use to compare to the population of surviving companion candidates due to their likely non-LMC main sequence identities.

3.5.3 Comparison To Surviving Companion Models

We have gathered a compilation of models that make concrete predictions about the effective temperature and radius of a surviving SN Ia companion on timescales appropriate for the SNR

0509−67.5($10^2 - 10^3$ yrs), shown in Table 3.2. The considered surviving companion models shown predict that the star will either be hotter than 10000 K or inflated to larger than 2.5 $R_\odot$. Our set of observations is sensitive to stars hotter than 5000 K or larger than 0.6 $R_\odot$. Therefore, we rule out this set of surviving companions from existing within SNR 0509−67.5 , as each model would be distinguishable from the sample of potential surviving companions in Figure 3.6.

Other surviving companion models not considered here can be easily tested and sought out in this remnant by comparing to our characterized stellar catalog. We show examples of our fit parameters in Table 3.4, and provide the full characterized catalog online.

MatchID	MatchRA	MatchDec	teff	teff_err	rad	rad_err	mh	mh_err	av	av_err	Near_center
1105108	77.37689	-67.52006	5658.51	352.269	0.533	0.064	-0.33	0.153	0.285	0.134	False
1240861	77.3773	-67.52317	5414.569	244.166	0.54	0.036	-0.349	0.145	0.269	0.137	False
2094417	77.37589	-67.52166	6607.698	94.121	1.489	0.014	-0.872	0.129	0.037	0.054	False
2360222	77.3794	-67.52045	6650.82	54.514	1.381	0.012	-0.424	0.136	0.027	0.03	True
4275360	77.38571	-67.52132	5655.744	225.258	0.617	0.031	-0.348	0.152	0.313	0.136	False
4304067	77.3827	-67.52268	5203.318	193.617	0.716	0.035	-0.352	0.146	0.311	0.138	False
4705369	77.37783	-67.52192	5789.892	210.41	0.646	0.027	-0.363	0.142	0.28	0.134	True
4728380	77.3771	-67.51996	4997.528	8.752	3.896	0.013	-0.96	0.057	0.003	0.004	False
4769912	77.37471	-67.52032	5758.987	189.441	0.761	0.025	-0.364	0.141	0.263	0.13	False
5394004	77.37623	-67.51961	5161.428	16.844	2.683	0.015	-0.721	0.114	0.007	0.01	False

Table 3.4 An abbreviated example of 10 stars with their extracted parameters. The full table including the magnitudes used for fitting is available as a supplemental online data product.

3.5.4 Results of Stars Identified in A22

3.6 Discussion

We have conducted a deep, systematic search of the Ia remnant SNR 0509−67.5 to identify a surviving companion, using a sample of existing archival HST wide band photometry. We investigated a large enough search region to allow for the fastest moving surviving companions, i.e. hypervelocity white dwarfs tracing back to double detonation progenitor systems (e.g. Shen et al., 2018). All models, regardless of the explosion mechanism of the primary, predict that a nearby secondary that is impacted by expanding supernova ejecta will show some combination of high effective temperature or inflated radius for at least thousands of years. In Table 3.2, we show a compilation of expected lower temperatures and radii predicted from various models approximately 1000 years after being impacted by SN Ia ejecta. In contrast, none of the stars inside the SNR 0509−67.5 close enough to the center to be surviving companion candidates in the remnant show astrophysical parameters that suggest exotic identities. For any of the models considered here, this finding rules out the existence of such a surviving companion as such a star would be clearly identifiable as separate from the main sequence stellar population. We note that we cannot rule out the existence of a He WD companion in line with Shen & Schwab (2017) in SNR 0509−67.5. However, this model solely considered luminosity generated due to the delayed decay of ^{56}Ni on the surface of the donor WD, which may not remain the dominant source of over-luminosity at timescales associated with the remnant (see e.g Pan et al., 2014; Liu et al., 2021).

We rule out the existence of a surviving companion in the remnant down to a limiting optical AB magnitude of 25.5, with the one exception being that the surviving companion is indistinguishable from the local stellar population in combined temperature-radius space. The list of considered surviving companion models we show is not exhaustive, and new models not yet explored or published are still in development. We encourage models not considered here to be compared to the astrophysical properties of this stellar population.

3.6.1   Spin-up/spin-down models

This work probes the interior stellar population of SNR 0509−67.5 for signatures of interaction both before and during the explosion of the primary WD. The models we show in Table 3.2 generally assume that the surviving companion is close enough to the primary when it explodes for the secondary to experience Roche lobe overflow. However, some models have been proposed in which the secondary donates mass to the primary C/O WD before the process halts and the secondary evolves in isolation. The mass transfer process imparts additional angular momentum onto the primary C/O WD which prevents it from experiencing thermonuclear runaway until it can dissipate the accrued angular momentum or spin down (Di Stefano et al., 2011; Justham, 2011; Hachisu et al., 2012). The spin-down timescale is poorly constrained to be between 10^5 and 10^9 years (but see Kerzendorf et al. 2018b and enclosed references for further constraints), and the secondary may have time to exhaust hydrogen evolve in to a WD. If so, the secondary can retain a large enough orbital separation from the primary to remain largely unaffected by the explosion. The secondary will then remain near the center of the remnant as an isolated WD that has cooled for up to the spin-down time. No isolated WD is detected in the archival photometry used in this work near the center of SNR 0509−67.5 , which can be translated to a constraint on spin-down timescale of the system that is dependent on the mass of the companion (see Di Stefano & Kilic 2012, but also Meng & Podsiadlowski 2013 for further discussion).

3.7   Conclusions

We present a full stellar classification of the interior stellar population to SNR 0509−67.5 to probe the parameter space sensitive to ejecta interaction and search for a surviving companion to the exploded star that created the remnant. We considered a generous search region corresponding to an ejection velocity of $2500\,\mathrm{km\,s^{-1}}$ and a remnant expansion age of 400 years. Within this region, we do not detect an anomalously hot or radially extended star as predicted by the interaction of supernova ejecta with a nearby companion in both the degenerate and non-degenerate companion cases in which the companion survives.

This result holds consistent with other recent non-detections of surviving companions in Ia

remnants that may point to SN Ia progenitor channels that do not leave bound stellar remnants behind (see Ruiz-Lapuente 2019). However, the sporadic nature of previous surviving companion searches with inconsistent limits and parameter space exploration makes conclusive statements about the viability of specific progenitor channels difficult to support.

The constraints of the LMC as well as the new developments to the HSC that made the stellar characterization central to this work possible remain consistent across other known SN Ia remnants in the LMC. Similar studies of those remnants would enable statistical statements about the viability of specific progenitor channels.

3.8 Appendix

3.8.1 Methodology verification - The Sun

To validate our stellar astrophysical parameter extraction, we obtained AB magnitudes and magnitude uncertainties of the Sun from Willmer (2018). We applied the same methodology that we used in our study to these observations, excluding our treatment of dust, to recover derived solar astrophysical parameters. Specifically, we obtained the same five HST band AB magnitudes from our work, F475W, F555W, F875W, F110W, and F160W, and performed Bayesian inference to extract stellar parameters which we could then compare to known intrinsic values. The results of the parameter extraction are shown in Figure 3.7. We used the same uninformative uniform temperature and radius priors as in the rest of our work but changed the metallicity prior to a normal distribution centered on solar metallicity (Mean = 0.00, $\sigma = 0.15$). As shown, our methodology powerfully constrains the temperature and radius of the star, producing strong agreement with true values, but once again recovering the prior on metallicity. See Appendix 3.8.2 for further discussion on our metallicity constraints.

3.8.2 Measuring Metallicity With Photometry

We report metallicity measurements for each of the stars in this work but do not attempt to quantitatively probe this space for surviving companions. We made this choice because both the general ability of pure photometry and the combination of filters required to detect metallicity enhancement in a star has a complex relationship with effective temperature. In Figure 3.8 we
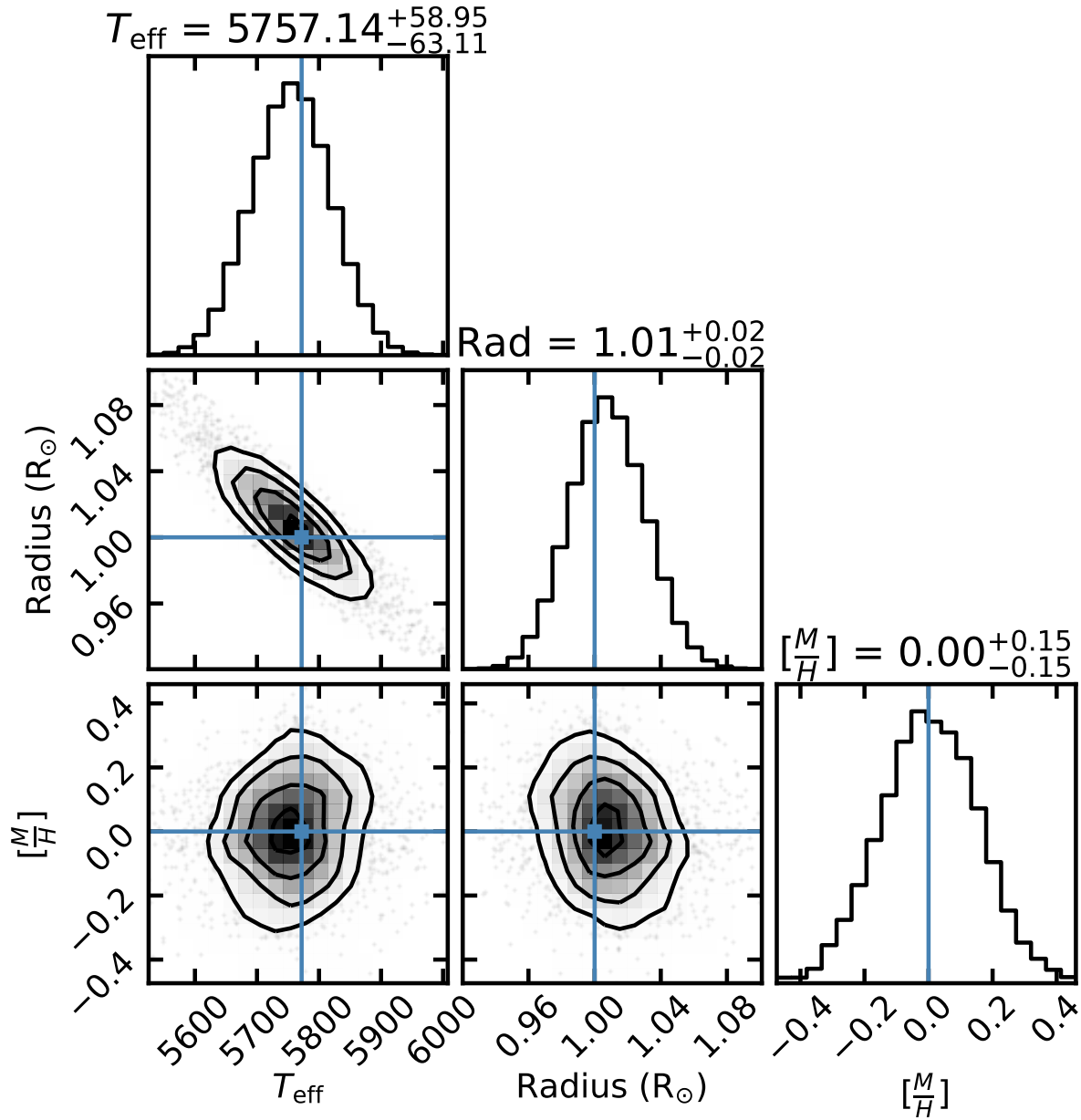
Figure 3.7 An example fit corner plot of extracted astrophysical parameters of the Sun for methodological validation. We obtained and fit magnitudes from Willmer (2018). The true values are shown with blue lines. Our parameter extraction shows strong agreement with the true solar values of temperature and radius, within 1σ.

show the relative differences in flux between metal-poor ($[\frac{M}{H}] = -1$) and metal-rich ($[\frac{M}{H}] = 1$) stars at 6000 K and 10000 K. For the filters used in this work, [F475W, F555W, F814W, F110W, and F160W] these stars would show differences of [-0.04, 0.07, 0.17, 0.13, 0.04] mags and [0.15, 0.15, 0.14, 0.11, 0.11] mags at 6000 K and 10000 K respectively. The difference in metallicity for

both temperature stars is possibly constrained by photometry, but this enrichment in a 6000 K star creates a more obvious signature, distinguishable from a change in temperature or radius.

In either case, the level of metallic enrichment expected for a surviving companion could potentially be constrained from the photometry of this work, as the differences in HST magnitudes from comparing the spectra in Figure 3.8 are significantly higher than the uncertainties of many observations, especially in the brighter stars in our sample. However, none of the stars in our sample showed an obvious signature tracing back to a departure from typical LMC metallicities, so the metallicities of stars in our sample are usually not constrained beyond our prior.

3.8.3   Investigating HHE 5

In Figure 3.9, we show our fit of the SED belonging to HHE5 and originating from photometry in Hovey (2016). The F814W measurement lies multiple standard deviations away from the constrained spectrum, and in general cannot lie on a standard stellar spectrum anchored by the infrared observations. Investigating further, we note that the F814W measurement of HHE 5 is the faintest F814W measurement present in the reported catalog of Hovey (2016). While not conclusive, this could point to the measurement being unphysical.

The location of HHE 5, very near the dynamical center of SNR 0509−67.5, is the strongest argument in favor of a surviving companion identification, and we acknowledge that the unusual photometry here could be seen as further support towards an exotic identification. However, no current surviving companion models predict the narrow F814W suppression seen in the SED. We support the explanation that the F814W measurement is unphysical, rather than invoking an exotic scenario capable of explaining this feature.
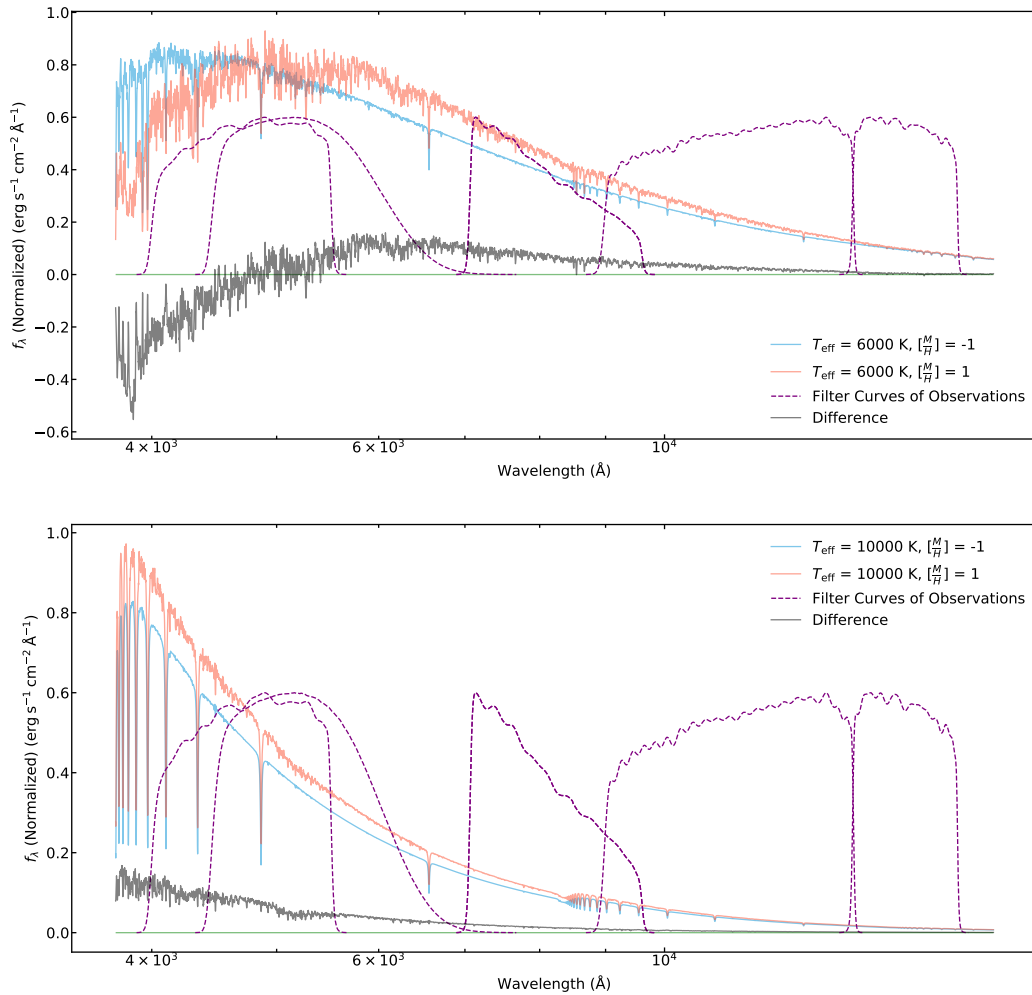
Figure 3.8 An example showing the effects of metallicity at different temperatures. The top panel shows the spectra of a metal-poor ($[\frac{M}{H}] = -1$) 6000 K star and a metal-rich ($[\frac{M}{H}] = 1$) 6000 K star. The bottom shows the same, but comparing 10000 K stars. The purple dashed lines show the transmission curves of the same filters used in the rest of this work, and the gray line shows the difference between the two spectra. At some temperatures, sufficiently sensitive photometry is capable of constraining metallicity, detecting relative enhancements and diminishments in the redder and bluer optical portions of the spectrum.
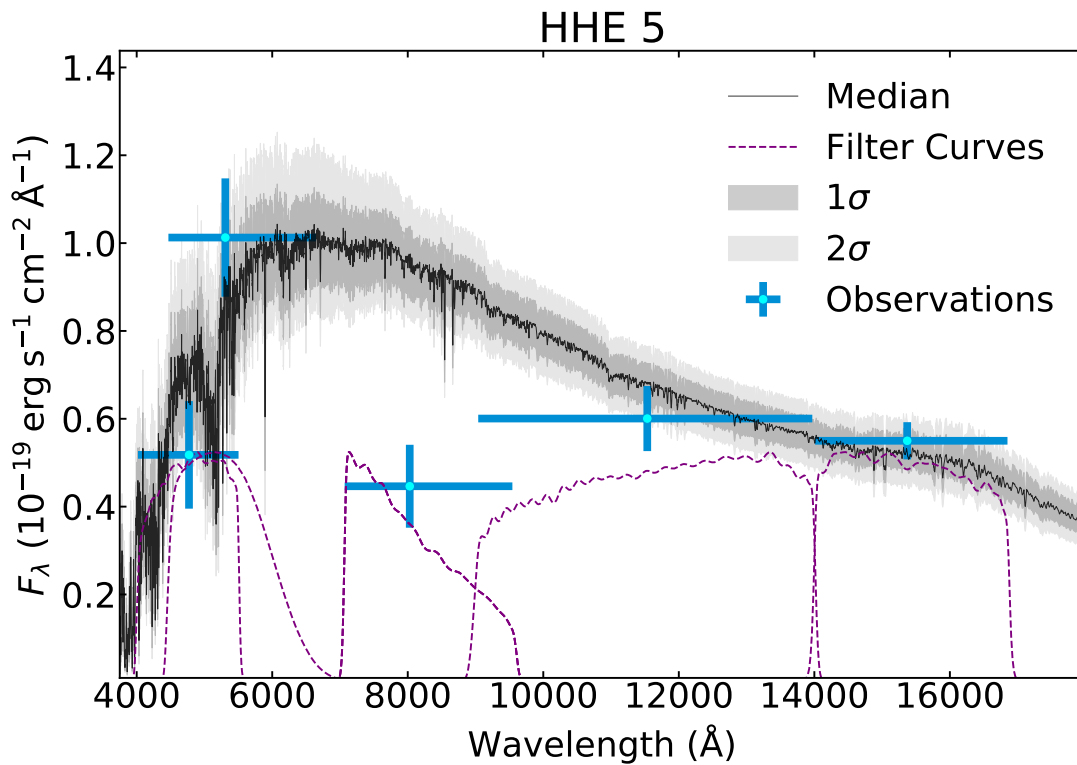
Figure 3.9 Our fit for HHE 5, similar to that shown in Figure 3.4. The model does a poor job fitting the observations, primarily because of the single F814W observation that is impossible to explain with a stellar spectrum capable of fitting the other four observations. The other points can be suitably explained by a typical stellar spectrum, in accordance with the possibility of an unphysical F814W measurement.

CHAPTER 4

STARDIS: A MODERN STELLAR SPECTRAL SYNTHESIS CODE

The following chapter presents currently unpublished but ongoing work led by J. V. Shields. It is on track to be published in 2024.
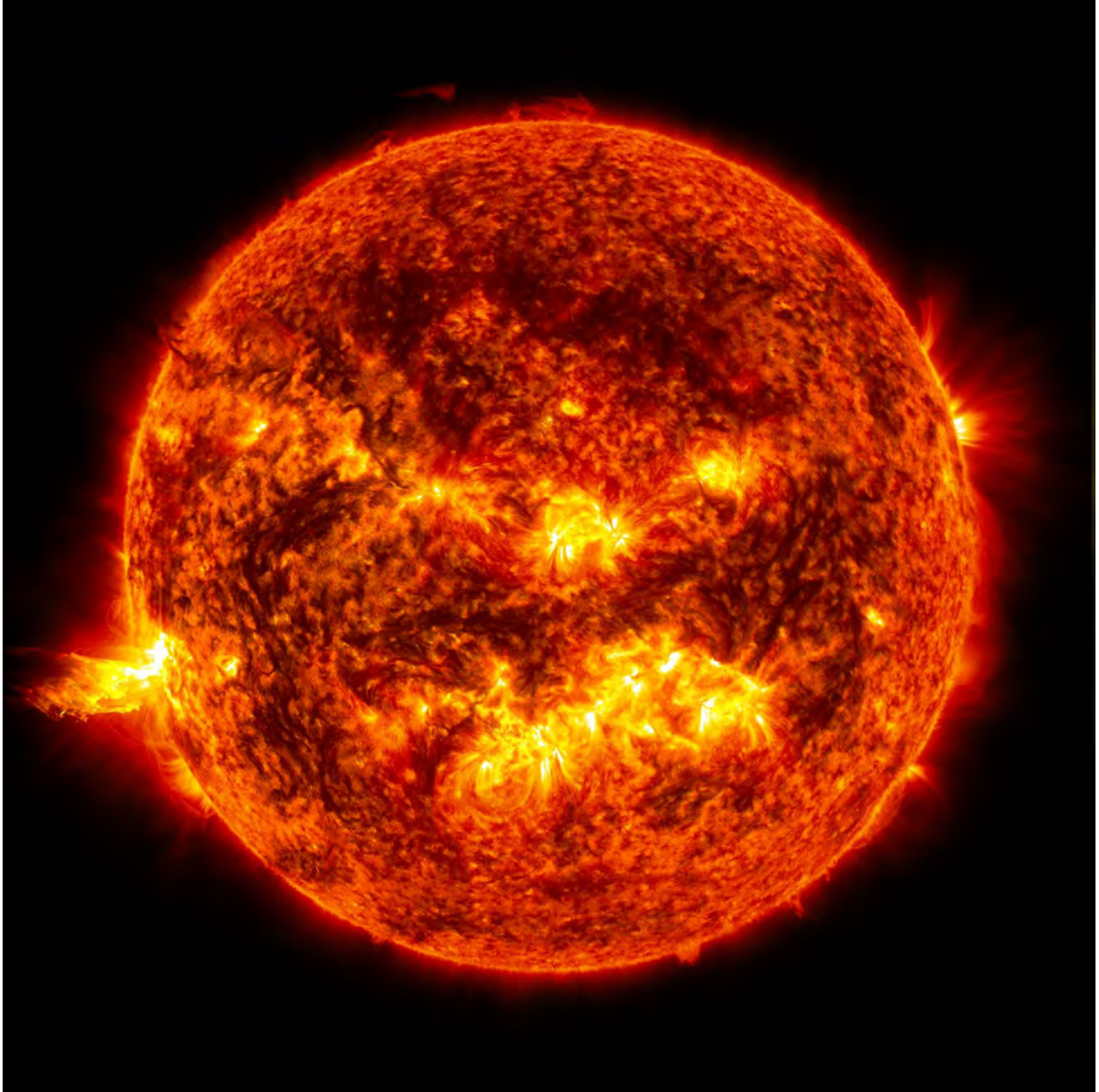
Figure 4.1 The Sun. Credit: NASA/SDO

4.1 Abstract

We introduce a new 1D open-source finite-difference stellar atmospheric spectral synthesis python code called STARDIS. STARDIS is a modular, open-source radiative transfer code that is capable of spectral synthesis from IR to near-UV. Future updates to the code will expand functionality to the UV, and allow the user to relax some of the LTE assumptions currently used in the code. We describe the structure, inputs, features, underlying physics, and assumptions of STARDIS as well as the radiative transfer scheme implemented. We also compare STARDIS to KORG, an independent pre-existing stellar radiative transfer code, to test for correctness with as similar inputs as possible. We find that STARDIS generally agrees with KORG to a similar level of precision as KORG to other stellar spectral synthesis codes. Finally, we provide benchmarks and describe future developments to the code. STARDIS can be found at https://github.com/tardis-sn/stardis, and documentation can be found at https://tardis-sn.github.io/stardis/.

4.2 Introduction

The practice of measuring chemical abundances in stars has been and remains a powerful tool in astrophysics. This practice primarily entails comparisons of synthetic stellar spectra to observed ones, specifically matching the observed chemical line features against synthetic spectra generated over a set of astrophysical stellar parameters (i.e., varying the composition and structure of the stellar atmosphere to create a set of models). Critical to this process is the generation of synthetic stellar spectra, which has been handled by a suite of codes over the past 50 years. These include, but are not limited to, MOOG (Sneden, 1973; Sneden et al., 2012), TURBOSPECTRUM (Plez, 2012), SYNTHE (Kurucz, 1993; Sbordone et al., 2004), SME (Valenti & Piskunov, 1996), SPECTRUM (Gray & Corbally, 1994), SYNSPEC (Hubeny & Lanz, 2011), PHOENIX (Baron et al., 2010; Husser et al., 2013), and KORG (Wheeler et al., 2023). These codes have collectively enabled a staggering body of science spanning the study of stellar and planetary atmospheric chemical abundances, galactic evolution, stellar evolution, and more. However, none of the codes are public, open-source, actively maintained, easily accessible and approachable, modular, and written in current popular coding languages. Indeed, KORG is the only open-source stellar synthesis code

released recently or being actively maintained. These problems hinder the continued expansion and application of those codes to meet the evolving needs of the stellar astrophysical community.

To remedy this, we present STARDIS, an open-source finite-difference stellar atmospheric spectral synthesis code written in python. The code is built in conjunction with and upon much of the existing machinery of the TARDIS code (Kerzendorf & Sim, 2014, detailed explicitly in section 4.3)). As such, current and future code developments of either can be used across the shared codebase (e.g., atomic data parsing, plasma solvers, etc.). STARDIS is currently functional as a 1D plane-parallel hydrostatic local thermodynamic equilibrium (LTE) radiative transfer code, and all analysis and comparison done in this work has been performed in this mode. However, we have written STARDIS to be highly modular and easily expandable both by current active developers, as well as future contributors with highly specific science cases. For instance, NLTE detailed chemical balance calculations that can be swapped in place of current chemical excitation and level population solvers are in development, and more generally the code is written to be modified and expanded. Finally, because the code is written in python, accessible on github, and maintained by an active collaboration, we intend it to be approachable with a low barrier to contribution.

Our goal is to provide an analysis tool that is flexible enough to model both typical and non-standard stellar systems and modular enough to include the specific physics needed to achieve that goal. Arbitrary chemical composition and thermodynamic quantity profiles can be supplied by the user, allowing for the study of perturbed systems. Additionally, STARDIS is connected to a robust atomic data ingestion code which can be used to prepare novel combinations of atomic data sources called `Carsus`[1].

In section 4.3 we describe the code, including the inputs and the calculations that it performs in order to obtain a synthetic spectrum. In section 4.4 we compare synthetic spectra produced by STARDIS chiefly to those generated over the same parameters with KORG. In section 4.5 we provide benchmark statistics. Finally, we conclude in section 4.6 with final remarks and discussion.

---

[1]https://tardis-sn.github.io/carsus/

4.3 Code Description

STARDIS breaks spectral synthesis into four key steps. It begins by initializing the atmosphere constructed and solved by an outside source, currently either output by MARCS (Gustafsson et al., 2008) or MESA (Paxton et al., 2011, 2013, 2015, 2018, 2019; Jermyn et al., 2023) (though the atmosphere at this stage can also be modified, or entirely fabricated by the user) described in section 4.3.1. This provides the temperatures, densities, chemical compositions, and structure of the stellar plasma. STARDIS then computes the state of the stellar plasma, detailed in section 4.3.1.2. Next, STARDIS computes the opacity of the plasma at each requested wavelength at each point in the atmosphere, explained in sections 4.3.3 and 4.3.4. Finally, STARDIS uses a raytracing prescription to solve the radiative transfer equation at each depth point throughout the atmosphere and obtain an output stellar spectrum at the stellar surface, described in 4.3.5.

4.3.1 Simulation Inputs

A STARDIS simulation needs a short list of various physical inputs to generate a spectrum. It needs the structure and composition of the atmosphere to be supplied (Section 4.3.1.1) and a source of atomic data to supply necessary information for chemicals in the atmosphere (Section 4.3.1.2). It can optionally be supplied with a linelist that will be used to calculate line transition features in the spectrum, but not to determine the chemical equilibrium at this stage. Also, it can be supplied with any additional sources of opacity desired by the user, which will usually be sources of continuum opacity not already calculated by the code. Finally, the code requires a configuration file that specifies the exact prescription of code to be run (i.e., what physics the user wants to include as well as computational choices such as how many threads to allow for multiprocessing).

4.3.1.1 Atmospheric Structure

STARDIS is intended to be a post-processing code that determines the spectrum generated by a star with a given atmosphere. This means that STARDIS does not solve for the atmosphere of the star, nor check to see that it can exist in hydrostatic equilibrium. Rather, the temperature, density, and chemical composition of the atmosphere must be read in from another source or supplied/adjusted by the user. As of the time of this work, STARDIS can ingest two model atmosphere sources. First,

the code can read in a MARCS[2] (Gustafsson et al., 2008) model atmosphere. MARCS models are 1D, plane-parallel, hydrostatic models calculated either in plane-parallel or spherical symmetry and include full chemical profiles. Second, the code can read in a MESA (Paxton et al., 2011, 2013, 2015, 2018, 2019; Jermyn et al., 2023)[3] model to initialize the atmosphere. MESA models are by nature highly flexible and not necessarily prepared for radiative transfer. Additionally, because MESA models generally do not feature complete chemical reaction networks, either a chemical profile supplied by the user or a scaled solar profile must be specified for STARDIS. In theory one could use chemical tracers supplied by MESA to infer a complete, accurate chemical profile, but that is beyond the scope of our initial code release.

Whether the atmospheric initialization is provided by MARCS or MESA, the chemical profile can be altered to suit the needs of the user. However, it should be noted that the atmospheric structure is in part a function of the chemical composition of that atmosphere. Small departures from the chemical composition of the input atmosphere will likely not have significant effects on the physical atmosphere being modeled, but it is worth noting that STARDIS will not verify the consistency of the atmosphere being supplied. STARDIS will solve the radiative transfer equation for the atmosphere in any case, whether or not the atmosphere being supplied is physically consistent or satisfies hydrostatic equilibrium. In our experience, the largest pitfall at this stage is if the model does not extend far enough into the stellar atmosphere.

4.3.1.2   Chemical Data and Linelists

In order to solve the state of the stellar plasma (i.e. the ionization states of the chemicals, see section 4.3.2), as well as other various important processes to the code, STARDIS requires information about the chemicals that compose the atmosphere. Specifically, STARDIS needs the atomic weights, ionization energies, energy levels, and information about line transitions of the atoms. This information is collected from a variety of sources and synthesized through the `Carsus` package (Pássaro et al., 2020), another standalone code within the larger TARDIS codebase.

Additionally, `Carsus` can parse and prepare a linelist, principally from the Vienna Atomic

---

[2]Available at MARCS
[3]See the MESA homepage

Line Database (VALD Piskunov et al., 1995; Ryabchikova et al., 1997; Kupka et al., 1999, 2000; Ryabchikova et al., 2015; Pakhomov & Ryabchikova, 2019). When provided, STARDIS will calculate line transitions from these lists rather than calculate transitions from reconstructed atoms. Empirically calibrated VALD linelists provide the most accurate, complete sets of atomic line transitions currently available.

4.3.2 Chemical Equilibrium

In order to compute the opacity of the stellar plasma and solve the radiative transfer equation in the stellar atmosphere, the code must first calculate the number density of each chemical in each ionization and excitation state. STARDIS shares its machinery for solving the stellar plasma with its parent code TARDIS, and detailed descriptions of and justifications for the chemical balance equations can be found in Kerzendorf & Sim 2014. In short, chemical populations are currently calculated in LTE using the Saha-Boltzmann ionization equation an

$$\frac{n_{i,j+1}n_e}{n_{i,j}} = \frac{2Z_{i,j+1}(T}{Z_{i,j}(T)} \left(\frac{2\pi m_e kT}{h^2} \right)^{3/2} e^{\frac{-\chi_{i,j}}{kT}} \tag{4.1}$$

as well as Boltzmann excitation equation

$$n_{i,j,k} = \frac{g_{i,j,k}}{Z_{i,j}} N_{i,j} exp(-\epsilon_{i,j,k}/kT) \tag{4.2}$$

where n is the number density, i, j, k are indices for energy level, ionization state, and element respectively, Z is the partition function, and χ is the ionization potential. In the second equation g is the degeneracy of the state, and ϵ is the excitation energy of the state relative to the ion ground state.

Molecules other than H_2 are not currently calculated, but are important for many absorption features in cool stars and will be added in a future update. NLTE detailed balance calculations are also in development, but will likely be significantly more computationally expensive to run so the user will need to choose between code expediency and more accurate chemical populations for their use case.

4.3.3 Continuum Opacities

Total continuum opacities at each wavelength and stellar depth point are ultimately due to a number of physical processes that must be calculated independently and summed. These can be separated into four categories in stellar atmospheres being: Rayleigh scattering, Thomson scattering, bound-free interactions, and free-free interactions. In any case the calculation follows the same prescription of finding the cross section of a particle due to some physical process and then multiplying that cross section by the number density of that particle to obtain an opacity (and we note that this is the same prescription as in the line opacity case). That is,

$$\alpha_{i,j}(\nu) = \sigma_{i,j}(\nu)n_i \tag{4.3}$$

and

$$\alpha_{total}(\nu) = \sum_{i,j} \alpha_{i,j}(\nu) \tag{4.4}$$

where α is the opacity, σ is the cross section, and n is the number density. i indexes the particle and j indexes the physical process. Cross sections and thus opacities are thus often but not always dependent on the frequency ν.

We will discuss each of the continuum opacity sources in turn.

We implement Rayleigh scattering following analytic expressions given in Colgan et al. 2016 for the H and He cross sections

$$\sigma_{\mathrm{H}}/\sigma_{\mathrm{Th}} = 20.24 \left(\frac{\hbar\nu}{2E_{\mathrm{H}}}\right)^4 + 239.2 \left(\frac{\hbar\nu}{2E_{\mathrm{H}}}\right)^6 + 2256 \left(\frac{\hbar\nu}{2E_{\mathrm{H}}}\right)^8 \tag{4.5}$$

$$\sigma_{\mathrm{He}}/\sigma_{\mathrm{Th}} = 1.913 \left(\frac{\hbar\nu}{2E_{\mathrm{H}}}\right)^4 + 4.52 \left(\frac{\hbar\nu}{2E_{\mathrm{H}}}\right)^6 + 7.90 \left(\frac{\hbar\nu}{2E_{\mathrm{H}}}\right)^8 \tag{4.6}$$

where $\sigma_{\mathrm{Th}} = 6.65246 * 10^{-25} \mathrm{cm}^2$, the Thomson scattering cross section. Rayleigh scattering due to other atoms or molecules is currently ignored, which is physically justified because they are not large sources of opacity in F, G, or K type stars. Additional sources will be added as needed.

Thomson scattering is relatively straightforward because it is independent of frequency so it is calculated as

$$\alpha = \sigma_{Th} n_e \tag{4.7}$$

where σ_T is once again the Thomson scattering cross section and n_e is the electron density.

Bound-free and free-free cross sections are either calculated using an analytical approximation or sampled from an interpolated function constructed from empirically measured opacity tables. Our analytic approximations are implemented following Hubeny & Mihalas 2014. That is

$$\sigma_{bf} = \frac{64\pi^4 Z^4 e^{10} m_e}{3\sqrt{3} c h^6} \frac{g_{bf}}{n'^5 \nu^3} \tag{4.8}$$

where Z is the charge of the particle, m_e is the mass of the electron, g_{bf} if the bound-free Gaunt factor, n' is the energy level of the electron, and ν is the ionization frequency. Gaunt factors represent quantum mechanical departures from the classical representation, and are supported but not currently implemented. In this case, the equation shown reduces to Kramers' opacity law.

Free-free cross sections are calculated similarly as

$$\sigma_{ff} = \frac{\sqrt{32\pi} Z^2 e^6}{3\sqrt{3} c h (k m_e^3 T)^{1/2}} \frac{\bar{g}_{ff}}{\nu^3} \tag{4.9}$$

where k is the Boltzmann constant, and $\bar{g}_{ff}$ is once again a Gaunt factor correcting the equation for quantum mechanical effects.

These equations are good first approximations that allow STARDIS to include the bound-free and free-free opacities for any generic particle and state as needed. However, for important bound-free and free-free opacity contributors, the user may wish to include empirical treatments to more precisely model the effects.

For these cases, there exists a bulk of scientific literature studying specific sources of opacity, calculating contributions of specific species to opacity by measuring temperature and/or wavelength dependent cross sections of those species. STARDIS currently includes three such studies that allow for more precise calculations of individual opacities. They are: H$^-$ bound-free interactions from

76

Wishart 1979 (i.e., the interaction of a photon with a proton with two bound electrons, which is an important source of continuum opacity in the solar atmosphere), H^- free-free interactions from Bell & Berrington 1987 (confusingly, in contrast to the immediate previous interaction type, now simply the interaction of a photon and a free electron mediated by a neutral H), and H_2^+ bound-free interactions following Stancil 1994. In cases such as these, STARDIS linearly interpolates a cross section table over wavelengths or wavelengths and temperatures as appropriate and resampled at the parameters of the stellar atmosphere. Once obtained, the opacities are calculated in the usual way following equation 4.3.

The specific handling of the three explicit opacity sources mentioned is sufficient for accurate treatment of the solar photosphere, but may not be sufficient for other cases not considered here. For this reason, and in line with the intended modularity of STARDIS, opacity tables can easily be ingested and used in the code.

4.3.4 Line Opacities

STARDIS has two similar but distinct methods of calculating bound-bound atomic transition opacities. The first makes use of fully reconstructed atoms with complete information of the upper and lower levels involved in a given line transition. Opacities are calculated following Rybicki & Lightman 1986. Beginning from equation 4.3, we substitute for the frequency integrated cross section of an atom for an excitation transition from a lower state to an upper state

$$\sigma = \frac{\pi e^2}{m_e c} f_{lu} \tag{4.10}$$

noting that the subscript l denotes the lower level, the subscript u denotes the upper level of a transition, and f_{lu} is the oscillator strength associated with the transition from the lower level to the upper level. With two key changes which will be explained momentarily, we arrive at the equation

$$\alpha(v) = \frac{\pi e^2}{m_e c} n_l f_{lu} \left[1 - \frac{g_{lower} n_{upper}}{g_{upper} n_{lower}} \right] \phi(v) \tag{4.11}$$

$\left[1 - \frac{g_{lower} n_{upper}}{g_{upper} n_{lower}} \right]$ is the stimulated emission factor, and appropriately accounts for a reduction in opacity related to photons being re-emitted at the same frequencies that are being absorbed.

$\phi(\nu)$ is the Voigt profile, which handles the broadening of the line across frequency space and is discussed at length in section 4.3.4.1.

A modification to this approach is necessary when STARDIS calculates line opacities that come from linelists which are common in astrophysics. In contrast, a linelist does not attempt to fully reconstruct an atom and supply an excitation energy and degeneracy for every energy level of an atom, and an oscillator strength of each possible transition. Rather, a linelist will be provided for a given wavelength or frequency regime, and specific line transitions will be listed in that region. While not necessarily physically consistent, linelists allow for empirical calibration and tuning to produce more accurate individual transitions are currently possible first principles. In practice, this means that a linelist may list a specific transition without all of the associated degeneracies, and instead report a single "gf" value. In such a case, the lower level population of the transition is not explicitly calculated,

$$\alpha_{\text{linelist}}(\nu) = \frac{\pi e^2}{m_e c} n_{ion} g f_{lu} \left[1 - e^{-h\nu/kT} \right] \phi(\nu) \tag{4.12}$$

and instead we calculate the stimulated emission factor as $[1 - e^{-h\nu/kT}]$ following Rybicki & Lightman (1986).

The most complete and accurate linelists are currently available through the VALD database (Piskunov et al., 1995; Ryabchikova et al., 1997; Kupka et al., 1999, 2000; Ryabchikova et al., 2015; Pakhomov & Ryabchikova, 2019) which includes individual lines from a wide variety of sources. STARDIS supports direct ingestion of and line opacity calculations from these linelists.

4.3.4.1 Line Broadening

Atomic spectral features are subject to line broadening. A line transition can be prompted by a photon over a range of frequencies which can be described by a Voigt profile. A Voigt profile is the convolution of a Gaussian and a Lorentzian, which describe the thermal broadening and the non-thermal sources of line broadening respectively.

$$\phi(x; \sigma, \Gamma) = \int_{-\infty}^{\infty} G(x'; \sigma) L(x - x'; \gamma) dx' \tag{4.13}$$

where $G(x; \sigma)$ is the expected Gaussian

$$G(x; \sigma) = \frac{1}{\sigma\sqrt{2\pi}}\exp\left(-\frac{x^2}{2\sigma^2}\right) \tag{4.14}$$

and $L(x; \gamma)$ is defined by

$$L(x; \gamma) = \frac{(\gamma/\pi)}{x^2 + \gamma^2} \tag{4.15}$$

No closed form solution to the Voigt profile exists, however it can be calculated by

$$\phi(x; \sigma, \Gamma) = \frac{Re[w(z)]}{\sigma\sqrt{2\pi}} \tag{4.16}$$

$$z = \frac{x + i\gamma}{\sigma\sqrt{2}} \tag{4.17}$$

where w is the Fadeeva function

$$w(z) = e^{-z^2}\left(1 + \frac{2i}{\sqrt{\pi}}\int_0^z e^{t^2}dt\right) \tag{4.18}$$

In effect, this means that a line can be solved for a known σ, or the standard deviation of the Gaussian component, and γ, the full-width half-max of the Lorentzian component. σ for a distribution of particles in thermodynamic equilibrium can be found as

$$\sigma = \frac{\nu}{c}\sqrt{\frac{2kT}{m}} \tag{4.19}$$

We digress and note that it is somewhat common practice for stellar codes to modify this equation to include a microturbulence parameter ξ as follows

$$\sigma = \frac{\nu}{c}\sqrt{\frac{2kT}{m} + \xi^2} \tag{4.20}$$

We have chosen to neglect this for now. Microturbulence lacks physical motivation and whether or not it improves the accuracy of lines is still in question (see e.g. Asplund, 2005; Kuperus, 2022).

STARDIS may include microturbulence in the future specifically to enable better comparisons to other codes, but are somewhat unsure of its scientific justification.

We now return to our primary task of calculating the Voigt profile to model line profiles. the width of the Lorentzian component of the Voigt profile is given by the summation of three independent components

$$\Gamma = \gamma_{\text{stark}} + \gamma_{\text{vdw}} + \gamma_{\text{Rad}} \tag{4.21}$$

and will be addressed in turn.

The Stark effect describes the splitting of transition lines that are superpositions of transitions between multiple degenerate atomic states into distinct transitions due to the presence of electric fields. Stark broadening is routinely described as an expansion where the linear term describes the leading monopole term and the quadratic term describes the leading dipole term. Neutral H and hydrogenic particles are thus particles in which linear Stark broadening is important, whereas quadratic Stark broadening is important for all other lines. As of now, linear stark broadening is calculated solely for H following Sutton (1978).

$$\gamma_{stark,linear} = a_1 [0.6 * (n_u^2 - n_l^2) N_e^{2/3}] \tag{4.22}$$

where $a_1 = 0.642$ for the first line in a series and 1 otherwise, n_u and n_l are now the principal quantum numbers of the upper and lower states in the transition, and N_e is now the electron number density[4].

For all non-hydrogen lines we calculate Quadratic stark broadening following Gray (2005)

$$log\gamma_4 = 19 + \frac{2}{3}logC_4 + logP_e - \frac{5}{6}logT \tag{4.23}$$

where P_e is the electron pressure following the ideal gas law to get $P_e = n_e kT$. C_4 is calculated following Traving (1960)

---

[4]I would personally like to apologize for the inconsistent variable naming conventions, but I am attempting to stay faithful to source works as well as different field conventions for quantities. From this point on, n refers to the principal quantum number, and N is now a number density.

$$C_4 = \frac{e^2 a_0^3}{36 h \epsilon_0 Z^4} (5 n_{\text{eff},u}^3 + n_{\text{eff},u} - 5 n_{\text{eff},l}^3 - n_{\text{eff},l}) \tag{4.24}$$

In this equation, e is the elementary charge, Z is the ion number, ϵ_0 is the vacuum permittivity of free space, and n_{eff} is the effective principal quantum number given by

$$n_{\text{eff}} = \sqrt{\frac{R_\infty}{E_{ionization} - E_{excitation}} Z} \tag{4.25}$$

where R_∞ is the Rydberg energy constant. The combination of these two equations gives us a description of Stark broadening for each line transition.

Next, we must handle the case of van der Waals broadening, also known as pressure broadening. This effect is a result of intermolecular forces on particles involved in line transitions and in stellar atmospheres is chiefly a result of neutral hydrogen applying attractive and repulsive forces at small distances due to the particle's polarization. Van der Waals broadening is the dominant source of broadening for most lines in dwarf atmospheres. This broadening term scales with the number density of neutral H. STARDIS calculates the van der Waals contribution to the Lorentzian of the Voigt profile following Warner 1967

$$\gamma_{vdw} = 17 \left(\frac{8kT}{\pi m_H} \right)^{0.3} C_6^{0.4} N_H \tag{4.26}$$

where

$$C_6 = 6.46 * 10^{-34} (5 n_{\text{eff},u}^4 + n_{\text{eff},u}^2 - 5 n_{\text{eff},l}^4 - n_{\text{eff},l}^2) \tag{4.27}$$

In these equations, m_H is the mass of H, and N_H is the number density of H.

The last unaccounted for broadening term is radiation broadening, sometimes referred to as natural broadening or damping. This broadening term is a result of the inherent uncertainty in energy of a particle described by the energy-time uncertainty principle. In brief, the uncertainty in energy of the transition is directly related to lifetime of the excited state. The radiation broadening term can be approximated directly as the Einstein A_{ul} coefficient, and is obtained directly from the source of atomic data.

Finally, we have arrived at a complete description of the two parameters needed to determine the shape of any given line. STARDIS calculates Voigt profiles for each line following the numerical approximation of Humlíček 1982. Though testing, we found that this implementation agrees with the `SciPy` (Virtanen et al., 2020) numerical implementation of the Voigt profile with 0.01% and is compatible with Numba (Lam et al., 2015). We describe our implementation scheme more in section 4.5.

4.3.5 Radiative Transfer

With an opacity determined at each depth point throughout the stellar atmosphere at each wavelength, STARDIS is equipped to solve the radiative transfer equation and compute a spectrum. To accomplish this, STARDIS implements a short-characteristic formal scheme for a static medium developed by van Noort et al. (2002). We transcribe the relevant equations here. Specifically, STARDIS solves the equation

$$I_2 = I_1 e^{-\Delta\tau_{1,2}} + w_0 S_2 + w_1 \frac{\partial S}{\partial \tau}\Big|_2 + w_2 \frac{1}{2}\frac{\partial^2 S}{\partial \tau^2}\Big|_2 \tag{4.28}$$

with the weight coefficients given by

$$w_0 = 1 - e^{-\Delta\tau_{1,2}},$$

$$w_1 = w_0 - \Delta\tau_{1,2} e^{-\Delta\tau_{1,2}},$$

$$w_2 = 2w_1 - (\Delta\tau_{1,2})^2 e^{-\Delta\tau_{1,2}},$$

Using the second-order finite difference approximations we have

$$\frac{\partial S}{\partial \tau}\Big|_2 = \frac{(S_2 - S_3)(\Delta\tau_{1,2}/\Delta\tau_{2,3}) - (S_2 - S_1)(\Delta\tau_{2,3}/\Delta\tau_{1,2})}{\Delta\tau_{1,2} + \Delta\tau_{2,3}} \tag{4.29}$$

$$\frac{1}{2}\frac{\partial^2 S}{\partial \tau^2}\Big|_2 = \frac{(S_3 - S_2)/\Delta\tau_{2,3} + (S_1 - S_2)/\Delta\tau_{1,2}}{\Delta\tau_{1,2} + \Delta\tau_{2,3}} \tag{4.30}$$

Currently the source function S is taken to be a blackbody. However, the radiative transfer scheme implemented here is agnostic to the exact source function at any given point and departures

from LTE at this step. The radiative transfer equation is solved at each point for which the stellar model is defined, i.e. the points throughout the atmosphere given by the input model atmosphere. This process is repeated for a number of angles specified by the user, and the weighted average is returned as astrophysical flux throughout the star, to capture the effects of rays emitting across the spherical surface surface of the star. STARDIS solves the equation for n angles specified by the user.

$$F_\nu = \frac{\pi^2}{n} \sum_i^n sin(\theta_i)cos(\theta_i)I_{\nu,i} \tag{4.31}$$

The flux at the outermost point in the simulation (i.e. the surface of the star) is then the final calculated stellar flux, our desired quantity and we have finished our simulation.

4.4 Code Comparison

Here we show a collection of synthesized spectra of STARDIS compared chiefly against those of KORG. We chose these comparisons as our primary metric of validation because we were able to run as similar models as possible between the two codes. STARDIS and KORG are both able to ingest MARCS model atmospheres and calculate line opacities using VALD linelists. We generated spectra with the two codes using the same solar type MARCs atmosphere ($T_{\rm eff} = 5777K$, $logg = 4.40$, [Fe/H] = [α/Fe] = 0.0) and a like VALD linelist. We also show a solar type Phoenix spectrum for reference, but make no direct comparisons to it because the general continuum opacity does not match well. We show four comparisons in Figures 4.2-4.5. Figure 4.5 includes extraterrestrial solar spectrum from Gueymard 2018. Comparisons of other, non-solar type stars are to be included in the final published version of this work.

Often codes disagree significantly on continuum flux, as can be seen when comparing STARDIS or KORG to Phoenix. However, the continuum fluxes are in strong enough agreement between STARDIS and KORG that direct comparisons can be made between the codes and we choose to show the raw synthesized fluxes instead.

Agreement between STARDIS and KORG across wavelengths is good in the optical regime, though the comparisons highlight a small number of missing components. We note the residuals

83

which are sometimes quite large on the individual spectral pixel level, that come from disagreements on the exact shape of specific lines, as can be seen around 6548 Å in Figure 4.2. This disagreement comes from STARDIS analytically calculating the Stark and van der Waals broadening parameters, where KORG ingests these parameters from an external source. Furthermore, KORG handles H lines with a special treatment, using profiles given by Stehlé & Hutcheon 1999. STARDIS instead handles H lines the same as all other chemical species. Agreement between H features in the codes is relatively strong regardless. The largest source of disagreements between the codes is the current lack of molecular lines in STARDIS, easily seen in Figure 4.3 at 5165 Å. Molecular balance calculations are planned future work, but are largely unrelated to elemental abundance measurements that STARDIS is tailored towards. We note that molecules are not present in large enough quantities to impact the chemical balance of elements (and indeed in most spectral synthesis codes are calculated after the atomic chemical balance has been completely solved using this assumption).

Figure 4.5 particularly highlights the strong agreement between the codes in the context of comparing to observational spectra. The figure shows a STARDIS and KORG spectrum compared against each other when convolved to a typical instrumental resolution, $R = 2000$. For typical instrumental spectral resolutions, the codes largely agree at the 1% level or better.

Perhaps the largest omission from STARDIS currently is the lack of appropriate metal bound-free and free-free opacities in the UV. While disagreement between all codes is large in the UV (see e.g., Wheeler et al., 2023), STARDIS clearly and obviously lacks the capability to correctly model this wavelength regime. Inclusion of the relevant opacities should however be completed in the near future.

4.5   Benchmarks

We show a comparison of code run-times in Table 4.1 for two sets of realistic simulations using the same simulation inputs (i.e., linelists and model atmospheres). All testing was done on an AMD EPYC 7552 48-Core Processor on Ubuntu 20.04.6 LTS. STARDIS is significantly slower for most use cases, somewhat unsurprisingly as the code is much younger and less developed, with continued
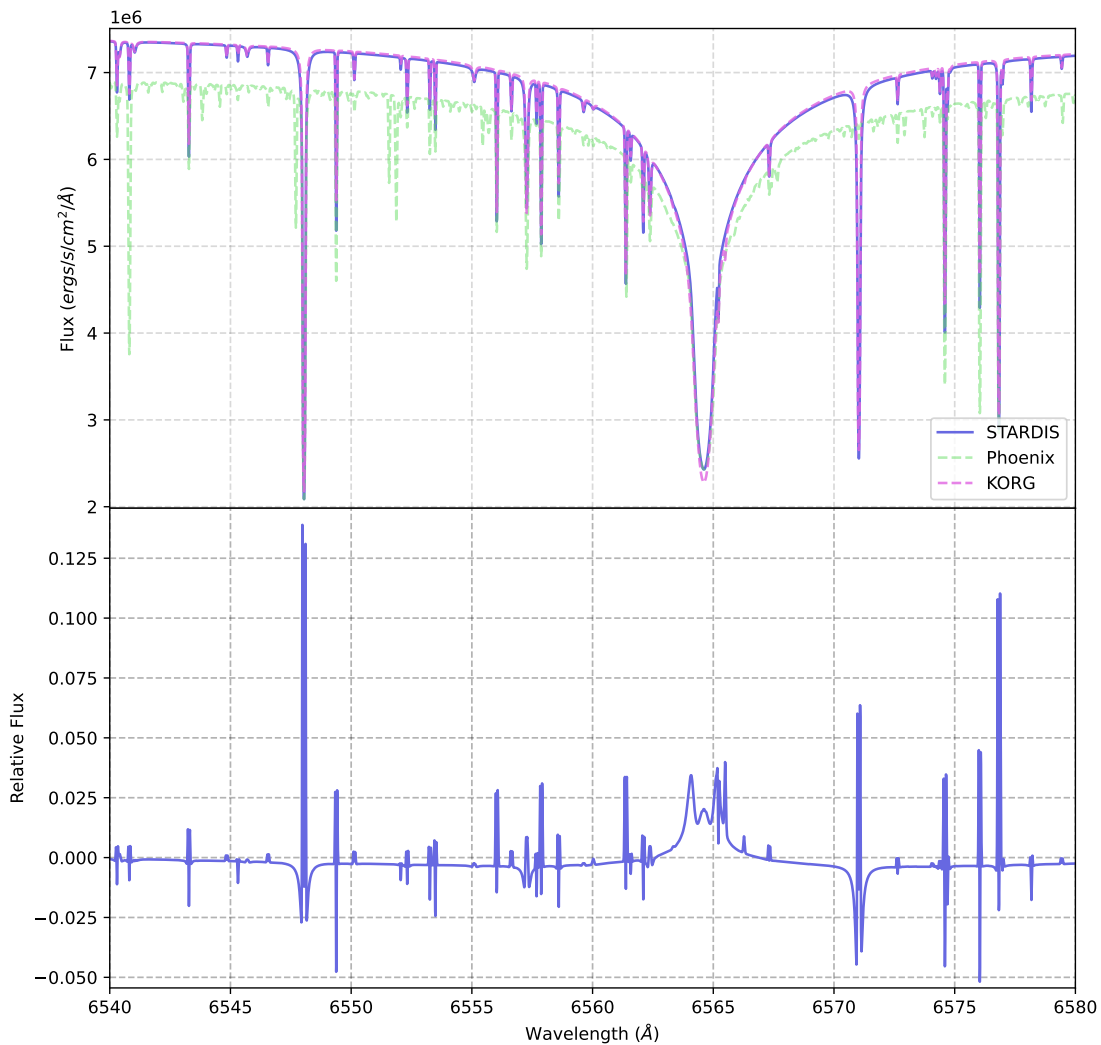
Figure 4.2 A comparison of the spectral output of STARDIS and KORG focusing on the 6563 Å Hα line. The top panel shows the raw fluxes output by STARDIS, KORG, and Phoenix, while the bottom panel shows the percent difference between STARDIS and KORG. Agreement is generally very good, but there are disagreements about exact line shapes.

optimizations as a future goal. However, we do note a few caveats to the numbers listed. First, KORG is primarily written in julia while STARDIS is primarily written in python, with the particularly computationally expensive parts of the code compiled just-in-time with LLVM using Numba (Lam et al., 2015). This means that both codes need to compile for first execution, but KORG's compile
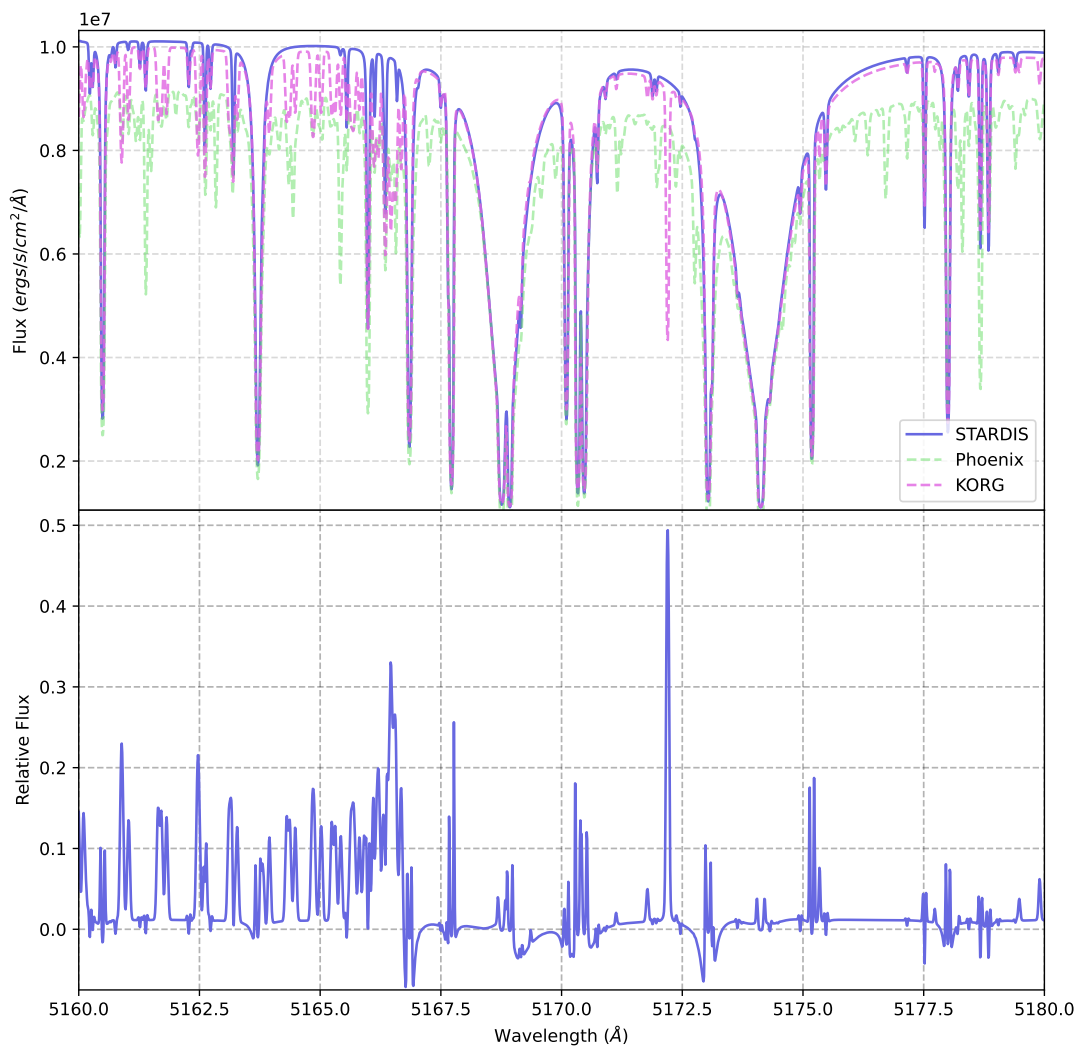
Figure 4.3 Similar to Figure 4.2, but focusing on the 5170 Å Mg triplet. STARDIS currently does not handle molecular lines, which is the major source of disagreement between the codes.

time is about four times as long (~ 5 seconds vs. ~ 20 seconds). Additionaly, STARDIS currently incorporates parallel computation support once again through Numba (Anderson et al., 2017). This particularly helps speed up large simulations in STARDIS.
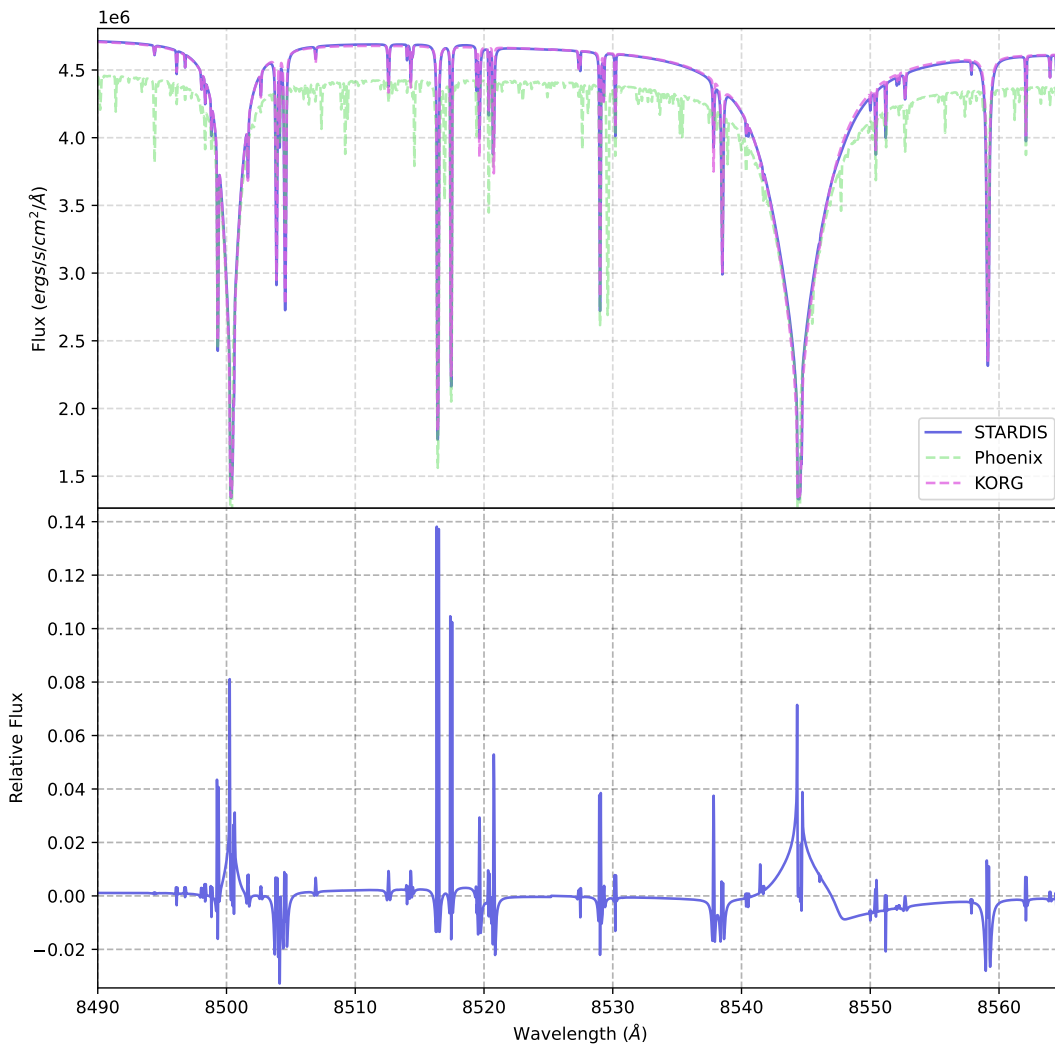
Figure 4.4 Similar to Figure 4.2, but focusing on two of the three Ca II triplet lines near 8500 Å. Once again small disagreements on line shapes exist, but agreement is strong.

4.6 Conclusions and Future Work

We have presented STARDIS, a new 1D stellar spectral synthesis code. This code is written in python to be approachable and expandable by current and upcoming astrophysicists. The code is a part of the expanding and supported TARDIS codebase to encourage long term sustainability and minimize reproduction of shared processes (i.e., physics implementations and numerical solvers

	STARDIS, Serial (s)	STARDIS Parallel, 8 threads (s)	KORG (s)
50 Å Wide	7.6	7.1	0.7
1000 Å Wide	51.1	17.7	1.85

Table 4.1 Compared to KORG, the only other recently developed stellar spectral synthesis code, STARDIS is roughly one order of magnitude slower in most cases. However, we note that all times listed here are post-compile times. STARDIS has a flat compile time of roughly 5 seconds, while KORG's compile time is close to 22 seconds in our testing. This makes STARDIS marginally faster to compute a first spectrum for many cases, but slower in most other cases.

written for one package can be applied to the other with minimal changes). STARDIS is entirely open-source and can be found at https://github.com/tardis-sn/stardis. Documentation, including installation and usage tutorials can be found at https://tardis-sn.github.io/stardis/.

STARDIS is built with modularity in mind, to be able to accurately model a wide variety of stellar that require different physics and approximations systems as needed. It is currently the only stellar spectral synthesis code known to the authors capable of directly ingesting MESA atmospheres. We advise caution when using STARDIS to model MESA atmospheres as we have yet to comprehensively validate MESA models against known outputs, however we believe that the tool should enable scientists interested in unique systems to make new insights that were not yet possible. Furthermore, models can be tweaked at the python object level to give the user as much flexibility as possible. This idea extends to the atomic data as well, being linked to the `Carsus` atomic data ingestion package within the TARDIS codebase to allow for as flexible atomic data inputs as possible.

Currently STARDIS has only been strongly validated on solar analogues. However, preliminary results are encouraging, and STARDIS is currently able to produce spectra of sufficient accuracy to constrain stellar astrophysical parameters and chemical abundances. The implementation of metal continuum opacities will allow for accurate spectral comparisons in the UV. Additionally, development of NLTE detailed chemical abundance calculations and a relaxation of the blackbody source function should be available in the near future.

In the long term, we intend STARDIS to be as approachable as possible without compromising on efficiency or precision. In addition to the planned and in progress extensions to the physical

and computational aspects of the code, we are currently producing comprehensive tutorials to showcase the various physics and computation schemes implemented in STARDIS. It is our hope that this code will provide a suitable tool to study the physical systems that current astrophysicists are interested in, and that the approachability of the code will allow for more efficient research for years to come.
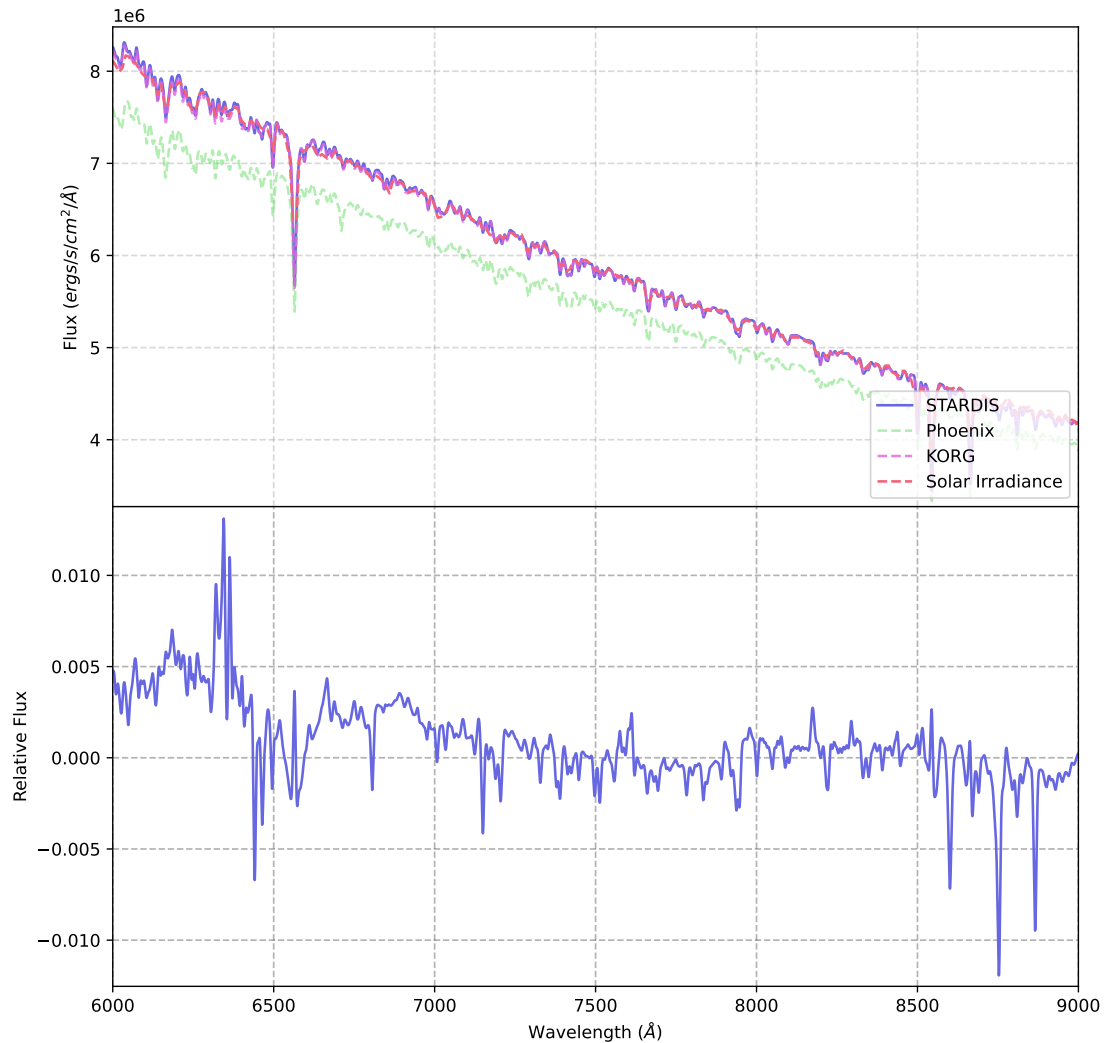
Figure 4.5 A large scale comparison of STARDIS, KORG, PHOENIX, convolved to a spectral resolution R of 2000. For reference, NIRSpec has a spectral resolution R between 100 and 2700. Agreement between the codes on large scales is generally better 0.5% on resolvable scales. There is some disagreement near the Ca triplet past 8500 Å, generally below 1%. A solar spectrum with similar spectral resolution is plotted for reference.

CHAPTER 5

SUMMARY AND FUTURE WORK

The overarching goal of this work is to use stars as probes of SN Ia progenitor systems, as well as to develop a tool that will enable and expedite future investigations of stellar properties and whatever deeper physical questions those investigations attack. In this final chapter, I will briefly summarize each of the scientific projects presented in this work in the order in which they appeared. Then, I will conclude in section 5.2 by describing future work and research directions.

5.1 Summary of Dissertation Work

5.1.1 Chapter 2, Searching for a Hypervelocity White Dwarf SN Ia Companion: A Proper Motion Survey of SN 1006

In Chapter 2 my coauthors and I investigated the interior stellar population to the SN 1006 remnant to try to identify a hypervelocity white dwarf as predicted by the Shen & Schwab 2017 conceptualization of the D6 SN Ia progenitor scenario. Previous surviving companion searches of the remnant did not explore a wide enough search area to allow for the extraordinarily high proper motions inherited by surviving companions in this scenario, greater than 1000 km s^{-1}. The discovery of such an object would immediately provide a massive step forward towards addressing the SN Ia progenitor problem, one of the primary concerns of this thesis. The non-existence of such an object in the remnant would alternatively provide strong evidence against the scenario as a generic explanation for normal SNe Ia.

In order to conclusively rule out surviving D6 companion, we needed to investigate the entire portion of the sky contained by a star moving greater than 1000 km s^{-1} for about 1000 yrs, the age of the SN 1006 remnant (see Figure 2.2). In such a large search region with so many contained stars, the only currently conceivable way to search for such a companion is to search through the contained stellar population using large-scale data science methodologies. We investigated this portion of the sky by systematically measuring the proper motions of each star in the region with high-precision astrometry performed on photometry from DECam on the on the Victor M. Blanco 4-meter Telescope. The results of that survey are shown in Figre 2.5. We did not find a star

with such an anomalously high proper motion as predicted by the scenario and concluded that the remnant must not have been created by the Shen & Schwab 2017 conceptualization of the D6 scenario.

5.1.2 Chapter 3, No Surviving SN Ia Companion in SNR 0509-67.5: Stellar Population Characterization and Comparison to Models

In Chapter 3 my coauthors and I turned our sights towards the $0509-67.5$ remnant in the LMC. While this remnant had been previously studied in Schaefer & Pagnotta 2012, the parameter space examined and ruled out by that work was not sufficient to conclusively say that no surviving SN Ia companion exists in the remnant when considering the decade of further theoretical work since the date of that study (i.e., surviving companions have been suggested since 2012 which have not been ruled out by that work). In this chapter of my thesis, we investigated SNR $0509-67.5$ by combining a several independent archival HST observations of the remnant taken over the years to build an SED for each star within the remnant. Using the distance of the LMC as a strong prior on the distance to each star, we modeled the SEDs of the stars to derive temperatures and radii for each (see Figure 3.3 for the stellar population). We gathered any prediction on the expected appearance of a surviving companion within 1000 yrs after the SN explosion and compared the predicted parameters to each of the stars within the remnant.

We did not detect a surviving companion within the remnant in line with the predictions of any theoretical surviving companion put forth in the literature. In effect, we ruled out the existence of a surviving companion within the remnant, and in turn ruled out each SN Ia progenitor scenario that would leave a surviving companion (with the exception of the spin up/spin down scenario, which would leave a companion too small to detect, or be relatively unperturbed and thus difficult to distinguish against the unrelated stellar population). Additionally, we showed the full distribution of constrained temperatures and radii of the interior stellar population to allow surviving companion predictions not considered in the work or not yet developed to be directly compared to those stars (see Figure 3.6).

92

5.1.3 Chapter 4, STARDIS: a Modern Stellar Spectral Synthesis Code

Chapter 4 details the release of the new STARDIS code, which has served as the final project of my thesis. The chapter begins with a justification for the the comprised work and need of the community for a new stellar spectral synthesis code. The chapter includes a review of the physics necessary to accurately perform radiative transfer in a stellar atmosphere, and describes the computation done by STARDIS to create the synthetic stellar spectrum. It also details the structure of and the assumptions made by the code. Finally, the chapter provides code comparisons to test the validity of the code, and benchmarks to evaluate the computational expediency of the code.

While this work does not immediately contribute to solving the SN Ia progenitor problem, it is my hope that STARDIS will enable more sophisticated and detailed modeling of theoretical SN Ia progenitors in the future, as well as more accurate chemical abundance measurements which have been shown to potentially be a lasting signature on the surface of a surviving companion. Furthermore, I hope that this code will be used to enable new physical investigation of stars across astrophysics, in sub-fields that I know next to nothing about. Much of the research in this thesis was built upon and only possible through the existence of astrophysics software. I can only hope that STARDIS will be of similar use to future astrophysicists.

5.2 Ongoing and Future Work

First and foremost, the official science release of the STARDIS code is expected soon after this thesis. While there is very little code development necessary before release, a more comprehensive validation of the code with a larger suite of inputs is planned.

Next, as detailed extensively in Chapter 4, the STARDIS code, has a host of planned future developments to extend functionality and ease of use. NLTE detailed chemical balance calculations should allow for more accurate measurements of chemical abundances in stellar atmospheres. NLTE population calculations of any given element in any given stellar atmosphere may not dramatically affect the ionization and level populations that are ultimately responsible for absorption and emission features in stellar spectra, but it is impossible to tell which features are affected, and by how much the answer changes, until the detailed calculation is performed. The implementation of NLTE

detailed balance calculations in STARDIS is currently underway. This development will be even more important in the modelling of hot, massive stars. Additionally, hot, massive stars usually show chemical features formed in extended stellar winds. To correctly reproduce these spectra, we plan to extend STARDIS to accurately handle wind profiles. On the low mass side, the largest current remaining obstacle in accurately modeling these stars is the formation of molecules in the stellar atmosphere and subsequent opacity calculations. We plan to add molecular balance equations to STARDIS to be able to accurately model low mass stellar spectra.

To refocus briefly on the topic of the SN Ia progenitor problem, in defiance of the work presented in this thesis, the progenitor problem remains unsolved. However, we have a number of clear avenues of investigation that will continue making progress towards unraveling the problem. I plan to repeat the methodology of Chapter 3 to search for surviving companions in a handful of other LMC SN Ia remnants. That investigation purely made use of public archival HST observations of historical remnants. There already exists similar, though perhaps somewhat less comprehensive, observations of over four other LMC remnants. Our investigation of SNR 0509−67.5 is the most comprehensive surviving companion remnant search to date. Repeating that study on a larger sample of remnants would either finally confirm a surviving companion, or build towards a robust statistically significant sample of non-detections that would suggest SNe Ia generically do not produce surviving companions. One way or another, this future study will make definitive headway into confirming and rejecting SN Ia progenitor scenarios.

BIBLIOGRAPHY

Anderson, T. A., Liu, H., Kuper, L., et al. 2017

Arnett, W. D. 1982, The Astrophysical Journal, 253, 785, doi: `10.1086/159681`

Arunachalam, P., Hughes, J. P., Hovey, L., & Eriksen, K. 2022, The Astrophysical Journal, 938, 121, doi: `10.3847/1538-4357/ac927c`

Asplund, M. 2005, Annual Review of Astronomy and Astrophysics, 43, 481, doi: `10.1146/annurev.astro.42.053102.134001`

Axelrod, T. S. 1980, PhD thesis. `https://ui.adsabs.harvard.edu/abs/1980PhDT.......1A`

Baron, E., Chen, B., & Hauschildt, P. H. 2010, Astrophysics Source Code Library, ascl:1010.056. `https://ui.adsabs.harvard.edu/abs/2010ascl.soft10056B`

Bell, K. L., & Berrington, K. A. 1987, Journal of Physics B Atomic Molecular Physics, 20, 801, doi: `10.1088/0022-3700/20/4/019`

Bertin, E., Mellier, Y., Radovich, M., et al. 2002, 281, 228. `https://ui.adsabs.harvard.edu/abs/2002ASPC..281..228B`

Bianco, F. B., Howell, D. A., Sullivan, M., et al. 2011, The Astrophysical Journal, 741, 20, doi: `10.1088/0004-637X/741/1/20`

Bildsten, L., Shen, K. J., Weinberg, N. N., & Nelemans, G. 2007, The Astrophysical Journal, 662, L95, doi: `10.1086/519489`

Blondin, S., Dessart, L., Hillier, D. J., & Khokhlov, A. M. 2017, Monthly Notices of the Royal Astronomical Society, 470, 157, doi: `10.1093/mnras/stw2492`

Bloom, J. S., Kasen, D., Shen, K. J., et al. 2012, The Astrophysical Journal, 744, L17, doi: `10.1088/2041-8205/744/2/L17`

Brown, W. R. 2015, Annual Review of Astronomy and Astrophysics, 53, 15, doi: `10.1146/annurev-astro-082214-122230`

Buchner, J. 2016, Statistics and Computing, 26, 383, doi: `10.1007/s11222-014-9512-y`

—. 2019, Publications of the Astronomical Society of the Pacific, 131, 108005, doi: `10.1088/1538-3873/aae7fc`

—. 2021, UltraNest – a robust, general purpose Bayesian inference engine, arXiv, doi: `10.48550/`

arXiv.2101.09604

Bulla, M., Sim, S. A., Pakmor, R., et al. 2016a, Monthly Notices of the Royal Astronomical Society, 455, 1060, doi: `10.1093/mnras/stv2402`

Bulla, M., Sim, S. A., Kromer, M., et al. 2016b, Monthly Notices of the Royal Astronomical Society, 462, 1039, doi: `10.1093/mnras/stw1733`

Capak; Peter. 2019, Spitzer enhanced imaging products (SEIP) source list, IPAC, doi: `10.26131/IRSA3`

Cartier, R., Sullivan, M., Firth, R. E., et al. 2017, Monthly Notices of the Royal Astronomical Society, 464, 4476, doi: `10.1093/mnras/stw2678`

Chandrasekhar, S. 1931, The Astrophysical Journal, 74, 81, doi: `10.1086/143324`

Chiosi, E., Chiosi, C., Trevisan, P., Piovan, L., & Orio, M. 2015, Monthly Notices of the Royal Astronomical Society, 448, 2100, doi: `10.1093/mnras/stv084`

Choi, Y., Nidever, D. L., Olsen, K., et al. 2018, The Astrophysical Journal, 866, 90, doi: `10.3847/1538-4357/aae083`

Colgan, J., Kilcrease, D. P., Magee, N. H., et al. 2016, The Astrophysical Journal, 817, 116, doi: `10.3847/0004-637X/817/2/116`

Colgate, S. A., & McKee, C. 1969, The Astrophysical Journal, 157, 623, doi: `10.1086/150102`

Collaboration, G., Prusti, T., de Bruijne, J. H. J., et al. 2016, Astronomy and Astrophysics, 595, A1, doi: `10.1051/0004-6361/201629272`

Collaboration, G., Brown, A. G. A., Vallenari, A., et al. 2018, Astronomy and Astrophysics, 616, A1, doi: `10.1051/0004-6361/201833051`

Dan, M., Rosswog, S., Guillochon, J., & Ramirez-Ruiz, E. 2011, The Astrophysical Journal, 737, 89, doi: `10.1088/0004-637X/737/2/89`

Dekel, A., & Silk, J. 1986, The Astrophysical Journal, 303, 39, doi: `10.1086/164050`

Di Stefano, R., & Kilic, M. 2012, The Astrophysical Journal, 759, 56, doi: `10.1088/0004-637X/759/1/56`

Di Stefano, R., Voss, R., & Claeys, J. S. W. 2011, The Astrophysical Journal, 738, L1, doi: `10.1088/2041-8205/738/1/L1`

Diehl, T. 2012, Physics Procedia, 37, 1332, doi: `10.1016/j.phpro.2012.02.472`

Fausnaugh, M. M., Vallely, P. J., Kochanek, C. S., et al. 2021, The Astrophysical Journal, 908, 51, doi: `10.3847/1538-4357/abcd42`

Fazio, G. G., Hora, J. L., Allen, L. E., et al. 2004, The Astrophysical Journal Supplement Series, 154, 10, doi: `10.1086/422843`

Fitzpatrick, E. L. 1999, Publications of the Astronomical Society of the Pacific, 111, 63, doi: `10.1086/316293`

Flaugher, B., Diehl, H. T., Honscheid, K., et al. 2015, The Astronomical Journal, 150, 150, doi: `10.1088/0004-6256/150/5/150`

Gaia Collaboration, Brown, A. G. A., Vallenari, A., et al. 2021, Astronomy & Astrophysics, 649, A1, doi: `10.1051/0004-6361/202039657`

Generozov, A., & Perets, H. B. 2022, Monthly Notices of the Royal Astronomical Society, doi: `10.1093/mnras/stac1108`

Gilfanov, M., & Bogdán, A. 2010, Nature, 463, 924, doi: `10.1038/nature08685`

Graham, M. L., Kumar, S., Hosseinzadeh, G., et al. 2017, Monthly Notices of the Royal Astronomical Society, 472, 3437, doi: `10.1093/mnras/stx2224`

Gray, D. F. 2005, The Observation and Analysis of Stellar Photospheres, 3rd edn. (Cambridge: Cambridge University Press), doi: `10.1017/CBO9781316036570`

Gray, R. O., & Corbally, C. J. 1994, The Astronomical Journal, 107, 742, doi: `10.1086/116893`

Green, D. A. 2019, Journal of Astrophysics and Astronomy, 40, 36, doi: `10.1007/s12036-019-9601-6`

Guest, B. T., Borkowski, K. J., Ghavamian, P., et al. 2023, The Astrophysical Journal, 946, 44, doi: `10.3847/1538-4357/acbf4e`

Gueymard, C. A. 2018, Solar Energy, 169, 434, doi: `10.1016/j.solener.2018.04.067`

Guillochon, J., Dan, M., Ramirez-Ruiz, E., & Rosswog, S. 2010, The Astrophysical Journal, 709, L64, doi: `10.1088/2041-8205/709/1/L64`

Guo, H. L., Chen, B. Q., Yuan, H. B., et al. 2021, The Astrophysical Journal, 906, 47, doi: `10.3847/1538-4357/abc68a`

Gustafsson, B., Edvardsson, B., Eriksson, K., et al. 2008, Astronomy and Astrophysics, 486, 951, doi: `10.1051/0004-6361:200809724`

Hachisu, I., Kato, M., & Nomoto, K. 1999, The Astrophysical Journal, 522, 487, doi: `10.1086/307608`

Hachisu, I., Kato, M., Saio, H., & Nomoto, K. 2012, The Astrophysical Journal, 744, 69, doi: `10.1088/0004-637X/744/1/69`

Han, Z. 2008, The Astrophysical Journal, 677, L109, doi: `10.1086/588191`

Han, Z., & Podsiadlowski, P. 2004, Monthly Notices of the Royal Astronomical Society, 350, 1301, doi: `10.1111/j.1365-2966.2004.07713.x`

Hayden, B. T., Garnavich, P. M., Kessler, R., et al. 2010, The Astrophysical Journal, 712, 350, doi: `10.1088/0004-637X/712/1/350`

Hernandez, J. I. G., Ruiz-Lapuente, P., Tabernero, H. M., et al. 2012, doi: `10.1038/nature11447`

Hernández, J. I. G., Ruiz-Lapuente, P., Filippenko, A. V., et al. 2009, The Astrophysical Journal, 691, 1, doi: `10.1088/0004-637X/691/1/1`

Hillebrandt, W., & Niemeyer, J. C. 2000, Annual Review of Astronomy and Astrophysics, 38, 191, doi: `10.1146/annurev.astro.38.1.191`

Hills, J. G. 1988, Nature, 331, 687, doi: `10.1038/331687a0`

Hoeflich, P., & Khokhlov, A. 1996, The Astrophysical Journal, 457, 500, doi: `10.1086/176748`

Hoeflich, P., Khokhlov, A., Wheeler, J. C., et al. 1996, The Astrophysical Journal, 472, L81, doi: `10.1086/310363`

Hoeflich, P., Hsiao, E. Y., Ashall, C., et al. 2017, The Astrophysical Journal, 846, 58, doi: `10.3847/1538-4357/aa84b2`

Hoffmann, S. L., Mack, J., Avila, R., et al. 2021, 53, 216.02. `https://ui.adsabs.harvard.edu/abs/2021AAS...23821602H`

Holmbo, S., Stritzinger, M. D., Shappee, B. J., et al. 2019, Astronomy & Astrophysics, 627, A174, doi: `10.1051/0004-6361/201834389`

Hovey, L. 2016, PhD thesis. `https://ui.adsabs.harvard.edu/abs/2016PhDT........21H`

Hoyle, F., & Fowler, W. A. 1960, The Astrophysical Journal, 132, 565, doi: `10.1086/146963`

Hubeny, I., & Lanz, T. 2011, Astrophysics Source Code Library, ascl:1109.022. `https://ui.adsabs.harvard.edu/abs/2011ascl.soft09022H`

Hubeny, I., & Mihalas, D. 2014, Theory of Stellar Atmospheres. `https://ui.adsabs.harvard.edu/abs/2014tsa..book.....H`

Humlíček, J. 1982, Journal of Quantitative Spectroscopy and Radiative Transfer, 27, 437, doi: `10.1016/0022-4073(82)90078-4`

Husser, T.-O., Wende-von Berg, S., Dreizler, S., et al. 2013, Astronomy & Astrophysics, 553, A6, doi: `10.1051/0004-6361/201219058`

Iben, Jr., I., Nomoto, K., Tornambe, A., & Tutukov, A. V. 1987, The Astrophysical Journal, 317, 717, doi: `10.1086/165318`

Iben, Jr., I., & Renzini, A. 1983, Annual Review of Astronomy and Astrophysics, 21, 271, doi: `10.1146/annurev.aa.21.090183.001415`

Iben, Jr., I., & Tutukov, A. V. 1984, The Astrophysical Journal Supplement Series, 54, 335, doi: `10.1086/190932`

—. 1994, The Astrophysical Journal, 431, 264, doi: `10.1086/174484`

Ihara, Y., Ozaki, J., Doi, M., et al. 2007, Publications of the Astronomical Society of Japan, 59, 811, doi: `10.1093/pasj/59.4.811`

Jermyn, A. S., Bauer, E. B., Schwab, J., et al. 2023, 265, 15, doi: `10.3847/1538-4365/acae8d`

Joshi, Y. C., & Panchal, A. 2019, Astronomy & Astrophysics, 628, A51, doi: `10.1051/0004-6361/201834574`

Justham, S. 2011, The Astrophysical Journal, 730, L34, doi: `10.1088/2041-8205/730/2/L34`

Kerzendorf, W., & Do, T. 2015, Zenodo, doi: `10.5281/zenodo.28016`

Kerzendorf, W., & Singhal, J. 2022, Astrophysics Source Code Library, ascl:2209.013. `https://ui.adsabs.harvard.edu/abs/2022ascl.soft09013K`

Kerzendorf, W. E., Childress, M., Scharwächter, J., Do, T., & Schmidt, B. P. 2014, \apj, 782, 27, doi: `10.1088/0004-637X/782/1/27`

Kerzendorf, W. E., Long, K. S., Winkler, P. F., & Do, T. 2018a, \mnras, 479, 5696, doi: `10.1093/mnras/sty1863`

Kerzendorf, W. E., Schmidt, B. P., Asplund, M., et al. 2009, The Astrophysical Journal, 701, 1665, doi: `10.1088/0004-637X/701/2/1665`

Kerzendorf, W. E., Schmidt, B. P., Laird, J. B., Podsiadlowski, P., & Bessell, M. S. 2012, The

Astrophysical Journal, 759, 7, doi: `10.1088/0004-637X/759/1/7`

Kerzendorf, W. E., & Sim, S. A. 2014, Monthly Notices of the Royal Astronomical Society, 440, 387, doi: `10.1093/mnras/stu055`

Kerzendorf, W. E., Strampelli, G., Shen, K. J., et al. 2018b, Monthly Notices of the Royal Astronomical Society, 479, 192, doi: `10.1093/mnras/sty1357`

Kerzendorf, W. E., Yong, D., Schmidt, B. P., et al. 2013, \apj, 774, 99, doi: `10.1088/0004-637X/774/2/99`

Kobayashi, C., Leung, S.-C., & Nomoto, K. 2020, The Astrophysical Journal, 895, 138, doi: `10.3847/1538-4357/ab8e44`

Kuperus, I. 2022, Master's thesis. `https://www.duo.uio.no/handle/10852/96749`

Kupka, F., Piskunov, N., Ryabchikova, T. A., Stempels, H. C., & Weiss, W. W. 1999, Astronomy and Astrophysics Supplement Series, 138, 119, doi: `10.1051/aas:1999267`

Kupka, F. G., Ryabchikova, T. A., Piskunov, N. E., Stempels, H. C., & Weiss, W. W. 2000, Baltic Astronomy, 9, 590, doi: `10.1515/astro-2000-0420`

Kurucz, R. 1993, Robert Kurucz CD-ROM, 18. `https://ui.adsabs.harvard.edu/abs/1993KurCD..18.....K`

Lam, S. K., Pitrou, A., & Seibert, S. 2015, in Proceedings of the Second Workshop on the LLVM Compiler Infrastructure in HPC, LLVM '15 (New York, NY, USA: Association for Computing Machinery), 1–6, doi: `10.1145/2833157.2833162`

Leonard, D. C. 2007, The Astrophysical Journal, 670, 1275, doi: `10.1086/522367`

Li, C.-J., Kerzendorf, W. E., Chu, Y.-H., et al. 2019, The Astrophysical Journal, 886, 99, doi: `10.3847/1538-4357/ab4a03`

Li, X.-D., & van den Heuvel, E. P. J. 1997, Astronomy and Astrophysics, v.322, p.L9-L12, 322, L9. `https://ui.adsabs.harvard.edu/abs/1997A%26A...322L...9L/abstract`

Litke, K. C., Chu, Y.-H., Holmes, A., et al. 2017, The Astrophysical Journal, 837, 111, doi: `10.3847/1538-4357/aa5d57`

Liu, Z.-W., Roepke, F. K., Zeng, Y., & Heger, A. 2021, Astronomy & Astrophysics, 654, A103, doi: `10.1051/0004-6361/202141518`

Liu, Z.-W., Röpke, F. K., & Han, Z. 2023, Research in Astronomy and Astrophysics, 23, 082001, doi: `10.1088/1674-4527/acd89e`

Liu, Z.-W., Röpke, F. K., & Zeng, Y. 2022, The Astrophysical Journal, 928, 146, doi: `10.3847/1538-4357/ac5517`

Livio, M. 2000, The Progenitors of Type Ia Supernovae (eprint: arXiv:astro-ph/9903264). `https://ui.adsabs.harvard.edu/abs/2000tias.conf...33L`

Livio, M., & Mazzali, P. 2018, Physics Reports, 736, 1, doi: `10.1016/j.physrep.2018.02.002`

Livne, E. 1990, The Astrophysical Journal, 354, L53, doi: `10.1086/185721`

Luck, R. E., Moffett, T. J., Iii, T. G. B., & Gieren, W. P. 1998, The Astronomical Journal, 115, 605, doi: `10.1086/300227`

Lundqvist, P., Mattila, S., Sollerman, J., et al. 2013, Monthly Notices of the Royal Astronomical Society, 435, 329, doi: `10.1093/mnras/stt1303`

Lundqvist, P., Nyholm, A., Taddia, F., et al. 2015, Astronomy & Astrophysics, Volume 577, id.A39, <NUMPAGES>12</NUMPAGES> pp., 577, A39, doi: `10.1051/0004-6361/201525719`

Maeda, K., & Terada, Y. 2016, International Journal of Modern Physics D, 25, 1630024, doi: `10.1142/S021827181630024X`

Maguire, K., Taubenberger, S., Sullivan, M., & Mazzali, P. A. 2016, Monthly Notices of the Royal Astronomical Society, 457, 3254, doi: `10.1093/mnras/stv2991`

Mannucci, F., Della Valle, M., & Panagia, N. 2006, Monthly Notices of the Royal Astronomical Society, 370, 773, doi: `10.1111/j.1365-2966.2006.10501.x`

Maoz, D., Mannucci, F., & Nelemans, G. 2014, Annual Review of Astronomy and Astrophysics, 52, 107, doi: `10.1146/annurev-astro-082812-141031`

Marietta, E., Burrows, A., & Fryxell, B. 2000, \apjs, 128, 615, doi: `10.1086/313392`

Marion, G. H., Brown, P. J., Vinkó, J., et al. 2016, The Astrophysical Journal, 820, 92, doi: `10.3847/0004-637X/820/2/92`

Martínez-Rodríguez, H., Lopez, L. A., Auchettl, K., et al. 2020, Evidence of a Type Ia Progenitor for Supernova Remnant 3C 397, doi: `10.48550/arXiv.2006.08681`

Mattila, S., Lundqvist, P., Sollerman, J., et al. 2005, Astronomy and Astrophysics, 443, 649, doi: `10.1051/0004-6361:20052731`

Mazzali, P. A., Nomoto, K., Cappellaro, E., et al. 2001, The Astrophysical Journal, 547, 988, doi: `10.1086/318428`

Meng, X., Chen, X., & Han, Z. 2009, Monthly Notices of the Royal Astronomical Society, 395, 2103, doi: 10.1111/j.1365-2966.2009.14636.x

Meng, X., & Li, J. 2019, Monthly Notices of the Royal Astronomical Society, 482, 5651, doi: 10.1093/mnras/sty3092

Meng, X., & Podsiadlowski, P. 2013, The Astrophysical Journal, 778, L35, doi: 10.1088/2041-8205/778/2/L35

Meyerott, R. E. 1978, The Astrophysical Journal, 221, 975, doi: 10.1086/156103

—. 1980, The Astrophysical Journal, 239, 257, doi: 10.1086/158106

Miller, A. A., Cao, Y., Piro, A. L., et al. 2018, The Astrophysical Journal, 852, 100, doi: 10.3847/1538-4357/aaa01f

Mitra, S., Davé, R., & Finlator, K. 2015, Monthly Notices of the Royal Astronomical Society, 452, 1184, doi: 10.1093/mnras/stv1387

Nomoto, K. 1982a, \apj, 253, 798, doi: 10.1086/159682

—. 1982b, \apj, 257, 780, doi: 10.1086/160031

Nomoto, K., & Iben, Jr., I. 1985, The Astrophysical Journal, 297, 531, doi: 10.1086/163547

Nomoto, K., Kobayashi, C., & Tominaga, N. 2013, Annual Review of Astronomy and Astrophysics, 51, 457, doi: 10.1146/annurev-astro-082812-140956

Nomoto, K., & Kondo, Y. 1991, The Astrophysical Journal, 367, L19, doi: 10.1086/185922

Nomoto, K., & Sugimoto, D. 1977, Publications of the Astronomical Society of Japan, 29, 765. https://ui.adsabs.harvard.edu/abs/1977PASJ...29..765N

Nomoto, K., Thielemann, F. K., & Wheeler, J. C. 1984, The Astrophysical Journal, 279, L23, doi: 10.1086/184247

O'Brien, J. T., Kerzendorf, W. E., Fullard, A., et al. 2021, The Astrophysical Journal, 916, L14, doi: 10.3847/2041-8213/ac1173

—. 2024, The Astrophysical Journal, 964, 137, doi: 10.3847/1538-4357/ad2358

Olling, R. P., Mushotzky, R., Shaya, E. J., et al. 2015, Nature, 521, 332, doi: 10.1038/nature14455

Ozaki, J., & Shigeyama, T. 2006, The Astrophysical Journal, 644, 954, doi: 10.1086/503737

Pakhomov, Y. V., & Ryabchikova, T. A. 2019, INASAN Science Reports, 4, 79, doi: `10.26087/INASAN.2019.4.2.014`

Pakmor, R., Kromer, M., Röpke, F. K., et al. 2010, Nature, 463, 61, doi: `10.1038/nature08642`

Pakmor, R., Kromer, M., Taubenberger, S., et al. 2012, The Astrophysical Journal, 747, L10, doi: `10.1088/2041-8205/747/1/L10`

Pakmor, R., Kromer, M., Taubenberger, S., & Springel, V. 2013, The Astrophysical Journal, 770, L8, doi: `10.1088/2041-8205/770/1/L8`

Pakmor, R., Roepke, F. K., Weiss, A., & Hillebrandt, W. 2008, Astronomy & Astrophysics, 489, 943, doi: `10.1051/0004-6361:200810456`

Pakmor, R., Zenati, Y., Perets, H. B., & Toonen, S. 2021, Monthly Notices of the Royal Astronomical Society, 503, 4734, doi: `10.1093/mnras/stab686`

Pakmor, R., Callan, F. P., Collins, C. E., et al. 2022, On the fate of the secondary white dwarf in double-degenerate double-detonation Type Ia supernovae, Tech. rep. `https://ui.adsabs.harvard.edu/abs/2022arXiv220314990P`

Pan, K.-C., Ricker, P. M., & Taam, R. E. 2012, \apj, 750, 151, doi: `10.1088/0004-637X/750/2/151`

—. 2013, \apj, 773, 49, doi: `10.1088/0004-637X/773/1/49`

—. 2014, \apj, 792, 71, doi: `10.1088/0004-637X/792/1/71`

Pankey, Jr., T. 1962, PhD thesis. `https://ui.adsabs.harvard.edu/abs/1962PhDT.......25P`

Papish, O., Soker, N., García-Berro, E., & Aznar-Siguán, G. 2015, \mnras, 449, 942, doi: `10.1093/mnras/stv337`

Paxton, B., Bildsten, L., Dotter, A., et al. 2011, 192, 3, doi: `10.1088/0067-0049/192/1/3`

Paxton, B., Cantiello, M., Arras, P., et al. 2013, 208, 4, doi: `10.1088/0067-0049/208/1/4`

Paxton, B., Marchant, P., Schwab, J., et al. 2015, 220, 15, doi: `10.1088/0067-0049/220/1/15`

Paxton, B., Schwab, J., Bauer, E. B., et al. 2018, 234, 34, doi: `10.3847/1538-4365/aaa5a8`

Paxton, B., Smolec, R., Schwab, J., et al. 2019, 243, 10, doi: `10.3847/1538-4365/ab2241`

Perlmutter, S., Aldering, G., Goldhaber, G., et al. 1999, The Astrophysical Journal, 517, 565,

doi: `10.1086/307221`

Phillips, M. M. 1993, The Astrophysical Journal, 413, L105, doi: `10.1086/186970`

Phillips, M. M., Lira, P., Suntzeff, N. B., et al. 1999, The Astronomical Journal, 118, 1766, doi: `10.1086/301032`

Pietrzyński, G., Graczyk, D., Gallenne, A., et al. 2019, Nature, 567, 200, doi: `10.1038/s41586-019-0999-4`

Piskunov, N. E., Kupka, F., Ryabchikova, T. A., Weiss, W. W., & Jeffery, C. S. 1995, Astronomy and Astrophysics Supplement Series, 112, 525. `https://ui.adsabs.harvard.edu/abs/1995A&AS..112..525P`

Plez, B. 2012, Astrophysics Source Code Library, ascl:1205.004. `https://ui.adsabs.harvard.edu/abs/2012ascl.soft05004P`

Pássaro, E. A., E., K. W., A., F., & C., V. 2020, An open source framework for atomic data, Zenodo, doi: `10.5281/zenodo.4062427`

Raskin, C., Scannapieco, E., Rockefeller, G., et al. 2010, The Astrophysical Journal, 724, 111, doi: `10.1088/0004-637X/724/1/111`

Rau, S.-J., & Pan, K.-C. 2022, Evolution of Main-Sequence-like Surviving Companions in Type Ia Supernova Remnants, Tech. Rep. arXiv:2205.13670, arXiv. `http://arxiv.org/abs/2205.13670`

Rebassa-Mansergas, A., Toonen, S., Korol, V., & Torres, S. 2019, Monthly Notices of the Royal Astronomical Society, 482, 3656, doi: `10.1093/mnras/sty2965`

Rest, A., Suntzeff, N. B., Olsen, K., et al. 2005a, Nature, 438, 1132, doi: `10.1038/nature04365`

Rest, A., Stubbs, C., Becker, A. C., et al. 2005b, The Astrophysical Journal, 634, 1103, doi: `10.1086/497060`

Rest, A., Welch, D. L., Suntzeff, N. B., et al. 2008a, The Astrophysical Journal, 681, L81, doi: `10.1086/590427`

Rest, A., Matheson, T., Blondin, S., et al. 2008b, The Astrophysical Journal, 680, 1137, doi: `10.1086/587158`

Rest, A., Prieto, J. L., Walborn, N. R., et al. 2012, Nature, 482, 375, doi: `10.1038/nature10775`

Rest, A., Scolnic, D., Foley, R. J., et al. 2013, doi: `10.1088/0004-637X/795/1/44`

Riess, A. G., Filippenko, A. V., Challis, P., et al. 1998, The Astronomical Journal, 116, 1009, doi: `10.1086/300499`

Riess, A. G., Yuan, W., Macri, L. M., et al. 2022, The Astrophysical Journal Letters, 934, L7, doi: `10.3847/2041-8213/ac5c5b`

Robin, A. C., Reylé, C., Marshall, D. J., & Schultheis, M. 2012, 26, 171, doi: `10.1007/978-3-642-18418-5_18`

Robitaille, T., & Bressert, E. 2012, Astrophysics Source Code Library, ascl:1208.017. `https://ui.adsabs.harvard.edu/abs/2012ascl.soft08017R`

Rosswog, S., Kasen, D., Guillochon, J., & Ramirez-Ruiz, E. 2009, The Astrophysical Journal, 705, L128, doi: `10.1088/0004-637X/705/2/L128`

Roy, N., Tiwari, V., Bobrick, A., et al. 2022, 3D Hydrodynamical Simulations of Helium-Ignited Double-degenerate White Dwarf Mergers, Tech. rep. `https://ui.adsabs.harvard.edu/abs/2022arXiv220409683R`

Ruiz-Lapuente, P. 2019, New Astronomy Reviews, 85, 101523, doi: `10.1016/j.newar.2019.101523`

Ruiz-Lapuente, P., Damiani, F., Bedin, L., et al. 2018, The Astrophysical Journal, 862, 124, doi: `10.3847/1538-4357/aac9c4`

Ruiz-Lapuente, P., Comeron, F., Méndez, J., et al. 2004, Nature, 431, 1069, doi: `10.1038/nature03006`

Ruiz-Lapuente, P., González Hernández, J. I., Mor, R., et al. 2019, The Astrophysical Journal, 870, 135, doi: `10.3847/1538-4357/aaf1c1`

Ryabchikova, T., Piskunov, N., Kurucz, R. L., et al. 2015, Physica Scripta, 90, 054005, doi: `10.1088/0031-8949/90/5/054005`

Ryabchikova, T. A., Piskunov, N. E., Kupka, F., & Weiss, W. W. 1997, Baltic Astronomy, 6, 244, doi: `10.1515/astro-1997-0216`

Rybicki, G. B., & Lightman, A. P. 1986, Radiative Processes in Astrophysics. `https://ui.adsabs.harvard.edu/abs/1986rpa..book.....R`

Saio, H., & Nomoto, K. 1985, Astronomy and Astrophysics, 150, L21. `https://ui.adsabs.harvard.edu/abs/1985A&A...150L..21S`

Sand, D. J., Hsiao, E. Y., Banerjee, D. P. K., et al. 2016, The Astrophysical Journal, 822, L16, doi: `10.3847/2041-8205/822/1/L16`

Sand, D. J., Graham, M. L., Botyánszki, J., et al. 2018, The Astrophysical Journal, 863, 24, doi: `10.3847/1538-4357/aacde8`

Sato, Y., Nakasato, N., Tanikawa, A., et al. 2015, The Astrophysical Journal, 807, 105, doi: `10.1088/0004-637X/807/1/105`

Sbordone, L., Bonifacio, P., Castelli, F., & Kurucz, R. L. 2004, Memorie della Societa Astronomica Italiana Supplementi, 5, 93, doi: `10.48550/arXiv.astro-ph/0406268`

Schaefer, B. E., & Pagnotta, A. 2012, Nature, 481, 164, doi: `10.1038/nature10692`

Schechter, P. L., Mateo, M., & Saha, A. 1993, Publications of the Astronomical Society of the Pacific, 105, 1342, doi: `10.1086/133316`

Schlafly, E. F., & Finkbeiner, D. P. 2011, The Astrophysical Journal, 737, 103, doi: `10.1088/0004-637X/737/2/103`

Schmidt, B. P., Suntzeff, N. B., Phillips, M. M., et al. 1998, The Astrophysical Journal, 507, 46, doi: `10.1086/306308`

Schwab, J. 2021, The Astrophysical Journal, 906, 53, doi: `10.3847/1538-4357/abc87e`

Schwab, J., Quataert, E., & Kasen, D. 2016, Monthly Notices of the Royal Astronomical Society, 463, 3461, doi: `10.1093/mnras/stw2249`

Shappee, B. J., Kochanek, C. S., & Stanek, K. Z. 2013a, \apj, 765, 150, doi: `10.1088/0004-637X/765/2/150`

Shappee, B. J., Piro, A. L., Stanek, K. Z., et al. 2018, The Astrophysical Journal, 855, 6, doi: `10.3847/1538-4357/aaa1e9`

Shappee, B. J., Stanek, K. Z., Pogge, R. W., & Garnavich, P. M. 2013b, The Astrophysical Journal, 762, L5, doi: `10.1088/2041-8205/762/1/L5`

Shappee, B. J., Piro, A. L., Holoien, T. W. S., et al. 2016, The Astrophysical Journal, 826, 144, doi: `10.3847/0004-637X/826/2/144`

Shen, K. J., & Bildsten, L. 2014, The Astrophysical Journal, 785, 61, doi: `10.1088/0004-637X/785/1/61`

Shen, K. J., & Schwab, J. 2017, The Astrophysical Journal, 834, 180, doi: `10.3847/1538-4357/834/2/180`

Shen, K. J., Boubert, D., Gänsicke, B. T., et al. 2018, \apj, 865, 15, doi: `10.3847/1538-4357/aad55b`

Shields, J. V., Arunachalam, P., Kerzendorf, W., et al. 2023, The Astrophysical Journal, 950, L10, doi: `10.3847/2041-8213/acd6a0`

Shields, J. V., Kerzendorf, W., Hosek, M. W., et al. 2022, The Astrophysical Journal Letters, 933, L31, doi: `10.3847/2041-8213/ac7950`

Sneden, C. 1973, The Astrophysical Journal, 184, 839, doi: `10.1086/152374`

Sneden, C., Bean, J., Ivans, I., Lucatello, S., & Sobeck, J. 2012, Astrophysics Source Code Library, ascl:1202.009. `https://ui.adsabs.harvard.edu/abs/2012ascl.soft02009S`

Stancil, P. C. 1994, The Astrophysical Journal, 430, 360, doi: `10.1086/174411`

Stehlé, C., & Hutcheon, R. 1999, Astronomy and Astrophysics Supplement Series, 140, 93, doi: `10.1051/aas:1999118`

Sutton, K. 1978, Journal of Quantitative Spectroscopy and Radiative Transfer, 20, 333, doi: `10.1016/0022-4073(78)90102-4`

Timmes, F. X., Woosley, S. E., & Weaver, T. A. 1995, The Astrophysical Journal Supplement Series, 98, 617, doi: `10.1086/192172`

Traving, G. 1960, Zeitschrift fur Astrophysik, 49, 231. `https://ui.adsabs.harvard.edu/abs/1960ZA.....49..231T`

Tucker, M. A., & Shappee, B. J. 2024, The Astrophysical Journal, 962, 74, doi: `10.3847/1538-4357/ad1b4e`

Tucker, M. A., Shappee, B. J., Vallely, P. J., et al. 2020, Monthly Notices of the Royal Astronomical Society, 493, 1044, doi: `10.1093/mnras/stz3390`

Valdes, F., Gruendl, R., & DES Project. 2014, 485, 379. `https://ui.adsabs.harvard.edu/abs/2014ASPC..485..379V`

Valenti, J. A., & Piskunov, N. 1996, Astronomy and Astrophysics Supplement Series, 118, 595. `https://ui.adsabs.harvard.edu/abs/1996A&AS..118..595V`

Vallely, P. J., Fausnaugh, M., Jha, S. W., et al. 2019, Monthly Notices of the Royal Astronomical Society, 487, 2372, doi: `10.1093/mnras/stz1445`

van der Marel, R. P., Alves, D. R., Hardy, E., & Suntzeff, N. B. 2002, The Astronomical Journal, 124, 2639, doi: `10.1086/343775`

van Noort, M., Hubeny, I., & Lanz, T. 2002, The Astrophysical Journal, 568, 1066, doi: `10.1086/338949`

Virtanen, P., Gommers, R., Oliphant, T. E., et al. 2020, Nature Methods, 17, 261, doi: `10.1038/s41592-019-0686-2`

Wang, B., & Han, Z. 2012, New Astronomy Reviews, 56, 122, doi: `10.1016/j.newar.2012.04.001`

Wang, B., Meng, X., Chen, X., & Han, Z. 2009, Monthly Notices of the Royal Astronomical Society, 395, 847, doi: `10.1111/j.1365-2966.2009.14545.x`

Warner, B. 1967, Monthly Notices of the Royal Astronomical Society, 136, 381, doi: `10.1093/mnras/136.4.381`

Webbink, R. F. 1984, The Astrophysical Journal, 277, 355, doi: `10.1086/161701`

Werner, M. W., Roellig, T. L., Low, F. J., et al. 2004, The Astrophysical Journal Supplement Series, 154, 1, doi: `10.1086/422992`

Wheeler, A. J., Abruzzo, M. W., Casey, A. R., & Ness, M. K. 2023, The Astronomical Journal, 165, 68, doi: `10.3847/1538-3881/acaaad`

Whelan, J., & Iben, Jr., I. 1973, The Astrophysical Journal, 186, 1007, doi: `10.1086/152565`

White, S. D. M., & Frenk, C. S. 1991, The Astrophysical Journal, 379, 52, doi: `10.1086/170483`

White, S. D. M., & Rees, M. J. 1978, Monthly Notices of the Royal Astronomical Society, 183, 341, doi: `10.1093/mnras/183.3.341`

Whitmore, B. C., Allam, S. S., Budavári, T., et al. 2016, The Astronomical Journal, 151, 134, doi: `10.3847/0004-6256/151/6/134`

Williams, B. J., Borkowski, K. J., Ghavamian, P., et al. 2013, The Astrophysical Journal, 770, 129, doi: `10.1088/0004-637X/770/2/129`

Willmer, C. N. A. 2018, The Astrophysical Journal Supplement Series, 236, 47, doi: `10.3847/1538-4365/aabfdf`

Winkler, P. F., Gupta, G., & Long, K. S. 2002, doi: `10.1086/345985`

Winkler, P. F., Long, K. S., Hamilton, A. J. S., & Fesen, R. A. 2005, The Astrophysical Journal, 624, 189, doi: `10.1086/429155`

Wishart, A. W. 1979, Journal of Physics B: Atomic and Molecular Physics, 12, 3511, doi: `10.1088/0022-3700/12/21/009`

Wojtak, R., Hjorth, J., & Osman Hjortlund, J. 2023, Two-population Bayesian hierarchical model

of type Ia supernovae, Tech. rep., doi: `10.48550/arXiv.2302.01906`

Woods, T. E., Ghavamian, P., Badenes, C., & Gilfanov, M. 2017, Nature Astronomy, 1, 800, doi: `10.1038/s41550-017-0263-5`

Zheng, W., Silverman, J. M., Filippenko, A. V., et al. 2013, The Astrophysical Journal, 778, L15, doi: `10.1088/2041-8205/778/1/L15`